Vibrational Kerr Spectroscopy

by

James A. Janni

B.S. with Distinction, Iowa State University, 1993

Submitted to the Department of Chemistry in Partial Fulfillment of the Requirements for
the degree of

DOCTOR OF PHILOSOPHY

at the

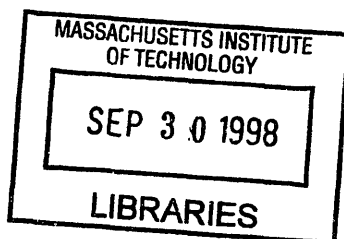Massachusetts Institute of Technology

June 1998

Signature of Author_____

Department of Chemistry
June 9, 1998

Certified by_____

Jeffrey I. Steinfeld
Professor of Chemistry, Thesis Supervisor

Certified by_____

Robert W. Field
Professor of Chemistry, Thesis Supervisor

Accepted by_____

Dietmar Seyferth
Chairman, Department Committee on Graduate Students

This doctoral thesis has been examined by a Committee of the Department of Chemistry as follows:

Professor Moungi G. Bawendi _____

                                                                       Chairman

Professor Jeffrey I. Steinfeld _____

                                                        Thesis Supervisor

Professor Robert W. Field _____

                                                        Thesis Supervisor

Professor Bruce Tidor _____

To My Wife

Vibrational Kerr Spectroscopy

by

James A. Janni

Submitted to the Department of Chemistry on June 9, 1998
in partial fulfillment of the requirements for the degree of
Doctor of Philosophy in Chemistry

Abstract

The infrared vibrational Kerr effect was investigated as a potentially selective and sensitive detection method for explosives. The investigation of the vibrational Kerr effect commenced with the first reported measurement of the integrated infrared vapor absorption strengths for the explosives trinitrotoluene (TNT), cyclotrimethylene trinitramine (RDX), and pentaerythritrol tetranitrate (PETN). From the infrared absorption spectra, the characteristic NO_2 symmetric and asymmetric stretch bands of the explosives were identified as spectral targets for the vibrational Kerr effect.

The vibrational Kerr spectra of fluoroform and nitromethane were successfully measured with conventional Kerr techniques. The vibrational Kerr measurements were first made on the CH stretch-bend combinations of fluoroform around 7000 cm^{-1}. The remainder of the vibrational Kerr measurements were carried out on the NO_2 asymmetric stretch band of nitromethane at 1584 cm^{-1}. Nitromethane was an ideal test molecule of the infrared measurement system because of its similarity to the explosives and its large room temperature vapor pressure. Rotationally resolved Kerr spectra of nitromethane were recorded for segments of the asymmetric stretch band and the expected qualitative features of the Kerr spectra were observed. Although the sensitivity needed for the detection of explosives was not demonstrated, the selective detection of polar molecules over weakly polar molecules was demonstrated for a mixture of nitromethane and nitrogen dioxide. The methods investigated for measurement of the Kerr effect in both the infrared and ultraviolet spectral regions are described in detail. Polarization modulation of the light source with phase sensitive detection was expected to increase sensitivity to the Kerr effect over conventional Kerr techniques. Despite the anticipated sensitivity enhancement offered by polarization modulation, poor performance of the photoelastic modulators and the Fourier Transform spectrometer impeded the demonstration of the enhancement.

Thesis Supervisor: Jeffrey I. Steinfeld   Thesis Supervisor: Robert W. Field
Title: Professor   Title: Professor

.

Acknowledgments

My education prior to MIT is filled with extraordinary educators. My interest in chemistry began thanks to the teaching and dedication of Dr. Donald Savage. His effort challenged me to explore all of my questions through research, study, and experiment. Only a short time after leaving the classes of Dr. Savage, I was fortunate to have Dr. Martha Russel as an advisor. She tirelessly monitored my progress with encouragement throughout my undergraduate education. During this education, I had the splendid opportunity to work in the laboratories of Dr. James Espenson. Dr. Espenson provided me with an experience in research that will always be appreciated. My gratitude extends to Dr. Andreja Bakac who honed my experimental skills in Dr. Espenson's laboratory. I am grateful for the financial support provided by the Barry Goldwater Excellence in Education Foundation.

All of this however would not have been possible without the support I first received from my family. My parents' dedication to my success and happiness provided me with the confidence, determination, and discipline to achieve my goals. Their devotion has been complete.

I dedicate this dissertation to my wife, because of the sacrifices that she made to make my graduate education possible. The times are too numerous to describe when she has extended herself beyond my expectations without complaint. Her support has been unwavering. God has blessed me with a supportive family, and a world full of grace, beauty, and love.

Table of Contents

Chapter One

Kerr Spectroscopy and Aviation Security

1.1 Introduction

Explosives exemplify the potential of chemistry in harnessing chemical processes for useful ends. However, when improperly handled, stored, or used, they pose a threat to human health and safety. The dangers, ranging from deliberate terrorist attacks to inadvertent groundwater contamination by explosive residues, make the detection of these molecules an important scientific effort. Research in the explosives detection field continues to address the problems of sensitivity and selectivity for the explosives. Within this field of scientific inquiry, the potential of gas phase vibrational Kerr spectroscopy as a sensitive and selective detection method for use in aviation security applications and as a more general spectroscopic technique will be examined.

The first three chapters build a foundation for understanding vibrational Kerr spectroscopy as a potential security tool. Giving an overview of the requirements for an aviation security system, the first chapter includes an overview of detection methods proposed for aviation security, a qualitative comparison of these methods with spectroscopic methods such as Kerr, and an exploration of the work already done on Kerr spectroscopy. The next chapter reports on the infrared vibrational vapor spectra recorded as a precursor to Kerr spectroscopy for the explosive molecules trinitrotoluene (TNT), pentaerythritol tetranitrate (PETN), and cyclotrimethylene trinitramine (RDX), shown in

Fig. 1.1. In Chapter Three a primitive model for the Kerr effect is constructed based on classical and time dependent perturbation treatments of absorption and dispersion in linear dichroism and birefringence. Using the results of the two simplified derivations of the Kerr effect, a Jones Matrix based calculation of the signals from the classic Kerr measurement apparatus is performed.
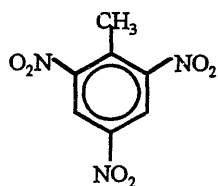
Trinitrotoluene
(TNT)
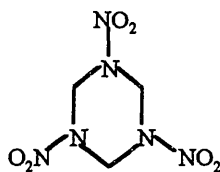
Cyclotrimethylene Trinitramine
(RDX)

Pentaerythritrol Tetranitrate
(PETN)

Figure 1.1 The Federal Aviation Administration has targeted these molecules in its efforts to improve airport security. The explosives RDX and PETN are of particular concern because they are the primary explosives in the plastic explosive SEMTEX; a major terrorist weapon.

The Kerr effect can certainly be understood with the results of the first three chapters, but the simple ideas of these chapters must be extended to describe the effect quantitatively. In Chapter Four, the primitive model of the Kerr effect is extended with an analysis of the polarizability that arises from the classical orientation of polar molecules in an applied static field. With the classical orientation model, a semi-classical derivation of the Kerr effect is also given for rovibrational and rovibronic transitions. The results of a Kerr spectrum simulation for the 1584 cm^{-1} asymmetric stretch band of nitromethane

based on the rovibrational model constructed for optical anistropy in Chapter Four is presented in Chapter Five.

The chapters describing the theory of the Kerr effect are followed by chapters describing the measurement of the Kerr effect for nitromethane. In Chapter Six all of the detection methods that were explored are described and compared with techniques used in previous measurements of infrared optical activity. The final Kerr apparatus described in Chapter Seven was used to record the results for nitromethane reported in the same chapter. Included in Chapter Seven is a comparison between the expected and the experimental results.

Exploring the challenges of using Kerr spectroscopy as a sensitive and selective technique for the detection of the explosive molecule vapors, the final chapter makes suggestions for improving sensitivity to the effect through modifications to the Kerr apparatus used for nitromethane. The final chapter also explores the possibility of using the Kerr effect as a more general spectroscopic tool.

1.2 Aviation Security

Vibrational Kerr spectroscopy of the explosives was pursued as a tool for explosives vapor detection under the direction of the Federal Aviation Administration (FAA Announcement 12015) . For this reason, the requirements set forth by the FAA for certification of a detection method served as the benchmark for proposing and evaluating spectroscopic techniques. The FAA's criteria stipulated that a system must be able to

sense less than 50 pg of the explosives TNT, PETN, and RDX, in less than 5 seconds with no false negatives and less than 5 % false positives. The systems also had to fit conveniently into the existing airport security infrastructure such as baggage and passenger screening, and not require specially trained security personnel. Air travel and transport would be crippled by a failure to meet the FAA's requirements, as screening of passengers and cargo would become too time consuming and costly.

A number of techniques for aviation security have been proposed for detecting explosives and explosive devices.[1,2] The techniques addressing the aviation security issue have been divided into bulk detection, with the goal of finding bombs and weapons, and residue or trace detection, used as an indicator of concealed devices on suspicious passengers and cargo. Proposals for the bulk detection of explosive have been based on neutron scattering, nuclear quadrupole resonance, and advanced x-ray imaging. For trace detection, gas chromatography, mass spectrometry, and ion mobility spectrometry have been proposed for detecting explosive residues around passengers and packages. The trace detection technologies coupled with specially designed concentrators, and passenger and cargo portals, which increase the sampled space and decrease interferences, have also been suggested as explosive vapor detectors. Both the bulk and trace detection methods mentioned above rely on systems that have large power requirements, have some level of mechanization, are expensive, and require specially trained operators. Therefore, research continues with the goal of development of detection schemes which are simpler, inexpensive, compact, and robust.

Optical spectroscopy offers a number of possible advantages to the systems considered above. First, with the development of small, powerful laser systems and detectors based on micro-electronic fabrication, explosives can be detected using lightweight, compact, and non-mechanical instrumentation. Photonics technology similar to the systems envisioned here have already been utilized in such varied instruments as compact Raman spectrometers and grocery store scanners. Similar systems for explosives detection are likely to be much less costly than some of the more sophisticated equipment required for techniques such as advanced x-ray imaging. Instrumentation can also be imagined similar to the laser scanners, which require little operator training and minimal maintenance.

The key to the development of spectroscopic detection methods lies in defining spectroscopic signatures. Molecular discrimination is often based on the vibrational fingerprint region in the mid-IR. Likewise, the Raman spectra of explosives produce typical explosives' signatures. The difficulty in deploying these techniques begins with their low sensitivity relative to the expected quantities of the explosives. Table 1.1 gives an indication of the sensitivity required for an infrared absorption based vapor detector probing the strongest infrared features of the target explosives. Considerable effort has been expended here and elsewhere to modify the insensitive conventional techniques through such enhancements as surface-enhanced Raman and cavity ringdown for the infrared. Often, increasing sensitivity decreases selectivity. In the case of infrared cavity ringdown, in particular, the asymmetric or symmetric stretches of the $-NO_2$ group of nitro explosives, the characteristic bands of the explosives, overlap bands of water and NO_2;

thus, any enhancement to the absorbance sensitivity for the explosives will inevitably result in greater sensitivity to these interfering compounds.

Table 1.1 Concentrations of the explosives at 300 K based on vapor pressure saturation.[3]

Property at 300 K	RDX	PETN	TNT
Concentration [mol/cm^3]	3×10^{-16}	8×10^{-16}	4×10^{-13}
Concentration [g/cm^3]	8×10^{-14}	3×10^{-13}	9×10^{-11}
Infrared Absorbance for Strongest Infrared Feature[a] [1/cm]	3×10^{-10}	1×10^{-10}	3×10^{-7}

[a] based on results to be discussed in Chapter Two

Finding explosive molecules in complex non-laboratory environments, then, seems dependent on developing simultaneous sensitivity to many of the physical properties of the explosives, rather than relying on one property such as the infrared absorption spectra, at a time. In work with Varian, a method for removing the ubiquitous atmospheric gases while delivering a sample of the explosive concentrated by two orders of magnitude through the use of a membrane separator with coldtrap pre-concentrator is being investigated. The complete system exploits the different affinities of the atmospherics and explosives to a treated silicon substrate, differences in diffusion rates, differences in vapor pressure and differences in the specific infrared absorption frequencies associated with the NO_2 groups on the explosives, for discrimination of the explosive compounds.

The Kerr technique continues the multifaceted interrogation of explosive samples. The first property probed in the vibrational Kerr effect detection of explosives is the characteristic NO_2 symmetric and asymmetric vibrational stretches observed in the mid-IR. With the IR signature as a base, the second identifying feature is the large dipole moments that nitro explosives often exhibit. Table 1.2 gives the average dipole moment reported for several nitro compounds and a few atmospheric gases. As will be shown in Chapter Four, the Kerr effect for molecules in the gas phase is strongly connected to the size of a molecule's dipole moment. The resulting sensitivity and selectivity was the focus of the development of vibrational Kerr spectroscopy.

Table 1.2 Average dipole moments of the explosive, simulants, water and nitrogen dioxide based on values in ref. 4.

Molecule	Dipole Moment [D]
Nitrobenzene	4.2
Nitromethane	3.4
o-Nitrotoluene	3.6
p-Nitrotoluene	4.4
Trinitrotoluene	1.2
PETN	2.5
RDX	5.8
Water	1.8
Nitrogen Dioxide	0.3

1.3 Previous Work

The Kerr effect was proposed by the Rev. John Kerr in 1875.[5] During Rev. Kerr's summer vacations of 1879 and 1880, he was able to experimentally verify his theory for more than one hundred substances. The Kerr effect is the optical anisotropy produced in a medium as the result of application of an electric field. The effect is most often quantified by measurement of the change in polarization of light that occurs as it traverses an anisotropic medium. In the classic Kerr measurement apparatus, shown in Fig. 1.2, the polarized light is first generated with a polarizer oriented with its polarization axis at 45 ° with respect to the applied field. The resulting polarization has equal linear components parallel and perpendicular to the applied field. The variation in propagation characteristics along the axis parallel and perpendicular to the field changes the polarization of the light so that the resultant light is elliptically polarized with its major axis tilted away from the original polarization axis. The propagation properties along the two axes differ in the amount of absorption or dispersion that occurs for light polarized in directions along the orthogonal axes. The resulting polarization now has some component parallel to the polarization axis of the second analyzer polarizer as shown in Fig. 1.2. The intensity of the transmitted light is the observable quantity in the Kerr effect.
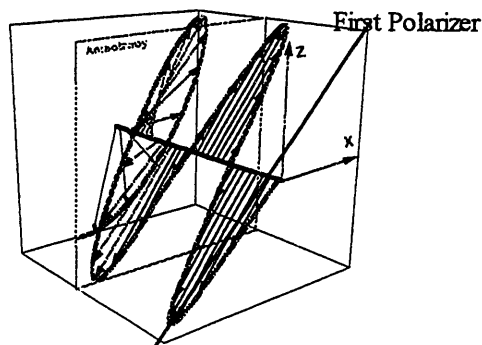
A.
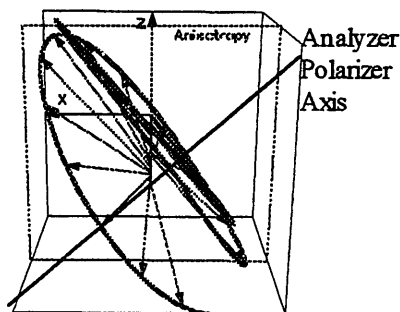
B

Figure 1.2 The classic Kerr apparatus measures the changes that occur in light linearly polarized at 45° with respect to the applied field. In this figure the field is along the Z axis. As frame B indicates, the change in the polarization of light results in a polarization component parallel to the analyzer polarizer's polarization axis.

Since the summers of 1879 and 1880 Kerr measurements have continued extensively in the visible portion of the spectrum. These measurements have led to the development of such practical devices as optical switches and to the documenting of non-linear optical properties of molecules for use in non-linear optics-based systems useful in such diverse fields as communications and medicine. Investigators of this phenomenon have achieved shot-noise limited dispersion angle sensitivity of 10^{-9} radians in the visible and it was hoped that this sensitivity could be extended to the infrared.[6] The Kerr sensitivity to explosives would be at least an order of magnitude better than conventional

infrared spectroscopy, and potentially more selective than conventional infrared spectroscopy.

Much of the theoretical description of the Kerr effect for gas phase molecules has been derived and reported by A.D. Buckingham. In a series of papers Buckingham describes, classically, the dependence of the Kerr effect on the orientational energy and later, quantum mechanically on the rotational state of the molecules.[7,8] His work also describes the typical magnitudes of the effect for electronic, vibrational, and rotational transitions. He only considers the real part of the polarizablilty and thus linear birefringence. The connection can easily be made between this birefringence and the corresponding dichroism through the Kramers-Kronig relationship. In a later collaboration with Brown and Ramsay, Buckingham considers both the real and imaginary terms in the description of the Kerr effect for formaldehyde.[9] The papers by Buckingham and by Brown, Buckingham and Ramsay provide an important theoretical model for predicting the size and nature of the effect reported for gas phase vibrational Kerr spectroscopy.

Despite the extensive work done on the Kerr effect in the visible, in spectral regions near the wavelengths of strong electronic or vibrational bands across the spectrum few measurements have been made. Through the use of photographic plates and the classic Kerr apparatus, Klemperer and Freeman observed the Kerr effect for the $\tilde{A}^1 A_2 - \tilde{X}^1 A_1 (\pi^* \leftarrow n)$ ultraviolet transition of formaldehyde in 1964.[10] The effect was again reported for this molecule in 1969 by Bridge, Haner, and Dows.[11] Their work focused on the differential line shapes in the presence and absence of an electric field, and

only briefly mentioned the possibility of using the Kerr effect as a spectroscopic technique. Brown, Buckingham and Ramsay repeated the formaldehyde measurement using photographic plates and analyzed their data based on their theoretical model already mentioned.[10] The measurements done on formaldehyde were preceded by the measurements of the infrared Kerr effect for liquid nitrobenzene in its vibrational overtone region (1.5-5.6 μm).[12] Recently, Slenczka made measurements similar to the Kerr effect on ICl ($A^3\Pi_1(v' = 19) - X^1\Sigma(v'' = 0)$) at 600 nm and provided a qualitative description of his results which relied solely on linear dichroism to explain the results.[13] The work reported here represents the first measurement of the Kerr effect in the infrared near a vibrational band of molecules in the gas phase.

1.4 Summary

As already stated, the spectroscopic technique of vibrational Kerr spectroscopy will be discussed in this thesis in the context of improved explosives detection. The thesis will suggest ways of making Kerr spectroscopy a viable and competitive detection option based on observations of the Kerr effect of nitromethane. Further suggestions will be made based on a review of the theory of the Kerr effect and research on infrared optical activity.

References

[1] J.I. Steinfeld, J. Wormhoudt, *Ann. Rev. Phys. Chem.* in press (1998).

[2] P. Kolla, *Angew. Chem.* 36 (1997) 800.

[3] B.C. Dionne, D.P. Rounbehler, E.K.Achter, J. R. Hobbs, and D. H. Fine, *J. Energetic Mater.* 4 (1986) 447.

[4] A. L. McCellan, ed. *Tables of Experimental Dipole Moments* W. H. Freeman San Fransico, (1968).

[5] John Kerr, *Phil. Mag.* 50 (1875) 446.

[6] D. P. Shelton, R. E. Cameron, *Rev. Sci. Instrum.* 49 (1988) 430.

[7] A.D. Buckingham, A. D. Pople *Proc. Roy. Soc.* A68 (1955) 905.

[8] A. D. Buckingham, *Proc. Phys. Soc.* A267 (1962) 271.

[9] J. M. Brown, A. D. Buckingham, D. A. Ramsay, *Can. J. Phys.* 49 (1971) 914.

[10] D. E. Freeman, W. Klemperer, *J. Chem. Phys.* 40 (1964) 604.

[11] N. J. Bridge, D. A. Haner, D. A. Dows, *J. Chem. Phys.* 48 (1958) 4196.

[12] E. Charnery, R. S. Halford, *J. Chem. Phys.* 46 (1958) 221.

[13] A. Slenczka, *Phys. Rev. Lett.* 80 (1998) 2566.

Chapter Two

Infrared Absorption Features of the Explosives

2.1 Introduction

Before experiments on the vibrational Kerr effect on the gas phase explosives TNT, RDX, and PETN could commence, measurements of the infrared absorption spectra of these molecules had to be made to determine the frequencies of the NO_2 stretches as well as their absorption cross sections. Although many infrared and Raman measurements had previously been made on the solid explosives, TNT and RDX were the only explosives considered for which infrared gas phase spectra had been published.[1-7] However, the absorption strengths were not reported. Such measurements were quite challenging given the low vapor pressures of the explosives, and their tendency to adsorb to surfaces and to decompose. This chapter describes the experimental setup and procedures used to measure the infrared absorption cross sections for the explosives. Included with the description of the experimental apparatus is a description of an *ab initio* calculation done for TNT as a means of identifying the modes and frequencies in the infrared and Raman spectra. An attempt was also made to measure the infrared gas phase spectra of ammonium nitrate, but NH_4NO_3 decomposed to ammonia, water, and nitric acid on heating.

2.2 Experimental Setup

Samples of the explosives were obtained from Mason and Hanger Pantex plant following authorization by Sandia National Laboratories. The materials were used as received without purification.

Figure 2.1 shows the vapor cell used for the measurement of the infrared vapor spectra of explosives. The vapor cell for the explosives was constructed with Varian Conflat flanges with a cell pathlength of 123 cm. At each end, one inch diameter, 0.5 cm thick MgF_2 windows were attached to the cell via a compressed Viton O-ring. The windows were compressed against the O-ring by copper sleeves attached to one inch Conflat window mounts as illustrated in Figure 2.1. The windows, along with the copper sleeve, were wrapped in heating tape to ensure that the windows were always at a temperature higher than the sample to prevent condensation of the explosives on the windows. Samples were introduced into the cell through a Swagelok plug attached to one of the flanges.

The quantity of explosive delivered to the cell was controlled via the equilibrium vapor pressure at a given temperature of the sample. For this reason, the temperature of the cell was monitored and controlled by five Chromel/alumel thermocouples attached to Omega CN76000 temperature controllers. These controllers were capable of controlling temperature to ± 0.1°. However, because of the thermal properties of the cell, the temperature was only maintained to ± 1°. An additional Omega CN76000 controller was used to select and maintain the temperature of the sample arm. The temperatures at

various points on the cell were also checked occasionally during a run with Chromel/alumel thermocouples connected to a Watlow 873 temperature readout. These measurements were necessary for locating possible cold spots and are the basis for the temperature uncertainty reported above. The temperature controllers were connected to a heating system consisting of nichrome heating tape (Omega FGS, 8 W/in^2) wrapped around the cell with fiber glass thermal insulation.
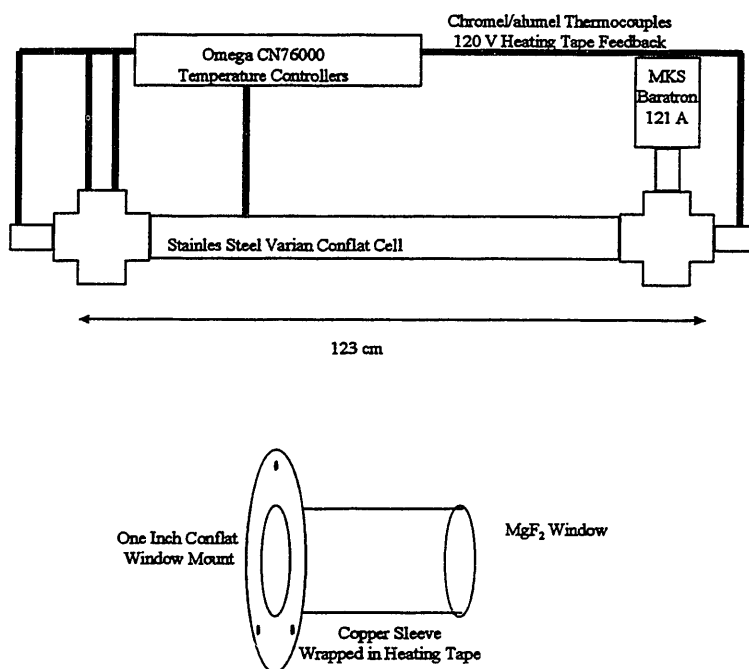
Figure 2.1 The absorption cell body was constructed of Varian Conflat flanges. The window mounts were modified to facilitate more even heating of the windows, particularly to minimize cold spots at the center of the windows.

When pressure measurements were possible, the pressure was monitored with a MKS Baratron model 21A bakeable pressure transducer. At room temperature this device

worked well as an absolute pressure device for measurement of pressures between 0.001 and 1 Torr. However, at elevated temperatures the zero of the Baratron indicated negative pressures. Therefore, the Baratron was used exclusively in differential mode once it had reached temperature equilibrium at temperatures greater than 300 K.

Spectra were collected with a BioRad FTS60A Fourier Transform Spectrometer using the internal ceramic source as the Mid-IR source. The external beam port was used to send the light from the interferometer to the infrared absorption cell. The light was directed into the cell with two gold mirrors for horizontal and vertical control. The internal aperture was removed to increase the light levels by a factor of two outside of the spectrometer bench. The detector was a liquid-nitrogen-cooled HgCdTe detector built by Santa Barbara Research Associates (A120 436) with pre-amplifier. The optimum scan rates were either 2.5 kHz or 5 kHz, where this frequency corresponds to the rate of HeNe reference laser zero crossings. The former was preferred as it allowed real-time display of the collected spectra. This scanning frequency corresponded to a mirror speed of 0.156 cm s^{-1}. The spectra were collected with a undersampling ratio (UDR)[a] of 0.25 or 1 depending on the mirror speed selected with the former selected for the faster speeds. All spectra were recorded at 16 cm^{-1} resolution with triangular apodization, gain range ratio (GRR)[a] of 40 and with a zero filling factor (ZFF)[a] of two. The output of the preamplifier was further amplified to fill the Bio-Rad A/D converter by a Princeton Applied Research 113 amplifier ($\pm$ 10 V).

---

[a] BioRad FTS60A terms are defined in Appendix A.

During the scanning of the infrared absorption spectra of the explosives, water and carbon dioxide lines were minimized in the spectra by purging the spectrometer and light path outside of the spectrometer with dry nitrogen boiling off a high pressure liquid nitrogen Dewar. The light path purge outside of the cell was constructed of 4 inch diameter plastic dryer tubing which created a convenient, compact purge volume.

2.3 Experimental Procedures

In this section the sequence of steps taken to record the infrared absorption spectra is described. The first task was to insure that there were no contaminants in the stainless steel cell that might interfere with the collection of the explosives' spectra. To remove the contaminants from the cell, it was heated to above 473 K for over eight hours while connected to the vacuum mechanical pump via a glass vacuum manifold with a liquid nitrogen cold trap. The heating of the cell was continued until a background pressure below 5×10^{-4} Torr was achieved. Once the cell had been cleaned in this manner, the cell temperature was reduced to 300 K.

The next step in this process was introduction of the explosives into the cell. Solid samples (30-50 mg) of the explosives were placed in the Swagelok plug which was then attached to the sample arm. While pumping on this sample, the temperature of the sample was slowly raised to 353 K. Pumping on the sample cell continued until the pressure stabilized at the level achieved after cleaning. Heating and pumping were used to remove the volatile gases from the explosive sample.

During the preparation of the sample, the bench and light path were purged using dry nitrogen for at least an hour. Scans were recorded of the empty cell and beam path as the water and carbon dioxide were removed from the path. Once the absorption lines for water and carbon dioxide had reached the same level as the noise background power spectra, spectral scans could be begun for the explosives. The first scan recorded was the background power spectrum used to calculate the absorption spectra.

After the background spectra had been recorded, the temperature of the sample arm was slowly raised to the desired starting temperature while the remainder of the cell including the windows was heated to at least 20 K higher to insure that the equilibrium pressure was determined by the sample temperature. The sample temperature was then raised in 10 K increments until the sample had completely decomposed. Spectra were collected at each of the set temperatures after the cell and sample arm had stabilized. Collection of 1024 scans for each spectrum took approximately 10 minutes. Changes in the cell and sample temperature of 5 to 10 degree increments also took 10-15 minutes. One temperature series with this timing took 2-3 hours. The total recording time of a temperature series determined the contribution of the decomposition products to the spectra.

The absorption spectra collected were processed with the BioRad software and were then translated to JCAMP[a] format. Before the JCAMP ascii files could be used with any of the available graphical presentation software, they had to be transformed from the JCAMP format to a format compatible with the graphical presentation software. This translation was performed with a Microsoft Excel Macro developed here.[8] The

conversion from the BioRad proprietary platform to a PC platform is only possible for transmission and absorbance data. Interferograms and power spectra cannot be translated in the same manner because a lack of suitable translation programs.

The translated absorption spectra were processed and analyzed using Microcal Origin.[9] Using this software, the integrated absorption intensities were determined by a Simpson's rule integration performed by the Microcal software. The baseline corrections were applied as needed, after the integration limits had been determined visually. The estimated uncertainty in these intensities is based on the propagation of errors associated with measuring the temperature, pressure, and absorbance. The major source of error is in the temperature measurements, which determines the pressures recorded for each run.

2.4 Calculation of the TNT Vibrational Spectra

The infrared spectra of TNT have been recorded in the solid, solution and vapor phases and calculated using semi-empirical methods. In this study, ab initio calculations were carried out for comparison with the experimental infrared and Raman spectra. Similar *ab initio* calculations had already been carried out to determine the structure of the molecules.

Vibrational and Raman frequencies were calculated using the Gaussian 94 HF/6-31G basis set.[10] The initial input geometry was generated using the program 'Quanta' on a Silicon Graphics Indigo-2 workstation.[11] MNDO and HF/STO-3G calculations were performed to refine these input parameters. In an attempt to decrease computational time,

the dihedral angles of the 2,6-nitro groups with the ring were constrained to be equal to each other in the initial geometry calculations, while the 4-nitro group was constrained so that its plane remained in the plane of the aromatic ring. The Gaussian 94 HF/6-31G basis set was used to calculate the infrared and Raman frequencies and intensities reported here. These calculations took 3-4 days on a Hewlett Packard 9000/735 workstation.

2.5 Observations/Results

Figures 2.2, 2.3, and 2.4 show the spectra collected for TNT, RDX, and PETN. Table 2.1 gives the infrared absorbance strengths in several different useful units. Included with the standard integrated values are the band peak absorption coefficients and absorption cross sections. These numbers have been very valuable in assessing the potential of the Kerr effect and the other techniques, such as the Varian capillary absorption cell and infrared cavity ringdown.

In the case of TNT, the NO_2 stretches were observed at temperatures as low as 353 K. This temperature was well below the 453 K temperature at which TNT, RDX, and PETN were observed to decompose rapidly. Therefore, the spectra of TNT were free of any decomposition products. On the other hand, RDX and PETN both decomposed in the 413-443K temperature range used to generate sufficient vapor pressures (>1mTorr) of these molecules. In fact over the course of some of the longer scans, these decomposition products dominated the spectra. Carbon dioxide appeared to be a major decomposition product based on the appearance of the 2440 cm^{-1} band of this molecule. The decomposition products noted here indicate that the 1320-1370 cm^{-1} feature reported by

Karpowicz and Brill may be due to decomposition during the flash pyrolysis of RDX they used to generate their vapor.[12] Likewise, the 1734 cm^{-1} band reported by Carper may also be a decomposition product in the spectrum of TNT.[13]
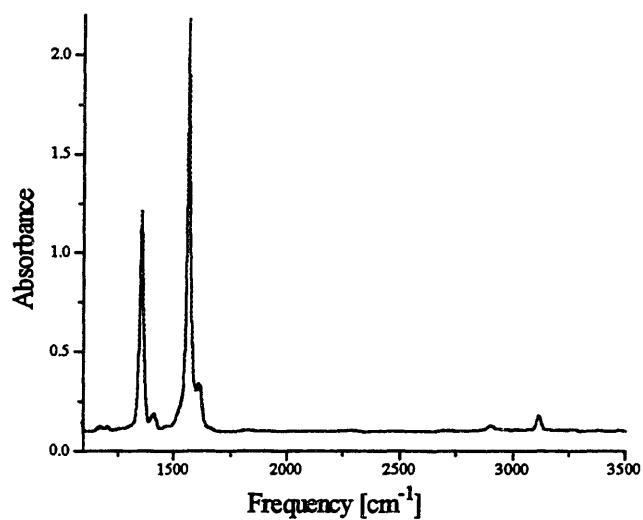
Figure 2.2 Infrared absorption spectrum of trinitrotoluene vapor at 413 K. This molecule did not exhibit any decomposition products in its spectra collected at temperatures ranging from 353-423 K.
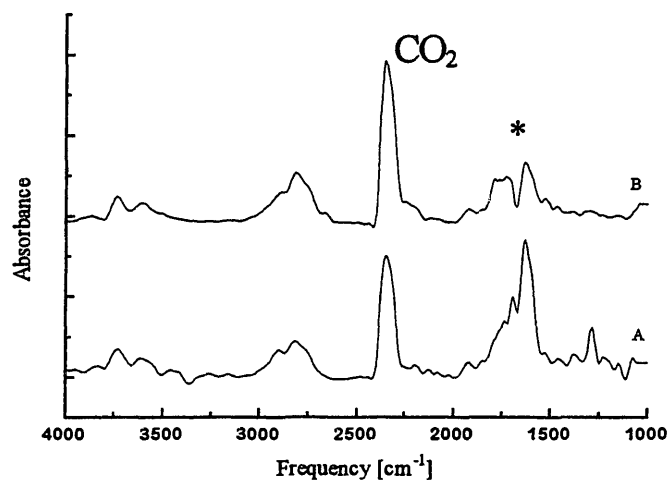
Figure 2.3 Infrared absorption spectrum of PETN vapor (A) at 413 K and (B) PETN vapor plus decomposition products at 433 K. The second spectrum was recorded after more than 20 minutes at this temperature. Both the low temperature spectra contain the CO_2 band at 2440 cm^{-1}. The (*) indicates the decomposition products in (B).
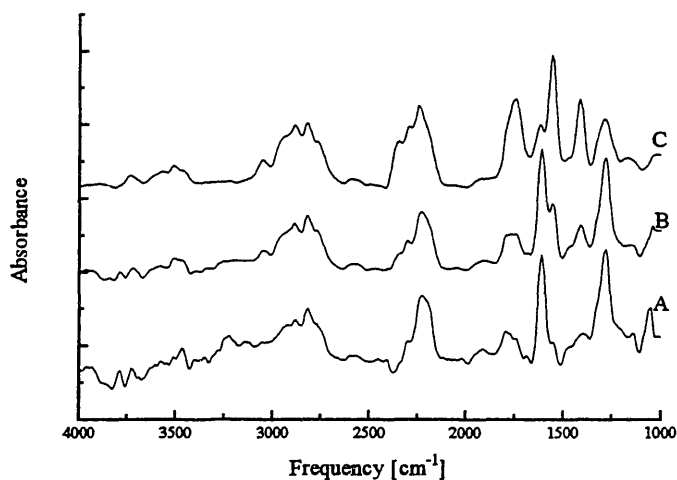
Figure 2.4 Absorption spectra of RDX vapor at (A) 423; (B) 443 and (C) 473 K. The higher temperature spectrum (C) clearly shows the bands for the decomposition products at 1400, 1600 and 2900 cm^{-1}.

Table 2.1

Infrared band intensities of vibrational transitions in mono and trinitrotoulenes, RDX, and PETN

Molecule	Band [cm^{-1}]	Integrated absorption [l cm^{-2} mol^{-1}]	Peak absorption coefficient [cm^2 mol^{-1}] x 10^4	Absorption Cross Section [cm^2]x10^{-18}
TNT	1080	383 ± 23	2.67 ± 1.80	0.0443 ± 0.0299
	1349	1.05 ± 0.45 x 10^4	48.3 ± 2.21	0.802 ± 0.367
	1402	648 ± 4	2.90 ± 0.68	0.0482 ± 0.0011
	1559	1.56 ± 0.79 x 10^4	69.5 ± 25.9	1.15 ± 0.43
	1606	1.02 ± 0.01 x 10^4	7.65 ± 1.79	0.127 ± 0.030
	2898	359 ± 20	0.889 ± 0.272	0.0148 ± 0.0045
	3107	642 ± 127	2.43 ± 0.54	0.0404 ± 0.0090
RDX	1272	4.17 ± 0.67 x 10^4	77.1 ± 24.3	1.28 ± 0.40
	1602	2.16 ± 0.19 x 10^4	78.0 ± 24.3	1.30 ± 0.40
PETN	1279	4.13 ± 1.14 x 10^4	5.14 ± 1.06	0.0664 ± 0.0176
	1626	2.34 ± 0.30 x 10^4	1.42 ± 0.30	0.0236 ± 0.0050
p-MNT	1216	706 ± 102	20.5 ± 10.2	0.341 ± 0.171
	1356	5.94 ± 0.78 x 10^3	82.5 ± 23.4	1.37 ± 0.39
	1547	5.76 ± 1.12 x 10^3	81.9 ± 25.3	1.36 ± 0.42
	1608	1.38 ± 0.32 x 10^3	43.5 ± 12.6	0.723 ± 0.209
	1737	1.56 ± 0.42 x 10^3	42.2 ± 9.3	0.700 ± 0.155
o-MNT	1216	3.73 ± 0.23 x 10^3	75.9 ± 16.3	1.26 ± 0.27
	1366	4.05 ± 0.13 x 10^3	78.9 ± 18.1	1.31 ± 0.30
	1736	8.15 ± 1.23 x 10^4	99.4 ± 15.7	1.65 ± 0.26

Once the integrated absorbance intensities had been determined, a comparison was made between the vapor pressures recorded by Dionne et al. and the measured absorbance at various temperatures by plotting ln(Absorbance) vs. $1/T$.[14] Figures 2.5, 2.6 and 2.7 show that, within experimental error, there is good agreement between our results and those of Dionne. For the case of TNT the agreement is quantitative. The plot yields a heat of vaporization of 47.2 kJ/mol, in excellent agreement with Dionne's value of 46.0 kJ/mol. The agreement for RDX and PETN is not quantitative because of the buildup of interfering decomposition products.
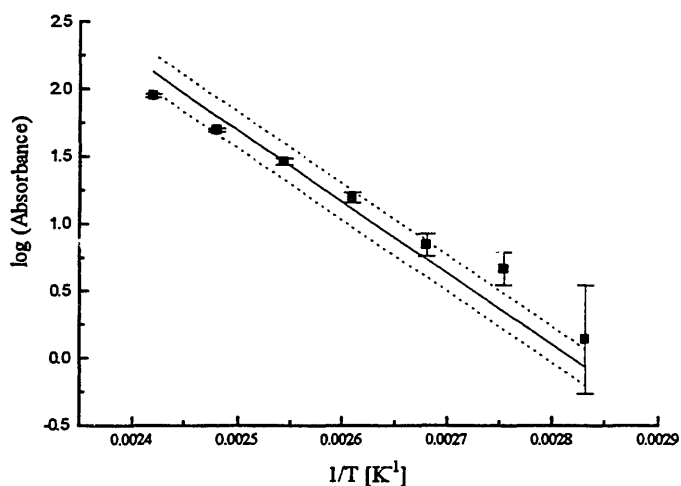
Figure 2.5 Measured TNT integrated infrared absorbance vs. temperature, compared with absorbance predicted from vapor pressures given by Dionne et al..[14]
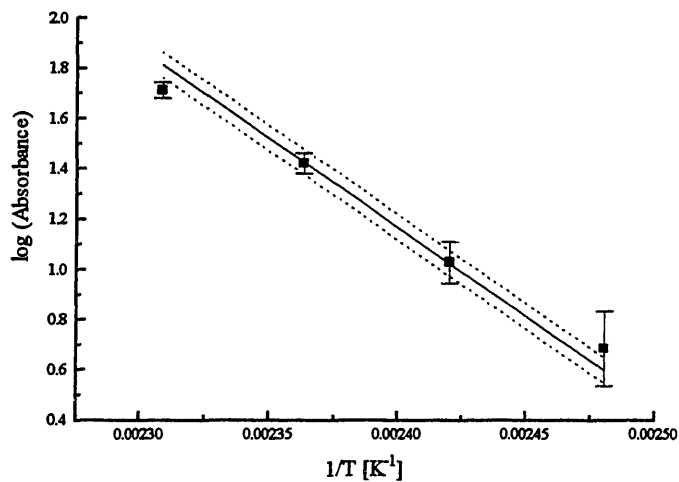
Figure 2.6 Measured PETN integrated infrared absorbance vs. temperature, compared with absorbance predicted from vapor pressures given by Dionne et al..[14]
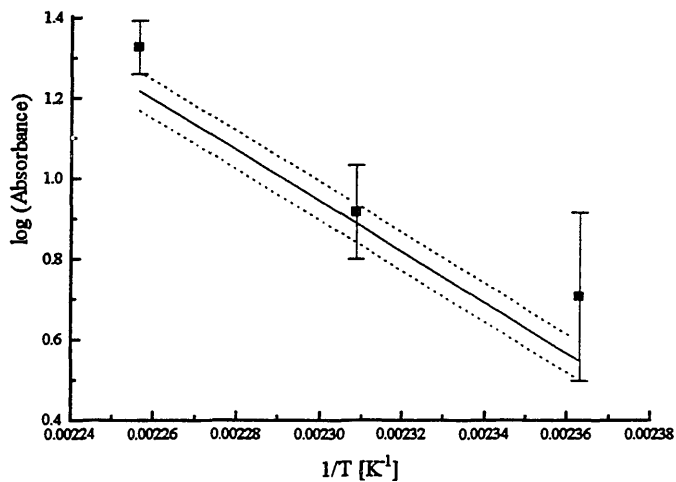
Figure 2.7 Measured RDX integrated infrared absorbance vs. temperature, compared with absorbance predicted from vapor pressures given by Dionne et al..[14]

The geometry of the TNT molecule predicted by our molecular orbital calculations, shown in Figure 2.8, was in excellent agreement with that reported by Chen.[15] Tables 2.2 and 2.3 give a comparison of the angles and bond lengths for both simulations along with x-ray data for the two possible crystal forms of TNT. The only significant difference is in the dihedral angles of ortho NO_2 groups relative to the benzene ring. This is a consequence of the initial dihedral angle constraint used in the preliminary geometry calculation. The molecular orbital calculation also illustrates the asymmetrical arrangement of the ortho NO_2 groups out of the plane of the benzene ring. If these groups are coplanar with the benzene ring and the para NO_2 remains in the plane, the molecule would not have a dipole moment. Since the Kerr effect is dependent on the size of the dipole moment, the calculated geometry along with dipole measurements made on this molecule are crucial for evaluation of feasibility of Kerr effect TNT detection.

The correlation between observed and calculated frequencies for both the infrared and Raman spectra were made based on the intensities of the modes. Table 2.4 compares the results of the calculations with the observed frequencies and intensities for the infrared spectrum. The higher values for the calculated frequencies is typical of this level of calculation and is due to basis set truncation and neglect of electron correlation. Scaled force constants are often used to correct the discrepancy. The scaling typically ranges from a factor of 0.7 to 0.9, which would bring our calculated values into the observed range as indicated by the ratios in the table. Table 2.5 compares the Raman frequencies and intensities calculated using Gaussian 94 with those collected in the Steinfeld lab and

by Buldakov et al..[16] The same scaling factors, used in analyzing the infrared frequencies, apply to the Raman frequencies as well.

Figure 2.8 The geometry of the explosive TNT was calculated using Gaussian 94 with the STO3G basis set. Bonds marked with arrows in the figure are out of the aromatic ring plane. Atoms numbered 1,2,3,5,6, 9, and 10 are carbons; atoms numbered 7,8, and 16 are nitrogen; atoms numbered 4,15,17,18, and 19 are hydrogen; atoms 11,12,13,14,20, and 21 are oxygen. Oxygens 21, 19, an 11 are above the plane, while oxygens 12, 17, and 20 are below the plane. The numbering of the atoms is consistent with the angles and bonds given in tables 2.2 and 2.3.

Table 2.2 Comparison of calculated geometries with all bond lengths in 10^{-10} m.[15]

Bond	crystal A	Crystal B	6-31G	6-31G*	6-31G**	This Calculation 6-31G
C6-C3	1.399	1.400	1.404	1.401	1.401	1.398
C3-C1	1.382	1.375	1.381	1.380	1.380	1.380
C1-C2	1.389	1.379	1.377	1.376	1.376	1.376
C2-C5	1.378	1.381	1.376	1.375	1.375	1.376
C5-C9	1.390	1.380	1.382	1.381	1.381	1.380
C9-C6	1.403	1.404	1.401	1.397	1.397	1.398
C6-C10	1.509	1.494	1.519	1.519	1.518	1.514
C10-H19			1.071	1.073	1.073	1.078
C10-H17			1.079	1.081	1.081	1.082
C10-H18			1.079	1.080	1.080	1.078
C3-N8	1.475	1.486	1.455	1.464	1.464	1.463
N8-O12	1.225	1.228	1.223	1.191	1.191	1.191
N8-O11			1.226	1.192	1.192	1.191
C1-H4			1.069	1.070	1.070	1.071
C2-N7	1.475	1.467	1.445	1.456	1.456	1.456
N7-O14			1.223	1.191	1.191	1.191
N7-O13			1.224	1.191	1.191	1.191
C5-H15			1.070	1.071	1.071	1.071
C9-N16	1.475	1.482	1.457	1.466	1.466	1.463
N16-O20			1.233	1.191	1.191	1.191
N16-O21			1.233	1.191	1.191	1.191

Table 2.3 Comparison of calculated geometries[15]

Angle	Crystal A	Crystal B	6-31G	6-31G*	6-31G**	This Calculation 6-31G
C3-C6-C9	113.6	112.6	114.1	114.0	113.9	114.1
C6-C3-C1	125.7	126.4	123.8	124.0	124.1	124.0
C3-C1-C2	116.4	116.1	118.6	118.4	118.3	118.2
C1-C2-C5	122.7	122.8	121.0	121.1	121.2	121.3
C2-C5-C9	117.4	117.4	118.6	118.4	118.4	118.3
C5-C9-C6	124.3	124.7	123.9	124.1	124.1	124.0
C6-C10-H19			110.5	110.5	110.5	110.6
C6-C10-H17			109.3	109.2	109.2	110.1
C6-C10-H19			108.6	108.6	108.6	110.6
C6-C3-N8	118.9	117.8	121.6	121.3	121.3	121.0
C1-C3-N8	115.6	115.8	114.6	114.7	114.6	115.0
C3-N8-O12	117.5	117.4	119.1	118.2	118.2	117.7
C3-N8-O11			117.1	116.6	116.6	116.9
O12-N8-O11	125.0	125.2	123.8	125.2	125.2	125.4
C3-C1-H4			120.8	120.7	120.7	120.7
C1-C2-N7	118.3	118.4	119.5	119.5	119.4	119.4
C2-N7-O14			117.8	117.2	117.2	117.2
C2-N7-O13			117.7	117.2	117.2	117.2
O14-N7-O13			124.5	125.7	125.7	125.6
C2-C5-H15			120.7	120.9	120.9	121.3
C5-C9-N16	116.1	115.8	113.9	113.9	113.9	115.0
C9-N16-O21			119.2	118.3	118.3	117.6
C9-N16-O20			116.7	116.2	116.2	116.9
O20-N16-O21			124.1	125.5	125.5	125.4
C6-C9-N16	119.6	119.5	122.3	122.0	122.0	121.0

Table 2.4 Comparison of calculated and observed infrared intensities for TNT

Observed infrared frequency [cm^{-1}]	Calculated infrared frequency [cm^{-1}] (unscaled)	Measured Relative Intensity	Total Calculated Relative Intensity	Assignment
1349	1651, 1654	0.673	0.414	NO$_2$ Symmetric Stretch
1559	1880, 1883	1.00	1.00	NO$_2$ Asymmetric Stretch
2898	3244, 3324, 3348	0.023	0.098	Methyl C-H Stretch
3107	3440, 3441	0.041	0.0377	Ring C-H Stretch

Table 2.5 Comparison of the calculated Raman shift frequencies with observed frequencies.

Observed Raman Shift Frequency ν^{16}	Observed Raman Shift ν TNT^{17}	Calculated Raman Shift ν	Assignment
	785.7	870	Ring Mode
	836.6	891,894	Ring Mode, ortho-NO$_2$ Torsion
904	909.9	1061	Ring Mode
935		1061	Ring Mode
1082		1207	Meta H Wag
1169		1289,1294	Symmetric and Asymmetric C-H stretches of meta H
1206		1336	Ring Mode
1354	1346	1654,1660	NO$_2$ Symmetric Stretch
1619		1764,1797	NO$_2$ Asymmetric Stretch

References

[1] F Pristera, M. Halik, A. Castelli, W.Fredericks, *Anal. Chem.* 32 (1960) 495.

[2] D.E. Chasan, G. Norwitz, *Microchem. J.* 17 (1972) 31.

[3] Z. Iqbal, K. Suryanararayanan, S. Bulusu, J.R. Autera, "Infrared and Raman Spectra of 1,3,5-trinitro-1,3,5-triazacyclohexane," Report AD-752899, Picatinny Arsenal, NJ, 1972.

[4] J. Akhavan, *Spectrochim. Acta* 47A (1991) 1347.

[5] F.W.S. Carver, T.J. Sinclair *J. Raman Spectrosc.* 14 (1983) 410.

[6] K. L. Mcnesby, J.E. Wolfe, J.B. Morris, R.A. Pesce-Rodriguez, *J. Raman Spectrosc.* 27 (1996) 97.

[7] I. R. Lewis, N.W. Daniel Jr., N.C. Chaffin, P.R. Giriffiths, M.W. Tungol, *Spectrochim. Acta* 51A (1995) 1985.

[8] Microsoft Excel Version 5.0, Microsoft, Redmond WA.

[9] Origin Version 3.0, Microcal Software, Inc., Northampton, MA.

[10] M.J. Frisch, G.W. Trucks, H.B. Schlegel, P.M.W. Gill, B.G. Johnson, M.A. Robb, J.R. Cheeseman, T. Keith, G.A Petersson, H.A. Montgomery, . Raghavachari, M.A. Al-Laham, V.G. Zakrzewski, J.V. Ortiz, J.G. Foresman, J. Cioslowski, B.B. Stefanov, A. Nanayakkara, M. Challacombe, C.Y. Peng, P.Y. Ayala, W. Chen, M.W. Wong, J.L. Andres, E.S. Replogle, R. Gomperts, R.L. Martin, D.J. Fox, J.S. Binkley, D.J. Defrees, J. Baker, J.P. Stewart, M. Head-Gordon, C. Gonzalez, J.A. Polple, Gaussian '94, Revision C.2 Gaussian, Inc., Pittsburgh, PA 1995.

[11] Quanta Version 4.0, Molecular Simulations, Inc., Burlington MA.

[12] R.J. Karpowicz, T.B. Brill, *J. Phys. Chem.* 88 (1984) 348.

[13] W.R. Carper, S.R. Bosco, J.J.P. Stewart, *Spectrochim. Acta* 42A (1986) 13.

[14] B.C. Dionne, D.P. Rounbehler, E.K. Achter, J.R. Hobbs, D.H. Fine, *J. Energetic Mater.* 4 (1986) 447.

[15] P.C. Chen, *J. Chin. Chem. Soc.* 42 (1995) 755.

[16] M.A. Bulgakov, I.I. Ippolitov, B.V. Korolev, I.I. Matrosov, A.E. Cheglokov, V.N. Cherepanov, Yu.S. Akushkin, O.N. Ulenikov, *Spectrochim. Acta* 52A (1996) 995.

[17] B. Gilbert, J. Janni, unpublished .

Chapter Three

Basic Kerr Concepts

3.1 Introduction

Fundamentally, the field of spectroscopy investigates the changes that occur in light and the medium in which it is propagating as they interact. The interaction between light and material begins with the response of charged particles to light's oscillating fields. In this chapter, the response of electrons to light is considered as manifest in the processes of absorption and dispersion. Unlike conventional absorption spectroscopy which is concerned only with the first, Kerr spectroscopy is also dependent on the phase changes due to the second phenomenon, dispersion. Fortunately, both phenomena can be accounted for by the expressions developed for linear absorption.

In this chapter the Kerr effect is discussed in the simple framework of linear absorption because of the familiarity of the framework and because of the potential for understanding the importance of absorption and dispersion simultaneously. The development will start with a simple classical model of a bound charge in an oscillating light field. From this model, expressions for absorption and dispersion as a function of light frequency will be derived. This will be followed by a derivation of the descriptions of absorption and dispersion as a function of frequency through time-dependent perturbation theory.

The derivation for both absorption and dispersion is limited to linear polarizability. Although the expressions derived in this chapter will not be able to account quantitatively for the Kerr effect, they provide an excellent model of dichroism and birefringence in an anisotropic medium without introduction of unnecessary complexity related to orienting polar molecules in a static electric field. In the pedagogical model for the Kerr effect outlined in this chapter, orientation of the molecule is accounted for by a perfectly aligned ensemble of molecules with transitions allowed parallel to the applied field. The ensemble is transparent perpendicular to the static electric field.

Finally, a Jones matrix treatment based on the results of the two derivations for absorption and dispersion will be applied to the classical Kerr measurement apparatus. The expressions resulting from the Jones matrices will give the wavelength and polarization dependence of the intensity of the light passing through the Kerr apparatus as it is affected not only by linear dichroism but also linear birefringence.

3.2 Classical Treatment

The classical treatment of this problem begins with considering an electron bound to a molecule or atom, as illustrated in Fig. 3.1, with a restoring force which is a function of displacement. Simple expressions can be derived for the position and motion of this electron with and without an oscillating electric field. Without the applied field the equation of motion can be derived through the well-known differential Eq. (3.2.1) describing the motion of a harmonic oscillator.

$$m_e \frac{d^2q}{dt^2} + k_r q = 0. \qquad\qquad (3.2.1)$$

In this expression m_e is the mass of the electron, q is the position of the electron and k_r is the restoring force constant acting on the electron. The solution to this differential equation indicates periodic motion starting at some initial displacement, q_0.

$$q = q_0 \cos\omega_i t. \qquad\qquad (3.2.2)$$

$$\omega_i = \sqrt{\frac{k_r}{m_e}}. \qquad\qquad (3.2.3)$$
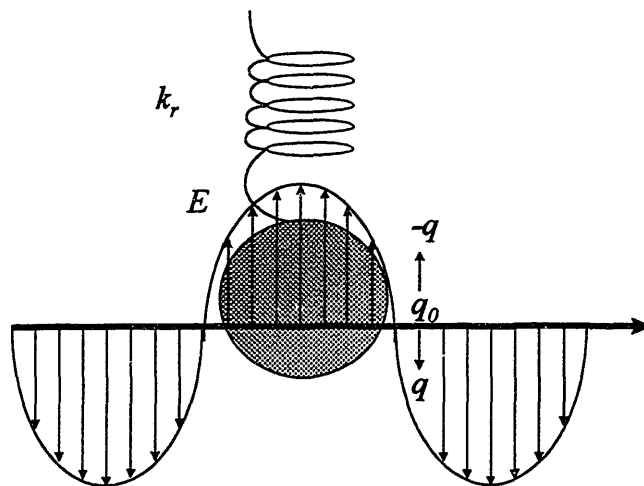
Figure 3.1 The classical approach to deriving expressions for absorption and dispersion as a function of frequency begins with an electron bound to a molecule or atom with a harmonic potential. The resulting restoring force is $-k_r q$.

The charge-on-a-spring model can be extended to include energy dissipation processes in the motion of the electron such as conversion to heat or light . A damping

47

coefficient, Γ, is introduced into Eq. (3.2.1) to account for these processes, so that the differential equation for the motion of the electron becomes,

$$m_e \frac{d^2 q}{dt^2} + \Gamma m_e \frac{dq}{dt} + k_r q = 0.$$ (3.2.4)

For the dissipative system the solution to the differential equation given in Eq. (3.2.5) indicates that when ω_d from Eq. (3.2.6) is put into Eq. (3.2.5) the oscillation dies out exponentially as a function of $-\Gamma t$.

$$q = q_0 e^{-\Gamma t} \cos \omega_d t$$ (3.2.5)

$$\omega_d = \frac{\sqrt{4 m_e k_r + \Gamma}}{2 m_e}$$ (3.2.6)

This damped, charged harmonic oscillator is now acted on by an oscillating electric field, $E = E_0 e^{i\omega t}$ with the electric field parallel to the motion of the electron as indicated in Figure 3.1. The differential equation describing the motion of the electron is now,

$$m_e \frac{d^2 q}{dt^2} + \Gamma m_e \frac{dq}{dt} + k_r q = e E_0 e^{i\omega t}.$$ (3.2.7)

The displacement of the electron at the frequency of the driving force is

48

$$q = \mathrm{Re}\left[m_e e^{i\omega t}\left(\frac{(\omega_i^2 - \omega^2)}{(\omega_i^2 - \omega^2)^2 + \omega^2\Gamma^2} - \frac{i\omega\Gamma}{(\omega_i^2 - \omega^2)^2 + \omega^2\Gamma^2} \right) \right]. \qquad (3.2.8)$$

The current expression, Eq. (3.2.8), for q indicates that energy can be transferred from the light to the electron's motion. This energy is then dissipated from the system via conversion to heat or light. In this way energy from the impinging light is absorbed. This model also accounts for changes in the phase of the light as it traverses the charged oscillator. Because the resultant light field is a superposition of the incident field and the local electron field, the phase changes result from the modulation of the local field by the motion of the electron. As the frequency dependence of q given in Eq. (3.2.8) indicates, both absorption and dispersion phenomena are more pronounced as the motion of the electron becomes resonant with the light field.

Using the results of Maxwell's equations for the propagation of light in an insulating and electrically neutral medium, a differential equation, Eq. (3.2.9), can be derived that when solved gives the spatial and temporal dependence of the electric field of light.

$$\frac{\partial^2 E}{\partial y^2} = \varepsilon_0\mu_0\frac{\partial^2 E}{\partial t^2} + \mu_0\frac{\partial^2 \Pi}{\partial t^2}. \qquad (3.2.9)$$

The constants ε_0 and μ_0 in Eq. (3.2.9) are the permittivity and permeability of vacuum respectively. The unusual convention of light propagating along the y axis was chosen to keep the labels of the axes consistent throughout this treatment of the Kerr effect.

This differential equation for the propagation of light, Eq. (3.2.9), has as one of its terms the second partial derivative of the bulk polarizability, Π, with respect to time. This bulk polarizability will now be derived as a function of the displacement of the electron, q. If the polarizability of a molecule is defined as the change in the dipole moment induced by an applied field, the expressions obtained for the position, Eq. (3.2.8), of the bound electron in an oscillating field as a function of time can be used to derive a bulk polarizability via a sum over the ensemble of electrons that make up the medium. In order to generate a dipole, the bound electron is considered to be separated from a positive charge, as would be the case in an atom or molecule. Therefore, changes in position of the electron represent a change in the dipole moment proportional to the applied light field. If an array of these oscillating charges is considered, an expression for the bulk polarizability, $\overline{\Pi}$, of a medium constructed of a collection of these oscillators can be developed from a summation over an ensemble of the oscillating dipoles,

$$\overline{\Pi} = N_e \sum_i \frac{m_e e^2 E_0 e^{i\omega t} f_i}{\omega_i^2 - \omega^2 + i\Gamma\omega}. \tag{3.2.10}$$

In this expression, the proportionality constant f_i was added to account for the various orientations of the oscillators relative to the oscillating field, their respective phase with

the field and their response to this field. The terms k_r/m_e were replaced with frequencies ω_i^2, which are the fundamental frequencies of the N_e oscillators in the medium, where N_e is the number of oscillators encountered by the propagating light.

Returning to Maxwell's equations, the expression for the bulk polarizability can be used to calculate the temporal and spatial dependence of light's electric field in the medium. Using the standard plane wave solution to this equation, Eq. (3.2.11), the k term is now given by Eq. (3.2.12).

$$E = E_0 e^{i(\omega t - kv)}.$$ (3.2.11)

$$k = \omega \sqrt{\varepsilon_0 \mu_0} \left(1 + \tfrac{1}{2} \sum_i \frac{m_e e^2 f_i}{\varepsilon_0 (\omega^2_i - \omega^2 + i\Gamma\omega)}\right).$$ (3.2.12)

The approximation $\sqrt{1+y} = 1 + \tfrac{1}{2}y$ when $y \ll 1$ was made in Eq. (3.2.12). Next, the expression for k is separated into real and imaginary components k' and k'':

$$k = k' + ik'',$$ (3.2.13)

$$k' = \frac{\omega}{c} + N_e m_e e^2 f_i \frac{\omega(\omega_i^2 - \omega^2)}{\varepsilon_0 c((\omega_i^2 - \omega^2)^2 + \Gamma^2\omega^2)},$$ (3.2.14)

$$k'' = N_e m_e e^2 f_i \frac{\Gamma\omega^2}{\varepsilon_0 c((\omega_i^2 - \omega^2)^2 + \Gamma^2\omega^2)}.$$ (3.2.15)

The substitution of $\sqrt{\varepsilon_0 \omega_0} = c$ was made, where c is the speed of light. The electric field then as a function of time and propagation distance is

$$E = E_0 e^{-k''y} e^{i(\omega t - k'y)}. \tag{3.2.16}$$

Equation (3.2.16) indicates that, near resonance between the light and charged oscillator frequencies, the light intensity decreases exponentially as a function of pathlength, y. The frequency dependence of this absorption is the expected Lorentzian function for a transition (Eq. (3.2.15)) with homogenous broadening. Equally important to the Kerr effect, however, is the corresponding phase factor as a function of distance, that occurs in the second half of Eq. (3.2.16).

The above classical framework expressions for both dispersion and absorption were simultaneously derived and are sufficient for describing linear polarizabilities and the effect they have on the propagation properties. To extend these ideas to include quantum mechanical and non-linear processes, it is useful to look at this same problem from a time-dependent perturbation theory approach.

3.3 Time Dependent Perturbation Approach

In this approach, derivation of the molecular polarizability will be the first task. In an ensemble of molecules the bulk polarization is proportional to the mean electric dipole moment, so the dipole moment for a single molecule as a function of the perturbing field

will be calculated followed by an average over a collection of molecules or atoms. Particular attention is paid to the superposition of contributions from individual molecules at a random distribution of spatial locations. The dipole moment for a single molecule can be calculated through the dipole moment operator taken between the wave functions perturbed by the oscillating field.

In this case the perturbation will be the light field, so that the perturbation term in the Hamiltonian will be $H' = \mu_\xi \cdot E_0 \cos \omega t$, where μ_ξ is the dipole moment operator along ξ in the laboratory frame. This perturbing field yields Eq. (3.3.1)

$$\mu_\xi(t) = e^{i\omega_{io}t}\langle i|\mu_\xi|o\rangle + \frac{1}{2\hbar}\sum_{\pm}e^{i(\omega_{io}\pm\omega)t}\sum_{j}\left[\frac{\langle i|\mu_\xi|j\rangle\langle j|\mu_\eta|o\rangle}{\Omega_{jo}\pm\omega} + \frac{\langle i|\mu_\xi|j\rangle\langle j|\mu_\eta|o\rangle}{\Omega_{ji}^{*}\mp\omega}\right]E_{o\eta} + \ldots$$

,

(3.3.1)

which gives the dipole moment in an oscillating field up to a linear dependence on the field. In this expression, ω_{io} is the frequency corresponding to the energy difference between states $\langle i|$ and $\langle o|$ given in Eq. (3.3.2).

$$\hbar\omega_{io} = E_i - E_o.$$

(3.3.2)

Likewise, the term $\Omega_{jo,ji}$ is

$$\hbar\Omega_{jo,ji} = \hbar(\omega_{jo,ji} - 1/2i\Gamma_{jo,ji}) = E_j - E_{o,i} - i\Gamma_{jo,ji}\hbar/2, \qquad (3.3.3)$$

where $\Gamma_{jo,ji}$ is the damping term. The directions ξ and η are the laboratory frame axes Z or X. The frequency of the incident radiation is ω and its polarization is given by the direction ξ. Because the Kerr effect near a transition between the ground state, $\langle o|$, and a state $\langle j|$ is considered, states $\langle i|$ and $\langle o|$ in Eq. (3.3.1) are the ground state $\langle o|$. Making the substitutions for the states and their energies, the only time dependent term that appears in Eq. (3.3.1) appears after the summation. Equation (3.3.4) gives the time dependent dipole moment needed to calculate the mean molecular polarizability.

$$\mu_\xi(t) = E_0 \cos\omega t \left(\frac{2\omega_{jo}(\omega_{jo}^2 - \omega^2 + \frac{1}{4}\Gamma_{jo}^2)\langle o|\mu_\xi|j\rangle\langle j|\mu_\eta|o\rangle}{(\omega_{jo}^2 - \omega^2 + \frac{1}{4}\Gamma_{jo}^2)^2 + \omega^2\Gamma_{jo}^2} \right)$$

$$- iE_0 \sin\omega t \left(\frac{i\omega_{jo}\omega\Gamma\langle o|\mu_\xi|j\rangle\langle j|\mu_\eta|o\rangle}{(\omega_{jo}^2 - \omega^2 + \frac{1}{4}\Gamma_{jo}^2)^2 + \omega^2\Gamma_{jo}^2} \right). \qquad (3.3.4)$$

The terms in the parentheses are the polarizabilites, Π, so that the resulting k will have real and imaginary components as was the case for the classical treatment. Plugging Eq. (3.3.2) for the time dependent perturbation derived polarizability into Maxwell's Eq. (3.2.9), and summing over a collection of N_e molecules,

$$k' = \frac{\omega}{c} + \frac{2N_e\omega^2\omega_{jo}(\omega_{jo}^2 - \omega^2 + \frac{1}{4}\Gamma_{jo}^2)\langle o|\mu_\xi|j\rangle\langle j|\mu_\eta|o\rangle}{\varepsilon_0 c\hbar((\omega_{jo}^2 - \omega^2 + \frac{1}{4}\Gamma_{jo}^2)^2 + \omega^2\Gamma_{jo}^2)} \qquad (3.3.5)$$

$$\text{and } k'' = \frac{2N_e\omega\omega_{jo}\Gamma_{jo}\langle o|\mu_\xi|j\rangle\langle j|\mu_\eta|o\rangle}{\varepsilon_0 c\hbar((\omega_{jo}^2 - \omega^2 + \frac{1}{4}\Gamma_{jo}^2)^2 + \omega^2\Gamma_{jo}^2)} . \qquad (3.3.6)$$

These equations can be made to look exactly like Eqs. (3.2.14) and (3.2.15) by making the approximation that Γ is much smaller than the frequencies ω_{jo} and ω, which is the case for most transitions.

Both the classical treatment of a charged harmonic oscillator and the time-dependent perturbation theory treatment of the response of a medium to an oscillating light field indicate the importance of both dispersion and absorption in describing the transmitted radiation. This relationship can be demonstrated in a third way through the application of the Kramers-Kronig relationship between the real and imaginary response of a system.[1,2] The extension of the time-dependent theory to include non-linear terms in the perturbing field will yield the same connection between the two phenomena. Therefore, the derivations presented here give the expected relationships between dispersion and absorption in the simplest case with indications for how to extend the calculations to include non-linear terms. The stage is now set for investigating the changes that occur in a beam of polarized light as it propagates through a medium with a transition allowed parallel to an applied static electric field.

3.4 Jones Matrix Approach to the Kerr Effect

Any consideration of the Kerr effect must start with a description of the changes that occur in polarized light as it passes through an anistropic medium. As indicated by the parallelism between dispersion and absorption given above, both absorption and dispersion are considered in the Jones Matrix description of the change in polarization.[3] The Jones Matrices transform a vector describing the initial polarization of light into a vector which describes the final polarization. The polarization transformation accounts for dispersion and absorption through exponential matrix elements that closely resemble the Beer-Lambert factors which describe linear absorption. However, the Jones Matrices include terms that result in a change in the phase as well as the intensity of the light as a function of propagation distance. The description of polarized light as a vector and the matrices that account for linear dispersion will be the subject of this section.
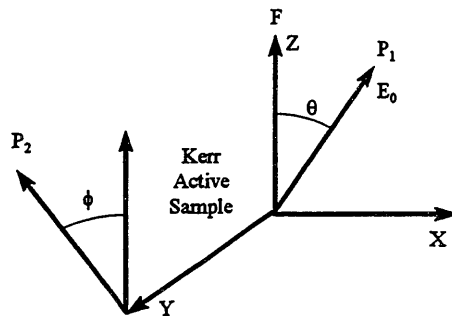
Figure 3.2 The Kerr effect is the optical anistropy induced in a material through the application of an electric field (F), in this case along the Z axis. Light linearly polarized as specified by the polarizer axis, P_1, propagates through the anistropic medium, and the resultant polarization is analyzed by a second polarizer, P_2. The angles θ and ϕ are, respectively, angles between the applied field and the polarizer axes.

As was the case in the derivation of the equations that described dispersion and absorption, consideration is given to the electric field component of light which propagates through the medium in the applied field. Figure 3.2 demonstrates the arrangement of the polarizers, anistropic medium, and the applied field. The unusual convention of light propagating along the Y-axis is used so that the external electric field, F, can be specified along the Z-axis. The axis system in this analysis is left-handed so that positive y is out of the page. Equation (3.4.1) describes the electric field of the light in the medium,

$$E = E_0 e^{i(ky-\omega t)}(a\hat{j} + b\hat{i}). \tag{3.4.1}$$

The coefficients a and b are the projections of the electric field of the light on the axes Z and X defined by a polarizer with a tilt angle θ with respect to the applied field, see Figure 3.2. Expressing the polarization of the light in the Jones Matrix convention yields the following polarization vector, Eq. (3.4.2),

$$E = E_0 e^{i(ky-\omega t)}\begin{pmatrix} \cos\theta \\ \sin\theta \end{pmatrix}. \tag{3.4.2}$$

Next the anisotropic medium, which is linearly birefringent and dichroic, is incorporated by the Jones Matrix below, Eq. (3.4.3), where the term D accounts for both phenomena.

$$E = E_0 e^{i(\omega t)} \begin{pmatrix} e^{iD_z} & 0 \\ 0 & e^{iD_x} \end{pmatrix} \begin{pmatrix} \cos\theta \\ \sin\theta \end{pmatrix}, \tag{3.4.3}$$

where,

$$D_{z,x} = \varepsilon' + i\varepsilon'' = k'_{z,x}y + ik''_{z,x}y . \tag{3.4.4}$$

Finally a second polarizer with the angle ϕ with respect to the applied field is added to the setup. The light field exiting the last polarizer is:

$$E_{det} = (\cos\phi \ \sin\phi) E_0 e^{i\omega t} \begin{pmatrix} e^{iD_z} & 0 \\ 0 & e^{iD_x} \end{pmatrix} \begin{pmatrix} \cos\theta \\ \sin\theta \end{pmatrix}, \tag{3.4.5}$$

$$E_{det} = E_0 e^{i\omega t} (\cos\theta\cos\phi e^{iD_z} + \sin\theta\sin\phi e^{iD_x}) . \tag{3.4.6}$$

The intensity, Eq. (3.4.7), of the light after the analyzer polarizer is the square modulus of the light electric field.

$$I = c\varepsilon_0 E * E_{det} , \tag{3.4.7}$$

where c is the speed of light and ε_0 is the permittivity of vacuum. Taking the square modulus of Eq. (3.4.6), the intensity is

$$I = \varepsilon_0 c E_0^2 (cos^2 \theta \cos^2 \phi e^{-2\varepsilon_z''} cos^2(2\varepsilon_z' - 2\omega t) + sin^2 \theta \sin^2 \phi e^{-2\varepsilon_x''} cos^2(2\varepsilon_x' - 2\omega t)$$
$$+ 1/2 \sin 2\theta \sin 2\phi e^{-(\varepsilon_z'' + \varepsilon_x'')} cos(\varepsilon_z' - \omega t) cos(\varepsilon_x' - \omega t))$$

(3.4.8)

Since the detector is not sufficiently fast to respond to the optical frequencies, an average over a period T is taken via Eq. (3.4.9).

$$I_{det} = \frac{1}{T} \int_0^T I dt$$

(3.4.9)

Performing this integration, one obtains the result that the signal measured on the detector is proportional to the intensity I_{det},

$$I_{det} = \frac{\varepsilon_0 c E_0^2}{2} (cos^2 \theta \cos^2 \phi e^{-2\varepsilon_z''} + sin^2 \theta \sin^2 \phi e^{-2\varepsilon_x''}$$

$$+ 1/2 \sin 2\theta \sin 2\phi \cos(\varepsilon_z' - \varepsilon_x') e^{-(\varepsilon_z'' + \varepsilon_x'')}).$$

(3.4.10)

In the classic Kerr setup, the axes of the polarizers are set at $\pm 45°$ with respect to the applied field so that Eq. (3.4.10) becomes Eq. (3.4.11):

$$I_{det} = \frac{E_0^{\ 2}}{4}(e^{-2\varepsilon_z''} + e^{-2\varepsilon_x''} - 2e^{-(\varepsilon_z'' + \varepsilon_x'')}\cos(\varepsilon_z' - \varepsilon_x')).$$ (3.4.11)

The expression Eq. (3.4.11) for the intensity of light is based on perfect polarizers, which is a particularly inaccurate description of polarizers in the infrared, so a term must be added to the Eq. (3.4.11) for the transmission of the crossed polarizers. The transmission of the crossed polarizers is accounted for with the term T_r. Equation (3.4.12) indicates the signal measured on a detector through the Kerr apparatus.

$$I_{det} = \frac{I_0}{2}(T_r + e^{-2\varepsilon_z''} + e^{-2\varepsilon_x''} - 2e^{-(\varepsilon_z'' + \varepsilon_x'')}\cos(\varepsilon_z' - \varepsilon_x')).$$ (3.4.12)

This last expression shows clearly the importance of considering both birefringence and dichroism. Materials that are dichroic are necessarily birefringent. The relationship between the dichroism and the birefringence was derived earlier for a simple system.

One final scenario must be considered as it describes the Kerr measurement apparatus for nitromethane. In the Kerr measurement apparatus described later, the light was depolarized by reflections from the metal Stark plates and by the window birefringence. The changes in the phase and intensity of light for the total number of reflections from the plates produced a total depolarization greater than or equal to the molecular birefringence and dichroism. For Kerr apparatus with a background birefringence and linear dichroism signal, Eq. (3.2.12) can be used to describe the

60

transmitted light without the analyte present. In the experiments here the background optical activity was adequately described by a background birefringence B_{back}. With an analyte in the classic Kerr setup the signal was,

$$I_{det} = \frac{I_0 e^{-(\varepsilon''_z + \varepsilon''_x)}}{2}(T_r + e^{-\Delta} + e^{\Delta} - 2\cos(B_{back} + \varepsilon'_z - \varepsilon'_x)), \qquad (3.4.13)$$

where $\Delta = \varepsilon''_z - \varepsilon''_x$. As will be the case in the nitromethane experiments, the dichroism and birefringrence arising from the Kerr effect was less than 50% of the intrinsic birefringence of the setup. For these small Kerr effects, Eq. (3.4.13) reduces to,

$$I_{det} = \frac{I_0 e^{-(\varepsilon''_z + \varepsilon''_x)}}{2}(T_r + \sin^2((B_{back} + \varepsilon'_z - \varepsilon'_x)/2)), \qquad (3.4.14)$$

with $B_{back} \approx 0.1$ Eq. (3.4.14) reduces further to,

$$I_{det} = \frac{I_0 e^{-(\varepsilon''_z + \varepsilon''_x)}}{2}(T_r + \tfrac{1}{4}(B^2_{back} + B_{back}(\varepsilon'_z - \varepsilon'_x) + (\varepsilon'_z - \varepsilon'_x)^2)) \qquad (3.4.15)$$

For small $\varepsilon'_z - \varepsilon'_x < B_{back}$, the signal is linear in the analyte birefringence.

3.5 Simple Kerr Model

In the simplest approximation of the Kerr effect, application of a static electric field leads to an allowed transition with light polarized parallel to this static field. In the simple case there is no corresponding transition with light polarized perpendicular to the applied field. The resulting birefringence and dichroism, probed with light polarized at $\pm$ 45 °, is considered here as a function of frequency. Figure 3.3 illustrates the frequency dependence of the real and imaginary components of the polarizabilities derived in the previous section. Consideration will first be given to a case where the concentration of the analyte, in combination with the applied electric field, produces an absorbance of 0.10 along the z axis. Figure 3.4 shows the intensity of light versus frequency for consideration of only linear dichroism, only linear birefringence and finally both phenomena. With the modest absorption along the z-axis, the predominant effect is linear dichroism. However, the line shape is definitely changed by the contribution from birefringence. In this case, the plane of polarization is slightly rotated towards the X-axis as the polarization component along Z is absorbed. The light is only slightly elliptically polarized under these conditions.

The situation changes as the absorbance along the z-axis is increased to 1. Figure 3.5 illustrates the predominance of the birefringence in this case. At this level of absorbance, the plane of polarization is still being tilted towards the X-axis. However, the resulting birefringence produces elliptically polarized light with a large polarization projection on the analyzer polarizer.

At frequencies where the absorbance along the z-axis is complete, the intensity of light at the detector plateaus at $0.25I_0$. This is the intensity of light that would have been expected if the light were originally polarized along the X-axis. The birefringence in this case exclusively affects the polarization component orthogonal to the X-axis, so there is no change in the X-axis polarization. Figure 3.6 illustrates the plateau. It also indicates the importance of the birefringence of all materials at frequencies near their transition frequency. This birefringence is significant at frequencies far from the transitions and has been postulated as a source of error in predicting the polarizability of molecules in the visible on the basis of Kerr effect measurements for molecules with strong infrared bands. In the case of fluoroform, the vibrational contribution to the visible Kerr effect is estimated at 25% of the observed Kerr signal.[4]
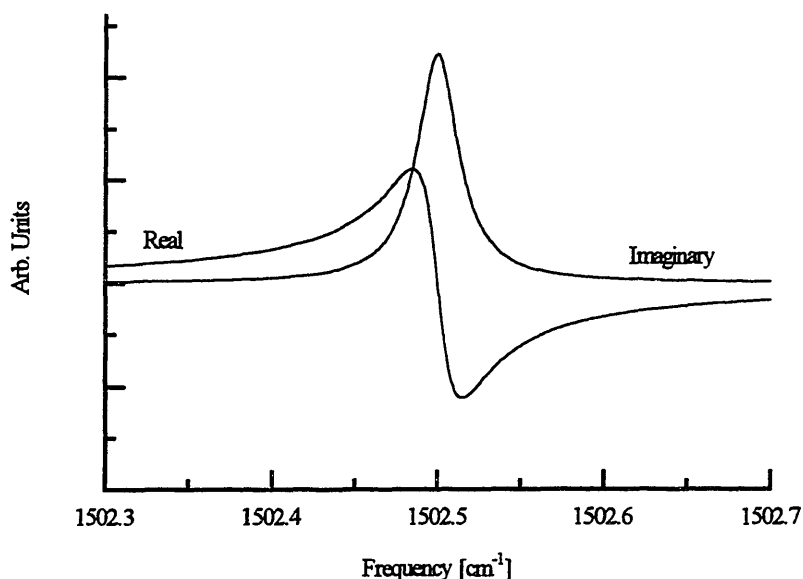
Figure 3.3 The real and imaginary components of the polarizability yield the expected dispersion and absorption curves.
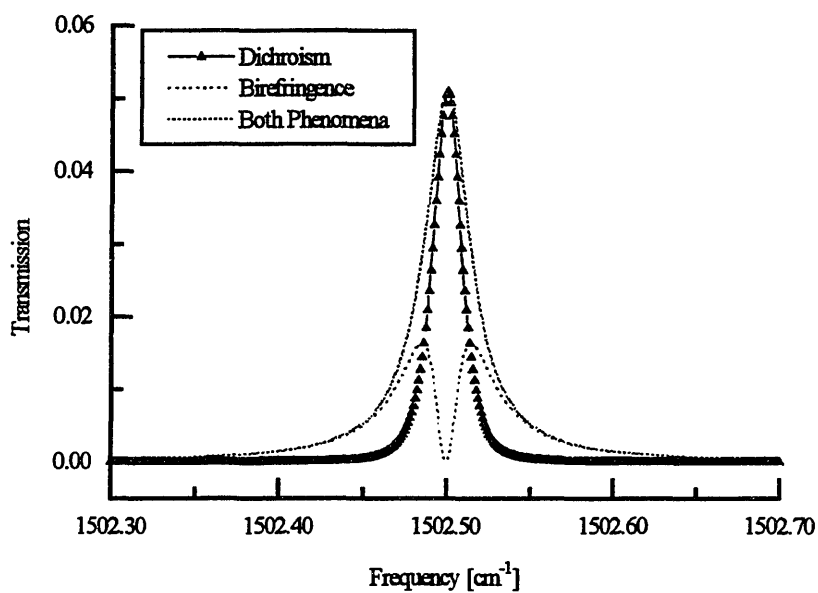
Figure 3.4 For an absorbance of 0.1 along the z-axis, the dichroism seems to dominate the effects leading to transmission of light through crossed polarizers.
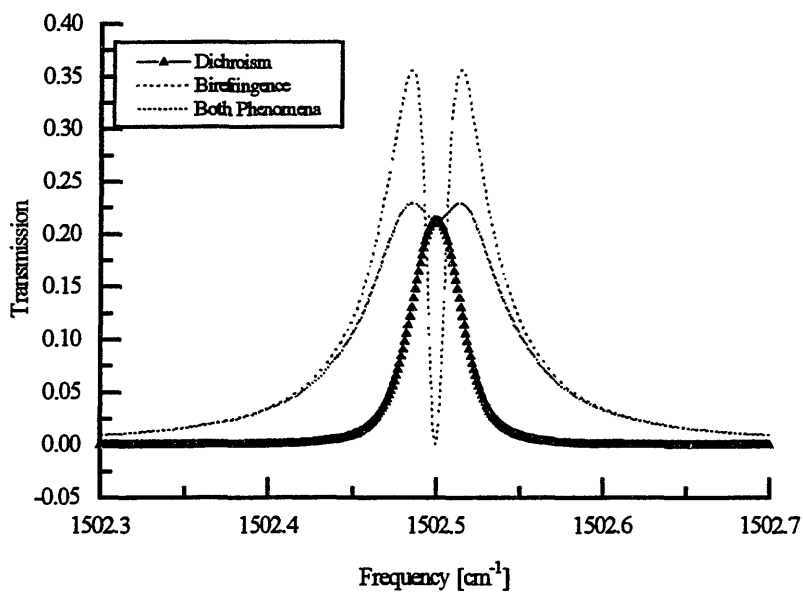
Figure 3.5 The intensity of light through the crossed polarizers near a transition along the z-axis with an absorbance of 1 is dominated by the birefringence.
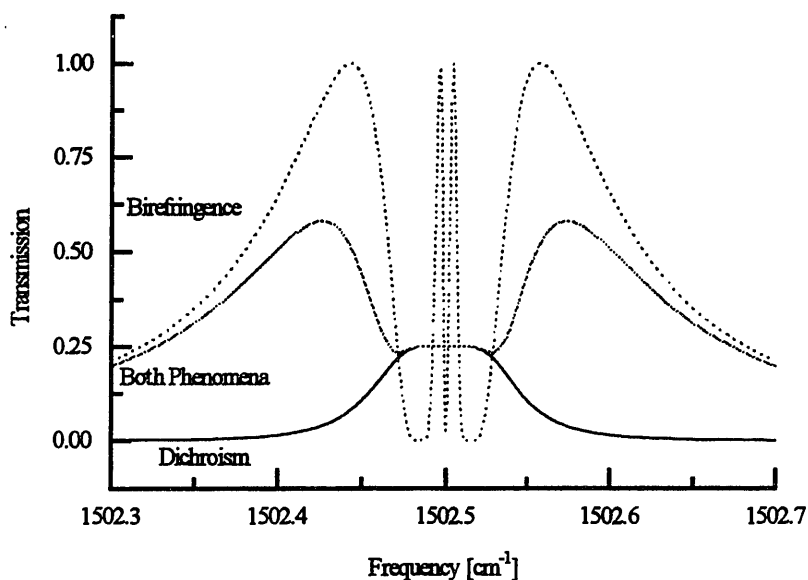
Figure 3.6 At a peak absorbance of 5, the intensity of light through the crossed polarizers plateaus near the peak as the z-component of polarization is completely absorbed. The intensity of light at frequencies very close to the transition frequency is dominated by the birefringence.

References

[1] R.L. Kronig, *J. Opt. Soc. Amer.* 12 (1926) 547.

[2] H.D. Kramers, *Atti. Congr. Int. Fis.* 2 (1927) 545.

[3] R.C. Jones, *J. Opt. Soc. Am.* 31 (1941) 488.

[4] D.M. Bishop, *Mol. Phys.* 42 (1981) 1219.

Chapter Four

Kerr Theory

4.1 Introduction

In the previous chapter, a model for the Kerr effect was developed based on the linear dichroism and birefringence exhibited by a collection of perfectly aligned molecules. Because the emphasis was on the relationship between the two phenomena, transitions were allowed only for light polarized parallel to the applied field. In this chapter the simple oriented transition model is modified by consideration of an ensemble of randomly oriented molecules in the laboratory frame with transitions allowed only along their molecular fixed axes. The applied field leads to Kerr signals through the effect on the fractional orientation of the molecules and through the distortion of the molecular polarizability. Both effects of the field on the optical properties of the medium are included in the derivation of the Kerr signal presented below.

In the next section, a generic electronic or vibrational transition will be considered. The derivation of the Kerr signal will follow the derivation published by A.D. Buckingham with explanation added for clarity.[1-3] Through an expansion of the dipole moment in powers of the static electric field, the molecular polarizability in the applied field is derived. Once a molecule's induced dipole moment has been calculated, the moment is used to calculate its energy in the field. The individual polarizabilities and energy are then

used to calculate the mean molecular polarizability for the bulk medium via a Boltzmann weighted average over all possible orientations of the molecules.

When resolution within an electronic or vibrational band is sufficient for the observation of rotational structure, the classical Boltzmann weighted average must be replaced by a quantum mechanical Boltzmann average over the discrete rotational states. In the third and fourth sections of this chapter, the expressions for the Kerr effect for electronic or vibrational bands with rotational structure are formulated for transitions where the homogeneous linewidth is greater than the Stark frequency shift for a transition. Transitions like the $\tilde{A}^1 A_2 - \tilde{X}^1 A_1 (\pi^* \leftarrow n)$ of formaldehyde considered in this research obey these expressions. For the infrared asymmetric NO_2 stretch of nitromethane, however, the Stark shifts are much greater than the homogeneous linewidth, and so the polarization of each ΔM transition must be considered. Although the resolution considered here is sufficient for observation of the rotational structure, the resolution considered is not sufficiently high for measurement of the Stark splittings. Therefore, the Kerr effect calculated from rotational averaging will depend on a weighted average over the individual M states.

The calculation of the Kerr effect as presented in this chapter differs from the approach taken by other authors who have also considered the problem. In the other treatments, the focus from the start was on the calculation of the energy of the molecules in the applied field. The molecular polarizability was then obtained from an expansion of the energies as powers of the electric field. In the treatment given here, the Kerr effect is derived starting from the previously specified polarizability. The effect of the static field is

incorporated into the expression for the polarizability through perturbations of the wavefunctions and frequencies. Although the approaches differ in their starting points, the results are equivalent. The calculation based on the polarizability, however, provides a direct derivation of the observables from linear absorption. The present derivation of the Kerr effect progresses then from simple classical ideas of an ideally aligned transition to include random orientations of molecules and the field induced distortion of its polarizability.

4.2 Classical Orientation of Molecules in a Static Electric Field

The absorption and dispersion modeled along the molecular axes in Chapter Three could be easily transferred to the spaced fixed axes determined by the electric field and the polarizers because the two axis systems were equivalent. In this section, the molecules are randomly oriented so that the macroscopic properties of dispersion and absorption in the space fixed axis system must be related to the microscopic properties in the molecular frame. In order to consider the molecular properties in the laboratory frame, the relationships between the molecular axes and the space fixed axes must be derived. Use is made of the well known direction cosine matrix which can be used to transform between the two axis systems. Figure 4.1 illustrates the axis system that will be used to calculate the Kerr signal. The space fixed axes determined by the electric field and the polarizers are X, Y, and Z with the field applied parallel to Z. The molecular axes are x, y, and z, with the symmetry axis of the molecule along z. The molecular axes are related to the

space fixed axes through the standard Euler angles, θ, φ, and ϕ. The angle θ is the angle between Z and z. The angles φ and ϕ account for rotation about Z and z, respectively.
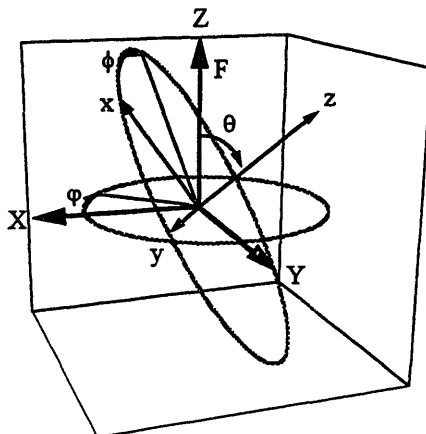
Figure 4.1 The space fixed axes, X, Y, and Z, determined by the applied field, F, are related to the molecular fixed axes, x, y, and z, through the Euler angles θ, φ, and ϕ. The angle θ is the angle between the axes Z and z. The angles φ and ϕ account for rotation about the Z and z axes, respectively.

With the relationship between the molecule and the space fixed axis systems established, the energy of any orientation of a molecule in an electric field is calculated from the projection of the dipole moment along the field axes, $\mu \cos\theta \, F$. Since the dipole moment can be altered by the applied field, the dipole moment is expressed as an expansion in the applied field, as illustrated in Eq. (4.2.1).

$$\mu_\alpha = \mu^o{}_\alpha + \alpha_{\alpha\beta}F_\beta + \beta_{\alpha\beta\eta}F_\beta F_\eta + \gamma_{\alpha\beta\eta\gamma}F_\beta F_\eta F_\gamma + \dots\dots \tag{4.2.1}$$

The term $\mu_\alpha{}^o$ is the zero-field dipole moment, while the terms $\alpha_{\alpha\xi}$, $\beta_{\alpha\xi\eta}$, $\gamma_{\alpha\xi\eta\gamma}$ ...are

tensors which are symmetric in their indices. The indices are the molecular frame axes

(x,y,z). The terms follow the Einstein summation convention for the molecular axes,

where for example,[4]

$$\alpha_{\alpha\beta} = \sum_{\alpha,\beta=x,y,z} \alpha_{\alpha\beta} .$$

(4.2.2)

The energy, then, of a molecule with a given orientation is,

$$U = \mu_\alpha{}^o F_\alpha + \alpha_{\alpha\beta} F_\alpha F_\beta + \beta_{\alpha\beta\eta} F_\alpha F_\beta F_\eta + \gamma_{\alpha\beta\eta\gamma} F_\alpha F_\beta F_\eta F_\gamma + ...$$

(4.2.3).

The energy, U, is now used to calculate the Boltzmann factor in the mean molecular

polarizability.

As was the case in Chapter Three, the change in the dipole moment caused by the

applied field is defined as the polarizability, Π. Based on Eq. (4.2.1), the polarizability is

$$\Pi_{\alpha\beta} = \frac{\partial \mu_\alpha}{\partial F_\beta} = \alpha_{\alpha\beta} + \beta_{\alpha\beta\eta} F_\eta + \gamma_{\alpha\beta\eta\gamma} F_\eta F_\gamma .$$

(4.2.4)

The tensors $\alpha_{\alpha\beta}$, $\beta_{\alpha\beta\eta}$, $\gamma_{\alpha\beta\eta\gamma}$ ... are referred to as the polarizabilities from this point on. Specifically, the term $\alpha_{\alpha\beta}$ is commonly referred to as the first order polarizability while the higher order terms are referred to as hyperpolarizabilities.

It is now convenient to introduce the direction cosine matrix elements, $k_\alpha^\parallel$ and $k_\alpha^\perp$, which are the projections of the space fixed axes parallel ($\parallel$) and perpendicular ($\perp$) to the electric field onto the molecular frame axis α. Equation (4.2.4), upon substitution, becomes

$$\Pi_{\alpha\beta} = \alpha_{\alpha\beta} + \beta_{\alpha\beta\eta}Fk_\eta^\parallel + \gamma_{\alpha\beta\eta\gamma}F^2 k_\eta^\parallel k_\gamma^\parallel + ... \qquad (4.2.5)$$

With the polarizability determined along the molecular axes, the laboratory polarizability is now computed, once again, through use of the direction cosine matrix elements. Because of the alignment of the polarizers with respect to the field in the Kerr setup, the polarizabilities along the axis parallel and perpendicular to the field will be of most interest. Equations (4.2.6) and (4.2.7) demonstrate the relationship between the polarizabilities generated through Eq. (4.2.5) and the polarizabilities for the space fixed axis system:

$$\Pi_{ZZ} = \Pi_{\alpha\beta} k_\alpha^\parallel k_\beta^\parallel, \qquad (4.2.6)$$

$$\Pi_{XX} = \Pi_{\alpha\beta} k_\alpha^\perp k_\beta^\perp. \qquad (4.2.7)$$

Considering only one molecule and the polarizabilities in Eqs. (4.2.6) and (4.2.7), the Kerr signal is

$$I_{det} = \frac{I_0}{2}(T_r + e^{-2\varepsilon_z''} + e^{-2\varepsilon_x''} - 2e^{-(\varepsilon_z'' + \varepsilon_x'')}\cos(\varepsilon_z' - \varepsilon_x')),$$ (4.2.8)

where

$$\varepsilon_z' - \varepsilon_x' = \omega\,\mathrm{Re}(\Pi_{ZZ} - \Pi_{XX})Y / \varepsilon_o c,$$ (4.2.9)

and

$$\varepsilon_{Z,X}'' = \omega\,\mathrm{Im}(\Pi_{ZZ,XX})Y / \varepsilon_o c.$$ (4.2.10).

The Kerr signal has now been calculated for one molecule. The next step is to consider an ensemble of molecules.

With both the polarizability and the energy calculated for a single molecule, the Boltzmann weighted average over all possible orientations of this molecule is now performed. Since the explosive molecules have a sufficiently dense manifold of rotational energy levels, the averaging will first be done classically by integration over all Euler angles. Equations (4.2.11)-(4.2.13) show the integrals that must be evaluated to calculate the mean molecular polarizabilities in the laboratory frame:

$$\overline{\Pi_{zz}} = \frac{\int_0^{2\pi} \int_0^{2\pi} \int_0^{\pi} \Pi_{\alpha\beta} k_\alpha^{\parallel} k_\beta^{\parallel} e^{-U/kT} \sin\theta \, d\theta d\varphi d\phi}{\int_0^{2\pi} \int_0^{2\pi} \int_0^{\pi} e^{-U/kT} \sin\theta \, d\theta d\varphi d\phi}, \qquad (4.2.11)$$

$$\overline{\Pi_{xx}} = \frac{\int_0^{2\pi} \int_0^{2\pi} \int_0^{\pi} \Pi_{\alpha\beta} k_\alpha^{\perp} k_\beta^{\perp} e^{-U/kT} \sin\theta \, d\theta d\varphi d\phi}{\int_0^{2\pi} \int_0^{2\pi} \int_0^{\pi} e^{-U/kT} \sin\theta \, d\theta d\varphi d\phi}, \qquad (4.2.12)$$

$$\overline{\Pi_{zz} - \Pi_{xx}} = \frac{\int_0^{2\pi} \int_0^{2\pi} \int_0^{\pi} \Pi_{\alpha\beta} (k_\alpha^{\parallel} k_\beta^{\parallel} - k_\alpha^{\perp} k_\beta^{\perp}) e^{-U/kT} \sin\theta \, d\theta d\varphi d\phi}{\int_0^{2\pi} \int_0^{2\pi} \int_0^{\pi} e^{-U/kT} \sin\theta \, d\theta d\varphi d\phi}. \qquad (4.2.13)$$

A Taylor Series expansion in the electric field is used to approximate these integrals. Since the polarizabilities $\overline{\Pi_{zz}}$ and $\overline{\Pi_{xx}}$ are equal in the absence of a field, the first term in the Taylor Series expansion of Eq. (4.2.13) that can lead to a Kerr signal term is the F term. To generate the second term, one needs the first derivatives of the mean molecular polarizabilities with respect to the field, which are given in Eqs. (4.2.14)-(4.2.16). In these expressions the brackets, $\langle \ \rangle$, are used to indicate integration over all space.

$$\frac{\partial \overline{\Pi}}{\partial F}_{F=0} = \left\langle \frac{\partial \Pi_{\alpha\beta}}{\partial F} \right\rangle_{F=0} - \frac{1}{kT} \left\langle \Pi \frac{\partial U}{\partial F} \right\rangle. \qquad (4.2.14)$$

$$\frac{\partial U}{\partial F}\bigg|_{F=0} = -\mu_\alpha k_\alpha^{\parallel}.$$ (4.2.15)

$$\frac{\partial \Pi_{\alpha\beta}}{\partial F}\bigg|_{F=0} = \beta_{\alpha\beta\eta} k_\eta^{\parallel}.$$ (4.2.16)

It can be easily shown that the integrations over all space for these derivatives are equal to zero for all three axes. For example, Eq. (4.2.17) gives the direction cosine for the molecular axis x projected onto the field axes. Inserting $k_x^{\parallel}$ in Eq. (4.2.11), it can be seen by inspection that the integral, Eq. (4.2.18), is equal to zero:

$$k_x^{\parallel} = \sin\varphi \, \sin\theta$$ (4.2.17)

$$\int_0^{2\pi}\int_0^{2\pi}\int_0^{\pi} \beta_{xxx} k_x^{\parallel} k_x^{\parallel} k_x^{\parallel} \sin\theta \; d\theta \; d\varphi \; d\phi = \int_0^{2\pi}\int_0^{2\pi}\int_0^{\pi} \beta_{xxx} \cos^3\varphi \, \sin^4\theta \; d\theta \; d\varphi \; d\phi = 0 .$$ (4.2.18)

Having demonstrated that the first two terms in the expansion contribute nothing to the Kerr signal, the third term is calculated from the second derivative of $\overline{\Pi}$ with respect to the field given in Eqs. (4.2.19)-(4.2.21).

$$\frac{\partial^2 \overline{\Pi}}{\partial F^2}\bigg|_{F=0} = \left\langle \frac{\partial^2 \Pi}{\partial F^2} \right\rangle - \frac{1}{kT}\left\langle 2\frac{\partial \Pi}{\partial F}\frac{\partial U}{\partial F} + \Pi\frac{\partial^2 U}{\partial F^2} \right\rangle + \frac{1}{k^2 T^2}\left\langle \Pi\left(\frac{\partial U}{\partial F}\right)^2 \right\rangle.$$ (4.2.19)

$$\frac{\partial^2 U}{\partial F^2}\bigg|_{F=0} = -\alpha_{\alpha\beta} k_\alpha^{\parallel} k_\beta^{\parallel} .$$ (4.2.20)

$$\frac{\partial^2 \Pi_{\alpha\beta}}{\partial F^2}\bigg|_{F=0} = \gamma_{\alpha\beta\eta\gamma} k_\eta^{\parallel} k_\gamma^{\parallel} .$$ (4.2.21)

Unlike the first two terms in the expansion, the second order terms are non-zero after integrating over all space. Instead of integrating all of the possible integrands, it is convenient to refer to the simple expression given by Buckingham for determining the values of the integrals associated with the hyperpolarizability, $\gamma_{\alpha\beta\eta\gamma}$.[1] The values of the integrals for the molecular polarizabilities given in Eqs. (4.2.11)-(4.2.13) are

$$\int_0^{2\pi}\int_0^{2\pi}\int_0^{\pi} k_\alpha^{\parallel} k_\beta^{\parallel} k_\eta^{\parallel} k_\gamma^{\parallel} \sin\theta \, d\theta \, d\varphi \, d\phi = \tfrac{1}{15}(\delta_{\alpha\beta}\delta_{\eta\gamma} + \delta_{\alpha\eta}\delta_{\beta\gamma} + \delta_{\alpha\gamma}\delta_{\beta\eta}),$$ (4.2.23)

and

$$\int_0^{2\pi}\int_0^{2\pi}\int_0^{\pi} k_\alpha^{\parallel} k_\beta^{\parallel} k_\eta^{\parallel} k_\gamma^{\parallel} \sin\theta \, d\theta \, d\varphi \, d\phi = \tfrac{1}{30}(4\delta_{\alpha\beta}\delta_{\eta\gamma} - \delta_{\alpha\eta}\delta_{\beta\gamma} - \delta_{\alpha\gamma}\delta_{\beta\eta}),$$ (4.2.24)

where $\delta_{\alpha\beta}$ is one when $\alpha = \beta$ and zero for $\alpha \neq \beta$. Making the substitutions for the values of the integrals in equation (4.2.13), the expression for the difference in the mean molecular polarizability is

$$\overline{\Pi_{zz} - \Pi_{xx}} = \frac{F^2}{30}\{(3\gamma_{\alpha\beta\alpha\beta} - \gamma_{\alpha\alpha\beta\beta}) + \frac{2}{kT}(3\beta_{\alpha\beta\alpha}\mu_\beta - \beta_{\alpha\alpha\beta}\mu_\beta)$$
$$+ \frac{1}{kT}(3\alpha_{\alpha\beta}\alpha_{\alpha\beta} - \alpha_{\alpha\alpha}\alpha_{\beta\beta}) + \frac{1}{k^2T^2}(3\alpha_{\alpha\beta}\mu_\alpha\mu_\beta - \alpha_{\alpha\alpha}\mu_\beta\mu_\beta)\}$$

(4.2.24).

The difference in mean molecular polarizabilities in Eq. (4.2.24) is, of course, responsible for the linear birefringence and dichroism in the sample. The first term in this expression does not depend on the temperature and arises from distortion of the polarizability in the field. The next two terms represent a combination of effects related to the distortion in the polarizability and the orientation of the molecule. The final term is solely dependent on the orientation of the molecule. Deriving the polarizabilites $\alpha_{\alpha\beta}$, $\beta_{\alpha\beta\eta}$, and $\gamma_{\alpha\beta\eta\gamma}$, is the final step in this derivation of the Kerr effect.

In Chapter Three, expressions were derived for the molecular polarizability from the time dependent perturbation approximation to the dipole moment in an oscillating field. Since the frequency of the transition will now be altered by the perturbing electric field, a Taylor series expansion for the perturbed polarizability near the transition frequency can be performed to approximate the polarizability as a function of frequency. The expansion yields terms in powers of the static electric field, which are the polarizabilities $\alpha_{\alpha\beta}$, $\beta_{\alpha\beta\eta}$, and $\gamma_{\alpha\beta\eta\gamma}$. Although it may not be immediately obvious, the results of the Taylor series expansion about the unperturbed transition frequency, ω_{jo}, are exactly equivalent to results of other treatments based on calculating the polarizability from the changes in energy of the states in the applied field. In the Taylor series approach,

however, the expressions for the polarizabilities come directly from the simple expressions for the polarizability of a perfectly aligned molecule derived in Chapter Three.

Recalling the expressions derived for the polarizability as a function of frequency in Chapter Three, expression (4.2.25) gives the polarizability for a molecule near a transition between states $\langle o |$ and $\langle j |$

$$\Pi_{\alpha\beta} = \frac{\omega_{jo}((\omega_{jo}^2 - \omega^2) + i\omega\Gamma)\langle o|\mu_\alpha|j\rangle\langle j|\mu_\beta|o\rangle}{\hbar((\omega_{jo}^2 - \omega^2)^2 + \omega^2\Gamma^2)}. \qquad (4.2.25)$$

The effect of the static electric field can be considered through its induced changes in the molecular eigenstates, the energies of the eigenstates, or a combination of the two. In the case of nitromethane, the unperturbed eigenstates are not substantially mixed by the 60 V/cm to 2 kV/cm fields used in this work. With the same approximation made for the general case considered here, the polarizability is calculated through a Taylor Series powers of the Stark frequency shift for transitions between states where the splitting is less than the linewidth, Γ_{jo}. Using the expression for the energy of a polar molecule in an electric field, the energy of a transition between $\langle o |$ and $\langle j |$ is given in Eq. (4.2.26)

$$\hbar\omega_{jo} = \hbar\omega_{jo} - (\mu_{j\alpha} - \mu_{o\alpha})F_\alpha - \tfrac{1}{2}(\alpha_{j\alpha\beta} - \alpha_{o\alpha\beta})F_\alpha F_\beta + ... \qquad (4.2.26)$$

After taking the derivatives of Eq. (4.2.25) with respect to the transition frequency, ω_{jo}, and multiplying them by the change in transition frequency, $\delta\omega_{jo}$, calculated from Eq. (4.2.26), the terms of the Taylor series expansion are separated into powers of the electric field. These terms are the polarizabilities $\alpha_{\alpha\beta}$, $\beta_{\alpha\beta\eta}$, and $\gamma_{\alpha\beta\eta\gamma}$. Equations (4.2.27)-(4.2.29) give the first three polarizabilities from the Taylor Series expansion:

$$\alpha_{\alpha\beta} = \left(\frac{2\omega_{jo}((\omega_{jo}{}^2 - \omega^2) + i\omega\Gamma)}{\hbar((\omega_{jo}{}^2 - \omega^2)^2 + \omega^2\Gamma^2)}\right)\langle o|\mu_\alpha|j\rangle\langle j|\mu_\beta|o\rangle, \qquad (4.2.28)$$

$$\beta_{\alpha\beta\eta} = \left(\frac{2((\omega_{jo}{}^2 - \omega^2)^2(-\omega_{jo}{}^2 - \omega^2) + \omega^2\Gamma^2(3\omega_{jo}{}^2 - \omega^2))}{\hbar^2((\omega_{jo}{}^2 - \omega^2)^2 + \omega^2\Gamma^2)^2}\right.$$

$$\left. + \frac{-2i\omega\Gamma((\omega_{jo}{}^2 - \omega^2)(3\omega_{jo}{}^2 + \omega^2) - \omega^2\Gamma^2)}{\hbar^2((\omega_{jo}{}^2 - \omega^2)^2 + \omega^2\Gamma^2)^2}\right)x$$

$$\langle o|\mu_\alpha|j\rangle\langle j|\mu_\beta|o\rangle(\mu_{j\eta} - \mu_{o\eta}), \qquad (4.2.29)$$

and

$$\gamma_{\alpha\beta\eta\gamma} = \left(\frac{2\omega_{jo}((\omega_{jo}{}^2 - \omega^2)^3(\omega_{jo}{}^2 + 3\omega^2) - 12\omega^2\Gamma^2\omega_{ho}{}^2(\omega_{jo}{}^2 - \omega^2) + 3\omega^4\Gamma^4)}{\hbar^3((\omega_{jo}{}^2 - \omega^2)^2 + \omega^2\Gamma^2)^3}\right.$$

$$\left. + \frac{2i\omega\Gamma\omega_{jo}(3(\omega_{jo}{}^2 - \omega^2)(\omega_{jo}{}^2 + \omega^2) - \omega^2\Gamma^2(5\omega_{jo}{}^2 - 3\omega^2))}{\hbar^3((\omega_{jo}{}^2 - \omega^2)^2 + \omega^2\Gamma^2)^3}\right)x$$

$$\langle o|\mu_\alpha|j\rangle\langle j|\mu_\beta|o\rangle(\mu_{j\eta} - \mu_{o\eta})(\mu_{j\gamma} - \mu_{o\gamma}). \qquad (4.2.30)$$

Substitution of these expressions for the polarizabilities into Eq. (4.2.24) and similiar expressions calculated for the polarizabilities parallel, $\overline{\Pi_{zz}}$, and perpendicular, $\overline{\Pi_{xx}}$, to the field, completes the derivation of the Kerr effect for an electronic or vibrational transition between states not significantly perturbed by the static field. From this point on, the frequency factor $X(\alpha_{\alpha\beta}, \omega_{jo})$ will be used to represent the frequency terms in the parentheses for the polarizability indicated in the first index. For example, $X(\alpha_{\alpha\beta}, \omega_{jo})$ is the parenthetical frequency factor in Eq. (4.2.28),

$$X(\alpha_{\alpha\beta}, \omega_{jo}) = \left(\frac{2\omega_{jo}((\omega_{jo}^2 - \omega^2) + i\omega\Gamma)}{\hbar((\omega_{jo}^2 - \omega^2)^2 + \omega^2\Gamma^2)} \right). \qquad (4.2.31)$$

It is now possible to compare the magnitudes of the contributions to the Kerr effect from the distortion of the polarizability and the orientation of the molecules induced by the field. For electronic and vibrational transitions of molecules in the gas phase at room temperature, if $\hbar^3(\Gamma)^3 << \hbar^2(\Gamma)^2 kT << \hbar\Gamma(kT)^2$, the Kerr effect for polar molecules is dominated by the distortion of the polarizability and the hyperpolarizability $\gamma_{\alpha\beta\eta\gamma}$ can be used to approximate the signal. In the next section the special case of the distortion that arises for rovibrational and rovibronic transitions is considered.

4.3   Rovibrational and Rovibronic Kerr Theory

Certainly, the classical expressions for the Kerr spectrum of a molecule cannot be used when the discrete rotational states of the molecule are considered. Instead of the integration over all possible orientations used in the classical approach to the problem, a summation over the discrete rotational states must be performed. The summation is done by replacing the states $\langle o|$ and $\langle j|$ in Eq. (4.2.26) with the symmetric top basis functions $\langle \tau, J, K, M|$ and $\langle \tau', J', K', M'|$, where τ and τ' are the ground and excited electronic or vibrational states. Equation (4.3.1) gives the expression for the molecular polarizability for a symmetric top molecule near a transition between $\langle \tau, J, K, M|$ and $\langle \tau', J', K', M'|$:

$$\Pi_{\alpha\beta} = \sum_{M,M'} X(\alpha_{\alpha\beta}, \omega_{jo}) \langle \tau, J, K, M | \mu_\alpha | \tau', J', K', M' \rangle \langle \tau', J', K', M' | \mu_\beta | \tau, J, K, M \rangle \quad (4.3.1)$$

Since consideration has only been given to the case when the resolution is not sufficient for observation of Stark splittings, the polarizability in Eq. (4.3.1) is summed over all M's in the ground and excited states. With the rotational wavefunction substitution made in the polarizability expression, the remainder of the derivation follows the classical treatment.

As in the classical treatment, it is essential to be able to correlate the molecular polarizability to the laboratory frame. The direction cosine matrix elements for the symmetric top can be expressed with the rotational quantum numbers J, K, and M. For

example, the projection of the dipole moment for a symmetric top molecule along the field axis is

$$\mu \cos \theta \, F = \frac{\mu MK}{J(J+1)}.$$
(4.3.2)

This projection of the dipole moment on the field axis determines the energy of a given orientation. Equation (4.3.3) gives the energy for a transition in the perturbed field for a molecule with a first order Stark effect,

$$\hbar \omega_{jo} = \hbar \omega_{jo}{}^{o} - \left(\frac{\mu_j M'K'}{J'(J'+1)} - \frac{\mu_o MK}{J(J+1)} \right) F.$$
(4.3.3)

The change in the transition frequency expressed in Eq. (4.3.3) is used in the Taylor Series expansion around ω_{jo} to calculate the polarizabilities.

Following the Buckingham derivation of the mean molecular polarizability, a Taylor Series expansion about $\omega_{\tau J'K'M'\tau JKM}$ enables the polarizabilities to be determined. Equations (4.2.29)-(4.2.30), which are the terms of this Taylor Series expansion, are used along with Eq. (4.3.1) and Eq. (4.3.3) to calculate the Kerr signal for a transition with resolved rotational structure. As was indicated in the discussion of the classical treatment of a vibrational or electronic transition, near a transition the hyperpolarizability $\gamma_{\alpha\beta\eta\gamma}$ dominates the other polarizabilities so that Eq. (4.2.30) can be used to approximate the

81

Kerr signal. Equation (4.3.4) expresses the polarizability difference responsible for the Kerr signal near a rovibrational or rovibronic transition of a molecule in the gas phase at room temperature.

$$\gamma_{zzzz} - \gamma_{zzxx} = \sum_{M,M'} X(\gamma_{\alpha\beta\eta\gamma'},\omega_{jo}) \left(\frac{\mu_j M'K'}{J'(J'+1)} - \frac{\mu_o MK}{J(J+1)} \right)^2 x$$

$$(\langle \tau',J',K',M|\mu_z|\tau,J,K,M\rangle^2 - \langle \tau',J',K',M\pm1|\mu_x|\tau,J,K,M\rangle). \quad (4.3.4)$$

For nitromethane and for other molecules in which the Stark splitting for the rovibrational transitions is greater than the linewidth, Γ_{jo}, the Taylor Series approximation to the frequency dependence is no longer appropriate. For these transitions in an electric field the polarization of the different ΔM transitions must be considered. The difference in polarizability along the axes parallel and perpendicular to the field is

$$\alpha_{zz} - \alpha_{xx} = X(\alpha_{\alpha\beta},\omega_{\tau JKM}^{\tau'J'K'M})\langle \tau\ J'K'M|\mu_z|\tau\ JKM\rangle - \quad (4.3.5)$$

$$X(\alpha_{\alpha\beta},\omega_{\tau JKM}^{\tau'J'K'M\pm1})\langle \tau\ J'K'M\pm1|\mu_x|\tau\ JKM\rangle.$$

The intensity of the line without the field is now spread over these different ΔM transitions and the difference between the dispersion and absorption for $\Delta M = 0$ and $\Delta M = \pm1$ gives the Kerr signal. In limit of very weak fields or the case of large J the Stark frequency split is small and Eq. (4.3.5) is small. In fact, if the frequencies $\omega_{zJKM}^{\tau'J'KM}$ and

ω_{zJKM}^{zJKM} are the same, Eq. (4.3.5) is easily shown to be zero. Therefore, the Kerr signal from the polarization of the ΔM is sensitive to low J lines, and the Kerr spectrum is expected to show fewer strong transitions.

References

[1] A.D. Buckingham, A.D. Pople, *Proc. Roy. Soc.* A68 (1955) 905.

[2] A.D. Buckingham, *Proc. Phys. Soc.* A267 (1962) 271.

[3] J.M. Brown, A.D. Buckingham, D. A. Ramsay, *Can. J. Phys.* 49 (1971) 914.

[4] M.P. Bogaard, B.J. Orr, *Magnetic Structure and Properties,* (ed. A.D. Buckingham) MTP International Review of Science, Physical Chemistry Ser. 2 Vol. 2 (1975) 149, Buttersworth, London.

Chapter Five

Nitromethane Kerr Spectrum Simulation

5.1 Introduction

To begin the study of nitromethane Kerr spectra, recorded for the asymmetric NO_2 stretch band at 1584 cm^{-1} shown in Fig. 5.1, assignment of some of the rotational structure in this band was made based on a calculation of the frequencies and intensities of some of the rovibration transitions. A description of this calculation along with the results are included in this chapter. The results of Chapter Four for the description of the Kerr effect are then applied to the rovibrational transitions. Kerr signals arising from Stark shifts larger than the homogeneous linewidth will be considered. The qualitative features of the Kerr spectra recorded for nitromethane emerge from this chapter.
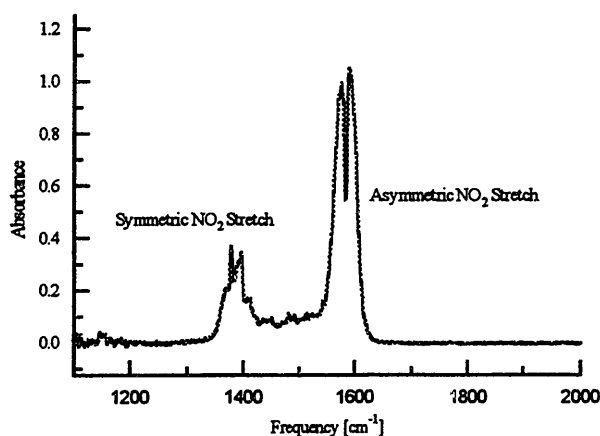
Figure 5.1 Nitromethane Infrared Absorption Spectrum The infrared vapor spectrum of nitromethane was collected with the BioRad FTS60A with 330 mTorr in the Kerr cell.

5.2 Rotational Structure Calculation

The rotational structure for the asymmetric NO_2 stretch band of nitromethane has been partially assigned by Pal, Hazra, Ghosh, and Kshirsagar for the ground internal rotor state.[3] Because a list of the assigned transitions was not available, the rotational structure of the band was calculated based on the Hamiltonian Pal et al. used to fit their spectrum. The rotational eigenstates and eigenvalues were also used in the calculation of the Kerr spectrum. Following the Pal et al. fit, the rotational structure of the B-type asymmetric stretch band of nitromethane was calculated using the Watson A reduction Hamilitonian in the I^r representation with internal free rotation. The rotation-internal rotation Hamiltonian for nitromethane is given in Eq. (5.2.1),

$$\tilde{H}_{rot} = BJ_x^2 + CJ_y^2 + AJ_z^2 - \Delta_J(\tilde{J}^2)^2 - \Delta_{JK}\tilde{J}^2 J_z^2 - \Delta_K J_z^4 - \tfrac{1}{2}[\delta_J \tilde{J}^2 + \delta_K J_z^2, J_+^2 + J_-^2]_+$$

$$+ Fp^2 - A'J_z p + \tfrac{1}{2}V_6(1 + \cos 6\alpha), \quad (5.2.1)$$

where J_z, $\tilde{J}^2$, and $J_+^2 + J_-^2$ are the normal symmetric top operators.[1] The operators J_x and J_y are $\tfrac{1}{2}(J_+ + J_-)$ and $\tfrac{i}{2}(J_+ - J_-)$, respectively. The second line of Eq. (5.2.1) accounts for the internal rotation. The constants A' and F are the frame rotational and internal rotation constant respectively. The potential term $\tfrac{1}{2}V_6(1 + \cos 6\alpha)$ is the potential for rotation expressed by the torsional angle, α, between the NO_2 plane and one of the

methyl hydrogens. The operator p is defined next in conjuction with calculation of the Hamiltonian matrix elements.

To generate the rotation-internal rotation Hamiltonian matrix, the symmetric top basis set wavefunctions, $|JK\rangle$'s, are replaced with the symmetric top wavefunctions times the internal rotation wavefunction $\exp(im\alpha)$ where m is an integer quantum number describing the internal rotation. The new state is represented by $|JKm\rangle$. In the symmetric top basis set with internal free rotation, the Hamiltonian diagonal matrix elements are

$$\langle JKm|\tilde{H}_{rot}|JKm\rangle = \tfrac{1}{2}(B+C)J(J+1) + (A' - \tfrac{1}{2}(B+C))K^2 - \Delta_J J^2(J+1)^2$$

$$- \Delta_{JK} J(J+1)K^2 - \Delta_K K^4 + Fm^2 - 2A'Km, \quad (5.2.5)$$

and the off-diagonal elements are

$$\langle JK\pm 2\,m|\tilde{H}_{rot}|JKm\rangle = \tfrac{1}{4}((B-C) - \delta_J J(J+1) - \delta_K K^2)\{[J(J+1)-K(K\pm 1)]x$$

$$[J(J+1)-(K\pm 1)(K\pm 2)]\}^{1/2}. \quad (5.2.6)$$

When $m=0$, the Hamiltonian matrix reduces to that of an asymmetric top. In this calculation, only the $m=0$ internal rotor state will be considered. Because the selection rule for internal rotation is $\Delta m = 0$, $m = 0$ is considered in the excited state as well.

After exclusion of internal rotation, the Hamiltonian matrix is simplified further with the introduction of the Wang transformed symmetric top basis set given in Eqs. (5.2.7) - (5.2.8).

$$\left| J\, 0^+ \right\rangle = \left| J\, 0 \right\rangle. \tag{5.2.7}$$

$$\left| J\, \mathrm{K}^+ \right\rangle = \tfrac{1}{\sqrt{2}}\left(\left| J\, -K \right\rangle + \left| J\,K \right\rangle \right). \tag{5.2.8}$$

$$\left| J\, \mathrm{K}^- \right\rangle = \tfrac{1}{\sqrt{2}}\left(\left| J\, -K \right\rangle - \left| J\,K \right\rangle \right), \tag{5.2.9}$$

where $\left| J\, \pm K \right\rangle$ are the symmetric top basis set state wavefunctions. With the transformation of the basis set and separation of even and odd K's indicated by Eq. (5.2.6), the diagonalization reduces to the diagonalization of four submatrices: even K $\left| J\, K^+ \right\rangle$, odd K $\left| J\, K^+ \right\rangle$, even K $\left| J\, K^- \right\rangle$, and odd K $\left| J\, K^- \right\rangle$.

Because Matlab, a numeric computation software package, includes pre-programmed diagonalization routines, it was selected for simulation of the rotational structure of the nitromethane band and for calculation of the Kerr spectrum.[2] Programs to generate the submatrices of the ground and excited state rotational Hamiltonian matrix in Matlab are given in Appendix B. The molecular constants for the calculation are given in Table 5.1. After diagonalization of the Hamiltonian matrix generated from the molecular constants and Eqs. (5.2.5) and (5.2.6), the eigenstates and eigenvalues were stored for

generation of the rovibrational spectrum and the Kerr spectrum. The energies of the rotational states were sorted and given indices K_a and K_c, the prolate and oblate symmetric top quantum numbers. The indices were assigned based on the energy of the states and were used solely for comparison with the spectrum in the literature.

The programs in Appendix B were written to generate the rovibrational spectrum of the asymmetric NO_2 stretch band of nitromethane. The intensities were calculated based on the transition moment operator applied to the rotational eigenstates expressed in the symmetric top basis set. The transition operator intensities were multiplied by the Boltzmann weighted population of the ground state at 300 K and the nuclear spin statistic weight which only allows population in even K for the ground internal rotor state. An absorption spectrum of nitromethane recorded in conjunction with the Kerr effect is used for evaluation of the calculated spectrum with the lines included in the Pal paper. Figure 5.2 shows a segment of the calculated rovibrational spectrum along with the recorded spectrum. Table 5.2 gives the calculated and observed frequencies for Fig. 5.2 along with additional lines assigned in the same spectral region by Pal. Pal reported a maximum discrepancy between the recorded and calculated spectra of 0.0045 cm^{-1} with a standard deviation of 0.0023 cm^{-1}. Over the spectral regions covered by this research, the same magnitude of discrepancies are observed between the calculated and recorded spectra; frequency calibrated to $\pm$ 0.002 cm^{-1}.

Table 5.1 Molecular parameters Molecular parameters reported in the literature for the 1584 cm^{-1} band of nitromethane for transitions between the ground internal rotor state.

Molecular Parameter	Lower State [cm^{-1}]	Upper State [cm^{-1}]
ν_0 [a]		1583.81163(20)
A' [b]	0.442999	
F [b]	5.5606235	
V_6 [c]	2.11	
A [a]	0.4450372	0.4449620(33)
B [a]	0.3517224	0.3516826(26)
C [a]	0.1959942	0.1960255(9)
$\Delta_J \times 10^6$ [a]	0.2048000	0.2431(23)
$\Delta_{JK} \times 10^6$ [a]	0.5921000	0.6822(103)
$\Delta_K \times 10^6$ [a]	-0.2515000	-1.5701(93)
$\delta_J \times 10^6$ [a]	0.0823000	0.0717(11)
$\delta_K \times 10^6$ [a]	0.5254000	0.4573(34)

[a] Chandramadhab Pal, Anindya Hazra, Pradip N. Ghosh, R.J. Kshirsagar, J. Mol. Struc. 165 (1997) 407.

[b] G.O. Sorensen, T. Pedersen, H. Dreizler, A. Guarnieri, A.P. Cox, J. Mol. Struc. 97 (1983) 77.

[c] E. Tannenbaum, R.J. Myers, W.D. Gwinn, J. Chem. Phys. 25 (1956) 42.
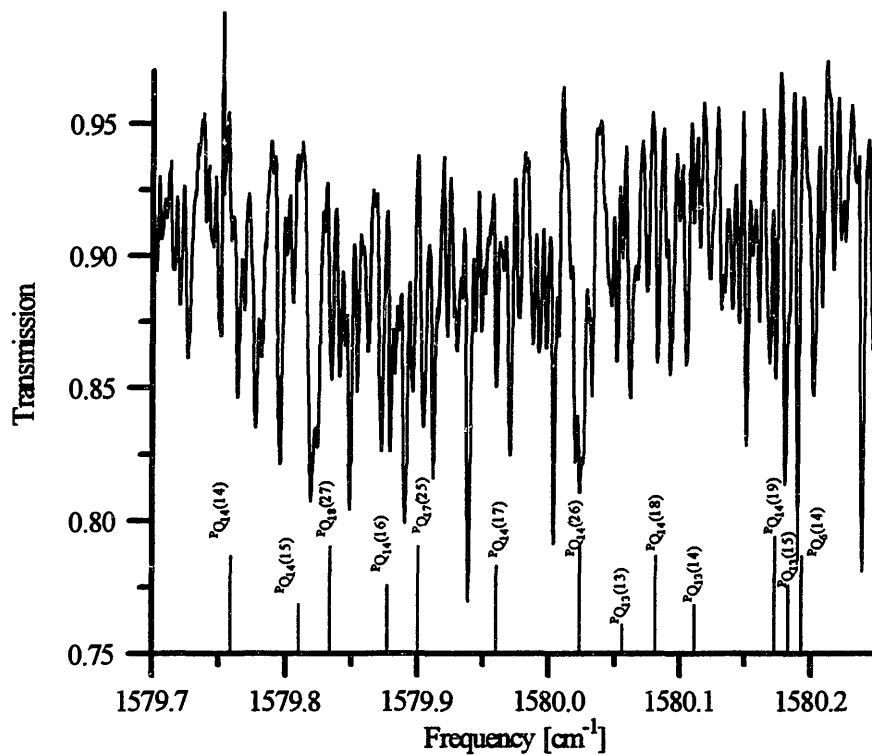
Figure 5.2 Calculated and Recorded Rotational Structure of B-Type Asymmetric Stretch Band of Nitromethane The figure illustrates the lines that were assigned by Pal along with the infrared absorption spectrum recorded in the Kerr cell with 100 mTorr of nitromethane in the cell. Over half of the lines are unassigned and belong to transitions between states with $m \neq 0$.

Table 5.2 Nitromethane Calculation Comparison

Assignment	Calculated [cm^{-1}]	Observed [cm^{-1}]	Assignment	Calculated [cm^{-1}]	Observed [cm^{-1}]
$^PP_5(5)$	1579.5028	1579.5014	$^PQ_{16}(28)$	1580.3882	1580.3881
$^PQ_{16}(21)$	1579.5670	1579.5670	$^PQ_{13}(24)$	1580.3928	1580.3950
$^PQ_{17}(24)$	1579.5908	1579.5936	$^PQ_{13}(17)$	1580.4190	1580.4156
$^PP_4(5)$	1579.6407	1579.6397	$^PQ_{12}(13)$	1580.4400	1580.4408
$^PP_2(9)$	1579.6925	1579.6936	$^PQ_{12}(14)$	1580.4868	1580.4843
$^PQ_{14}(14)$	1579.7564	1579.7588	$^PQ_{14}(20)$	1580.5318	1580.5313
$^PQ_{14}(15)$	1579.8096	1579.8088	$^PQ_5(12)$	1580.5546	1580.5534
$^PQ_{18}(27)$	1579.8336	1579.8338	$^PQ_{12}(15)$	1580.6043	1580.6038
$^PQ_{14}(16)$	1579.8771	1579.8781	$^PQ_{13}(18)$	1580.6440	1580.6411
$^RQ_{17}(25)$	1579.8999	1579.8960	$^PQ_{16}(28)$	1580.7291	1580.7309
$^PQ_{14}(17)$	1579.9596	1579.9594	$^PQ_{14}(25)$	1580.7361	1580.7352
$^PQ_{14}(26)$	1580.0229	1580.0228	$^PQ_{12}(22)$	1580.7592	1580.7593
$^PP_3(7)$	1580.0421	1580.0435	$^PQ_{12}(16)$	1580.7829	1580.7805
$^PQ_{13}(13)$	1580.0556	1580.0553	$^PQ_{16}(25)$	1580.8738	1580.8750
$^PQ_{14}(18)$	1580.0809	1580.0812	$^PQ_{14}(21)$	1580.9404	1580.9431
$^PQ_{13}(14)$	1580.1106	1580.1098	$^PQ_{13}(19)$	1580.9971	1580.9974
$^PQ_5(13)$	1580.1548	1580.1546	$^PQ_{12}(17)$	1581.0770	1581.0818
$^PQ_{14}(19)$	1580.1724	1580.1726	$^PQ_{16}(26)$	1581.2219	1581.2195
$^PQ_{13}(15)$	1580.1826	1580.1828	$^PP_2(5)$	1581.2288	1581.2250
$^PQ_6(14)$	1580.1925	1580.1958	$^PP_1(6)$	1581.2630	1581.2632
$^PQ_{13}(16)$	1580.2789	1580.2799	$^RP_4(6)$	1581.2707	1581.2696
$^PQ_{12}(12)$	1580.3365	1581.3584	$^PQ_{14}(24)$	1581.3177	1581.3166
$^PQ_{18}(28)$	1580.3382	1580.3406	$^PQ_{14}(22)$	1581.3606	1581.3607
$^RP_8(10)$	1580.3789	1580.3793	$^PQ_{13}(20)$	1581.4147	1581.4121

5.3 Nitromethane Kerr Spectroscopy

As was shown in Chapter Four, when the electric field is large and the Stark shifts for the transitions are larger than the transitions' linewidths, the polarization of the different ΔM transitions must be considered. For nitromethane, $\mu E = 5.8 \times 10^{-5} E$ cm^{-1}, the linear dichroism and birefringence results from the polarization of the different ΔM. Figure 5.3 illustrate the Stark splitting effect on the differential absorption and dispersion for the $^P P_4(4)$ transition of nitromethane with several applied fields. It should be noted from Fig. 5.3 that there is not a simple relationship between the electric field and the strength of the signal for a given line. However, as the field increases it seems apparent that some lines will overlap with other lines and the result will either be cancellation or enhancement of the signal. If the nearest line to the $^P P_4(4)$ is considered, the possibility of cancellation or enhancement of the signal from a single line is apparent. Figure 5.4 shows the overlap of the dispersion curves resulting from the Kerr effect. In the case of the asymmetric NO_2 stretch band of nitromethane, where the internal rotor increases the density of rotational states and transitions in the spectrum, the possibility of signal cancellation or enhancement from overlapping lines is more likely.
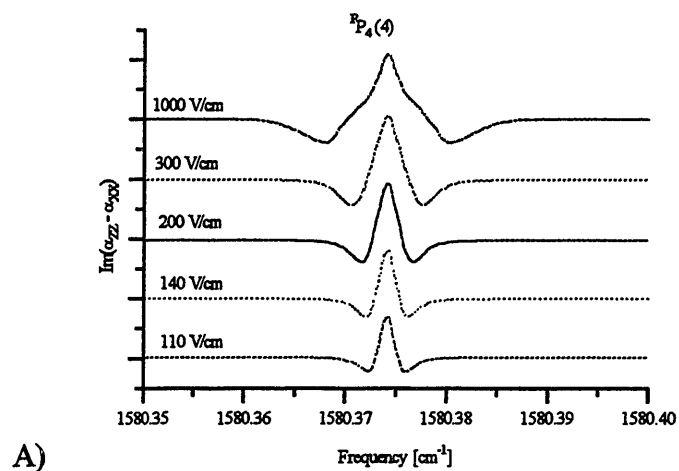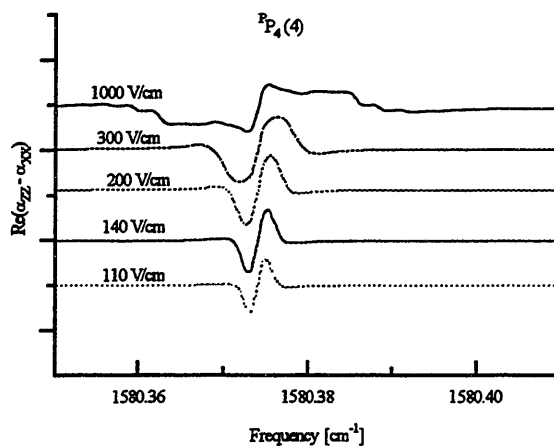
Figure 5.3 Calculated Differential Absorption and Dispersion for $^P P_4(4)$ Part A) of this figure illustrates the lineshape and effect of the field on the intensity of the differential absorption feature. Part B) demonstrates the differential dispersion. Both spectra result from the ΔM 's of the transition as they are shifted in frequency by the electric field.
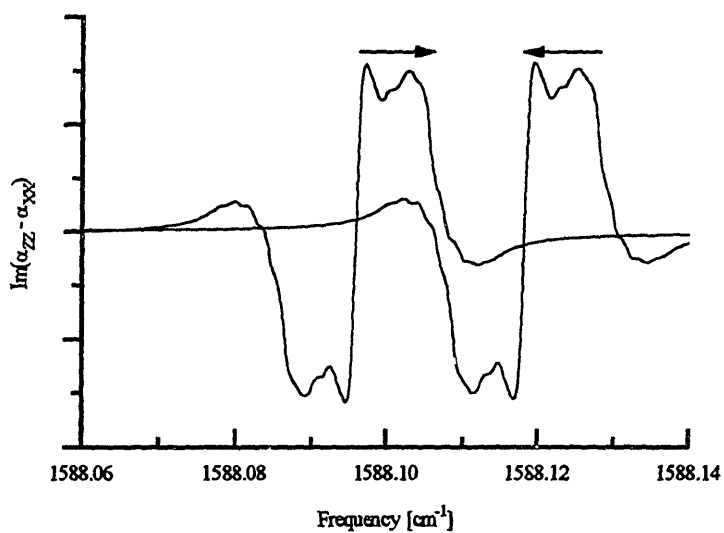
Figure 5.4 Signal Cancellation or Enhancement As the dispersion curves in this case are spread out there can be cancellation or enhancement of the Kerr signal from a nearby transition. The effect that neighboring lines have on each other makes assignment difficult at higher field strengths.

References

[1] J.K.G. Watson, *Vibrational Spectra and Structure* (J.R. Durig ed.), Vol. 6, Elsevier, Amsterdam, 1977.

[2] Matlab Version 4.3, Mathworks Inc., Cambridge, MA.

[3] C. Pal, A. Hazra, P.N. Ghosh, R.J. Kshirsagar, *J. Mol. Struc.* 165 (1997) 407.

[4] G.O. Sorensen, T. Pedersen, H. Dreizler, A. Guarnieri, A.P. Cox, *J. Mol. Struc.* 97 (1983) 77.

[5] E. Tannenbaum, R.J. Myers, W.D. Gwinn, *J. Chem. Phys.* 25 (1956) 42.

Chapter Six

Experimental Measurement of the Kerr Effect

6.1 Introduction

The Rev. John Kerr was able to measure the electric field induced birefringence for over 100 substances in just a few years of investigation. His success was achieved as a result of a detection apparatus that has survived to this day. In this chapter, the revisions to the classic Kerr measurement apparatus are described. The progress that has been made in Kerr effect measurements is used as a foundation for the development of the vibrational Kerr effect for explosives detection. In the course of describing the revisions to the classic Kerr measurement and dichroism measurement setups, motivations for the Kerr measurement systems pursued in this research are provided. The use of polarization modulation for enhancing sensitivity and selectivity to birefringence and linear dichroism emerges from Sections 6.2 and 6.3 as a successful modification to the classic Kerr setup. In Sections 6.4 to 6.8, a report on the attempted measurement schemes based on polarization modulation and the classic Kerr system applied to the detection of the vibrational Kerr effect is given. In the end, because of difficulties that are described in the sections on polarization modulation, this investigation of vibrational Kerr spectroscopy returned to the classic Kerr measurement apparatus.

6.2 Previous Work

Experimental setups specifically designed for measurement of the Kerr effect have primarily been designed for the visible region of the spectrum. The reported experimental setups differ only slightly from the simple system of a light source, two crossed polarizers, a narrow gap transverse Stark or Kerr cell, and a detector. For spectral information, a monochromator is often added. Figure 6.1 illustrates the arrangement of the elements in the classic Kerr measurement apparatus. Because the signal is proportional to the light source intensity, high power sources with low noise characteristics are usually chosen. Light sources which are well collimated are preferred as the light is directed between the narrow gap metal Stark plates which depolarize the light on reflection. At either end of the Kerr cell, the polarizers most commonly used are extinguishing polarizers such as Glan-Thompson prism polarizers, with transmission less than 10^{-6} when crossed. The extinguishing polarizers eliminate the perpendicular polarization and are preferred over polarizers based on angular separation of the polarization components. Kerr cells have been constructed for solids, liquids, and gases. In each design, conducting metal plates are used to apply the field to the sample. Kerr cells for the condensed phase have short path lengths (<2cm), while gas phase cells have been built with path lengths between one and two meters. Finally, high sensitivity detectors are chosen for the Kerr apparatus. The reported Kerr measurement systems differ only in one or two components from the system outlined here.

High Voltage
Power Supply

Kerr Cell

Signal Processing

High Power
Light Source

Polarizer

Ground

Analyzer
Polarizer
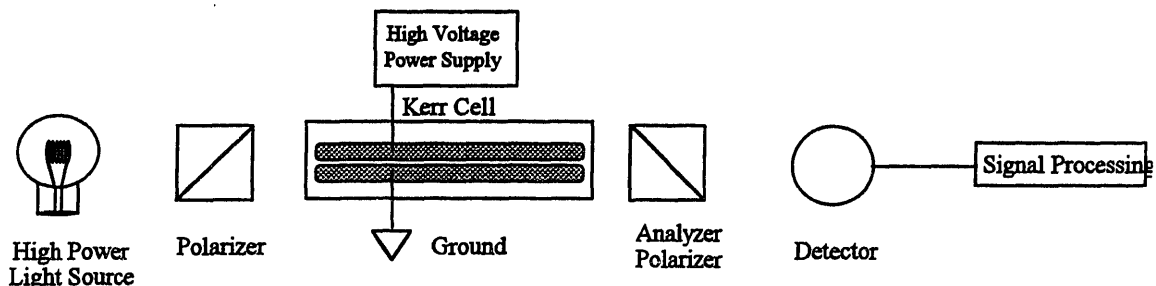
Detector

Figure 6.1 Classic Kerr Effect Apparatus. The classic Kerr measurement scheme is based on a high power light source, crossed polarizers, a Stark or Kerr cell, a detector, and signal processing electronics. When spectral information is recorded, a spectrometer is added to the setup. In the earlier experiments in this field, photographic plates were used as detectors.

Modifications and additions to the classic Kerr setup are made to diminish the problems of background birefringence and linear dichroism not associated with the analyte. In order to separate the desired Kerr effect from the background interferences, the electric field in the Stark cell is often modulated. With phase sensitive demodulation techniques, the demodulated signal on the detector is insensitive to the unmodulated background phenomena, and there can be an enhancement in the signal to noise. The extrinsic birefringence and linear dichroism interferences can also be eliminated by a birefringent compensator placed between the crossed polarizers. Because the Kerr effect is so well characterized for nitrobenzene and carbon disulfide, the compensator is often a liquid Kerr cell based on these compounds. The electric field in the cell is adjusted to minimize the background signal. The voltage applied to the compensator Kerr cell can

also be modulated. Not only do the modulated compensators eliminate the unwanted birefringence, but the modulation enables the separate recording of linear dichroism and birefringence spectra. The separation of these phenomena will be demonstrated in the next section on the photoelastic modulator.

With the unwanted background signals minimized, it is possible to measure the Kerr effect accurately. Before the magnitude of the effect can be accurately measured, the Kerr setup must be calibrated. For the reported visible wavelength measurements, the phenomenon most responsible for the transmission through the crossed polarizers is birefringence. Therefore, calibration of the visible systems was performed with well characterized birefringent materials For example, the liquid Kerr cell compensators mentioned above can be used for calibration. Additionally, Babinet-Soleil adjustable waveplates have been used to determine the response of the Kerr setup to a known birefringence. Once the response has been calibrated, it is important to characterize fully the Kerr cell. The Stark plate length and separation must also be accurately known. If great care is taken in calibration and in elimination of the background phenomena, sensitivity to Kerr dispersion angles of 10^{-9} radians ($(\varepsilon_Z' - \varepsilon_X')$, often called the dispersion angle) with absolute accuracy near 0.1 % has been reported for a few mW of visible light.[1,2]

As mentioned in the introduction, this research was directed at achievement of the same sensitivity and accuracy as Shelton's apparatus applied to the birefringence of H_2 at 632.8 nm, in the infrared near the symmetric and asymmetric NO_2 stretch bands of the explosives.[1,2] This research is the first reported measurement of the infrared Kerr effect in

the gas phase. In fact, only one Kerr measurement has been reported in the infrared. The Kerr spectrum of liquid nitrobenzene in the (2-5 μm region) covering its overtone bands has been reported.[3] Although only one other Kerr measurement has been reported in the infrared, many investigators have examined infrared optical activity. Infrared optical activity measurement systems have been developed for magnetic vibrational circular dichroism (MCVD) and vibrational circular dichroism (VCD) based on Fourier Transform spectrometers (FTS) coupled with polarization modulation.[4,5] Two approaches have been developed for the combination of FTS with polarization modulation. In the FTS combined with a photoelastic modulator design (FTS-PEM), shown in Fig. 6.2, the light from the interferometer is first polarized. Next, the polarization of this light is modulated with a photoelastic modulator. Unlike the classic Kerr measurement apparatus, there is no second analyzer polarizer in the FTS-PEM setup for optical activity. Instead, the light simply passes from the sample to the detector. The light on the detector is modulated between right and left circular polarization by the PEM. If the signal on the detector is demodulated, the signal is proportional to the difference in the sample absorption of the circular components. The demodulated signal is the interferogram corresponding to the differential absorption power spectrum of the sample.
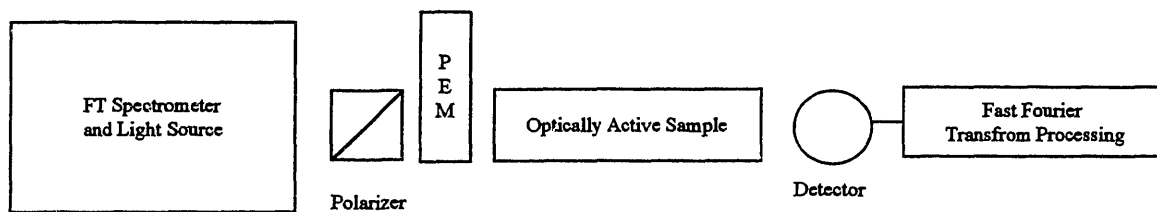
Figure 6.2 FT-PEM Infrared Optical Activity. Several investigators have built infrared optical activity measurement apparatuses based on amplitude modulation produced with a Michelson interferometer combined with polarization modulation produced with the PEM. The dual modulation scheme is reported to be sensitive to 10^{-6} differential circular absorbance.

In the FTS-PEM design, the amplitude and polarization modulations of the light are performed separately. The polarization and amplitude modulations, however, can be effected simultaneously with a polarization division interferometer (PDI). Figure 6.3 illustrates the construction of the PDI interferometer. In the PDI, the normal beamsplitter in the FT interferometer is replaced by a polarizing beamsplitter. This beamsplitter transmits one polarization which is reflected from the fixed mirror, while it reflects the orthogonal polarization which is reflected from the moving mirror. In order that the light in each of the arms of the interferometer can be retransmitted by the beamsplitter, the polarization of the light in each arm must be preserved. The polarization is preserved with the use of right angle mirrors. Because the interference, and thus the signal, at the beamsplitter is maximum when the intensity in both arms is balanced, the light source is polarized so that there are equal polarization components for the transmitted and reflected polarization axes of the beamsplitter. Upon recombination at the beamsplitter, the light is both amplitude modulated and polarization modulated as a function of the mirror distance.

The advantages of the PDI are twice the efficiency of the FTS-PEM measurement scheme and broader spectral coverage than is typical for a PEM.[6]
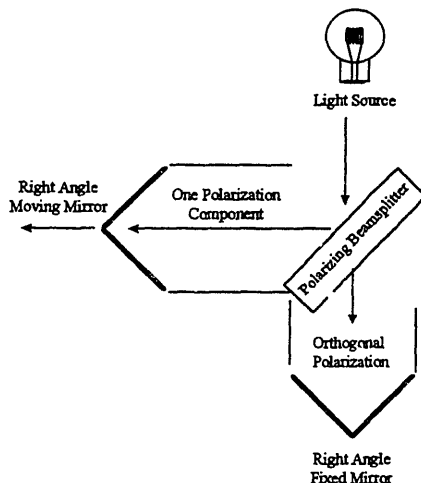
Figure 6.3   Polarization Division Interferometer In the PDI, the beamsplitter is replaced by a polarizing beamsplitter. The light source is polarized with equal components of the beamsplitter polarizations. Right angle mirrors are used instead of flat mirrors to preserve the polarization of the light. The light exiting the interferometer is both polarization and amplitude modulated as a function of mirror separation.

Although a dichroism sensitivity limit has not been reported for either the PDI or the FTS-PEM system, a review of the literature suggests that absorbance differences of 10^{-6} can be measured.[7-11] This circular dichroism absorbance difference corresponds to a Kerr transmission of 10^{-6}. This is three orders of magnitude less sensitive than the visible measurements already mentioned. One goal of this research was to improve on the FTS-PEM system sensitivity while characterizing the Kerr effect for explosives. For reasons explored later, no improvements were possible because the PEM used in these experiments continually malfunctioned.

6.3 Photoelastic Modulator

A key to this research on techniques for measurement of the Kerr effect has been the investigation of the application of the FTS-PEM system to the problems of linear dichroism and birefringence. The key element in an optical activity apparatus is the PEM. The addition of the PEM to the classic Kerr measurement apparatus permits separation of the linear dichroism and birefringence components of the Kerr signal. The PEM can also improve sensitivity to the Kerr effect. Both linear dichroism and linear birefringence of a Kerr measurement based on polarization modulation are explored through the derivation of the signal from the PEM based system.

The PEM is a polarization modulator based on the compression of a crystal. The crystal in the PEM is compressed along orthogonal axes, with the perpendicular modulations π (180°) out of phase with each other. The compression of the crystal makes the PEM birefringent so that as long as two axes of the PEM along which birefringence is modulated are not parallel to the initial polarization, the polarization of the light is modulated. Figure 6.4 illustrates the arrangement between the polarizers and the PEM in the PEM based Kerr measurement setup. The PEM is incorporated into the classic Kerr apparatus with the two compression axes of the PEM aligned at ±45 ° with respect to the first polarizer's polarization axis. As was shown in Chapter Three, this alignment of the PEM's birefringence results in the maximum modulation of the polarization.
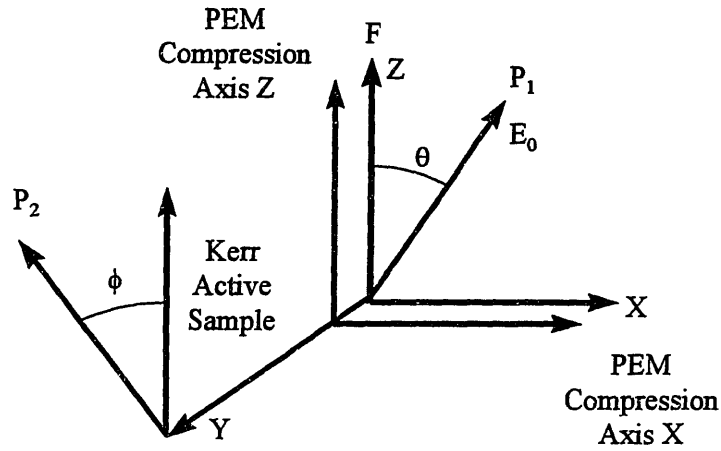
Figure 6.4 PEM Arrangement The PEM can be inserted anywhere between the crossed polarizers. The birefringent compression axes are aligned with the birefringent axes of the sample which are established by the field, F.

As in Chapter Three, the Jones Matrix convention is used to calculate the effect on the detected signal when the PEM is added to the classic Kerr apparatus. Returning to the Jones Matrix description of the classic Kerr apparatus given in Chapter Three, Eq. (6.3.1) gives the mathematical description of the electric field of the light at the detector, E_{det}, in the classic Kerr setup.

$$E_{det} = \begin{pmatrix} \cos\phi & \sin\phi \end{pmatrix} E_0 e^{i\omega t} \begin{pmatrix} e^{iD_z} & 0 \\ 0 & e^{iD_x} \end{pmatrix} \begin{pmatrix} \cos\theta \\ \sin\theta \end{pmatrix}$$

(6.3.1)

Recall that, the matrix elements $e^{iD_{z,x}}$ account for the intensity and phase changes that occur along the Z and X axes Once again, an arbitrary rotation of the polarization axes of

the polarizers by the angles θ and ϕ with respect to the static field axis will be considered first.

The PEM is included in Eq. (6.3.1) through a second matrix with the same form as the matrix describing the linear dichroism and birefringence of the sample. The result is

$$E_{det} = \begin{pmatrix} \cos\phi & \sin\phi \end{pmatrix} E_0 e^{i\alpha t} \begin{pmatrix} e^{iD_z} & 0 \\ 0 & e^{iD_x} \end{pmatrix} \begin{pmatrix} e^{iM} & 0 \\ 0 & e^{-iM} \end{pmatrix} \begin{pmatrix} \cos\theta \\ \sin\theta \end{pmatrix}. \qquad (6.3.2)$$

The ordering of the matrices in Eq. (6.3.2) reflects the optical order of the elements. The exponential term M in the PEM matrix is the refractive index modulation determined by the compression of the crystal. The compression of the crystal is sinusoidal as indicated by Eq. (6.3.3) where M_0 is the modulation depth or retardation set by the PEM controller.

$$M = \frac{M_0}{2}\cos(ft) \qquad (6.3.3)$$

The frequency, f, of the modulation was 30 kHz for the IR ZnSe PEM tested and 50 kHz for the quartz PEM (PEM90 controller, Model II ZS37, Model FS50). For the Hinds PEM's tested in this investigation, the modulation depth M_0 was set by the PEM controller. On the PEM controller, the modulated birefringence was selected with the same parameters that would be used to specify a waveplate. Therefore, the wavelength for the modulation was specified in addition to the modulation depth. For example, with a

modulation depth of quarter-wave at a wavelength setting of 632.8 nm, the PEM would be a modulated quarter-waveplate for 632.8 nm light. The same setting would be a 1/8 waveplate at 1265.6 nm, and a half waveplate for 316.4 nm.

Following the calculations made in Chapter Three, the intensity at the detector is

$$I = I_0 (\cos^2 \theta \cos^2 \phi e^{-2\varepsilon_z''} \cos^2 (2M + 2\varepsilon_z' - 2\omega t)$$

$$+ \sin^2 \theta \sin^2 \phi e^{-2\varepsilon_x''} \cos^2 (-2M - 2\varepsilon_x' - 2\omega t)$$

$$+ 1/2 \sin 2\theta \sin 2\phi e^{-(\varepsilon_z'' + \varepsilon_x'')} \cos(M + \varepsilon_z' - \omega t) \cos(-M + \varepsilon_x' - \omega t)), \qquad (6.3.4)$$

where I_0 is the light source intensity, $\varepsilon_{z,x}''$ are the absorption coefficients along the axes Z and X, and $\varepsilon_{z,x}'$ are the phases of the light along the two axes. The detector cannot respond at the optical frequencies, so once again an average over time is calculated making the slowly varying wave approximation for the polarization modulation. This is a good approximation for the 50 kHz and 30 kHz modulation frequencies considered here. With this approximation, the signal for a given wavelength is

$$I_{det} = \frac{I_0}{2} (\cos^2 \theta \cos^2 \phi e^{-2\varepsilon_z''} + \sin^2 \theta \sin^2 \phi e^{-2\varepsilon_x''}$$

$$+ 1/2 \sin 2\theta \sin 2\phi \cos(\varepsilon_z' - \varepsilon_x' - 2M) e^{-(\varepsilon_z'' + \varepsilon_x'')}). \qquad (6.3.5)$$

In order to measure the birefringence of the sample, the modulation birefringence and the sample birefringence must be separated. A trigonometric identity for the final term is used to separate the modulation and sample birefringences. Equation (6.3.6) shows the separation between these phenomena.

$$I_{det} = \frac{I_0}{2}(cos^2 \theta \, cos^2 \phi e^{-2\varepsilon_z''} + sin^2 \theta \, sin^2 \phi e^{-2\varepsilon_x''}$$

$$+ 1/2 \sin 2\theta \sin 2\phi (\cos(\varepsilon_z' - \varepsilon_x') \cos(2M) + \sin(\varepsilon_z' - \varepsilon_x') \sin(2M)) e^{-(\varepsilon_z'' + \varepsilon_x'')}) . \quad (6.3.6)$$

The first two terms in the first line of Eq. (6.3.5) describe the dichroism, while the second line accounts for the birefringence. The $\cos(M_0 \cos ft)$ and $\sin(M_0 \cos ft)$ in Eq. (6.3.6) can be expanded via a Fourier expansion. Equations (6.3.7) and (6.3.8) give the Fourier expansion for these terms, where $J_n(M_0)$ are the ordinary Bessel functions.

$$\cos(M_0 \cos ft) = J_0(M_0) + 2\sum_n^{\infty} (-1)^n J_{2n}(M_0) \cos(2nft) . \quad (6.3.7)$$

$$\sin(M_0 \cos ft) = 2\sum_n^{\infty} (-1)^{n+1} J_{2n-1}(M_0) \cos((2n-1)ft) . \quad (6.3.8)$$

Making the substitution for $\cos(M_0 \cos ft)$ and $\sin(M_0 \cos ft)$, and orienting the polarizers at $\pm 45°$ with respect to the PEM axes, and the field axes Z and X, Eq. (6.3.9) gives the intensity of light on the detector for non-ideal polarizers with transmission T_r.

$$I_{det} = \frac{I_0}{4}(T_r + e^{-2\varepsilon_z''} + e^{-2\varepsilon_x''} - 2e^{-(\varepsilon_z''+\varepsilon_x'')}\left[\cos(\varepsilon_z' - \varepsilon_x')[J_0(M_0) + 2\sum_n^\infty (-1)^n J_{2n}(M_0)\cos(2nft)]\right.$$

$$\left. + 2\sin(\varepsilon_z' - \varepsilon_x')\sum_n^\infty (-1)^{n+1} J_{2n-1}(M_0)\cos((2n-1)ft)\right]. \qquad (6.3.9)$$

With the signal on the detector calculated, it is now possible to explore the potential of PEM in detection of the Kerr effect. First it can be shown from Eq. (6.3.9) that with demodulation of the signal at odd harmonics of the modulation frequency, f, the demodulated signal is proportional to $\sin(\varepsilon_z' - \varepsilon_x')$, which is zero when there is no birefringence. The birefringence can also be detected at even harmonics but the signal is proportional to $\cos(\varepsilon_z' - \varepsilon_x')$ and for small differences in indices of refraction detection is made against a large background. The only absorption in the modulation expression is the total absorption, $\varepsilon_z'' + \varepsilon_x''$, so the effects of linear dichroism has been removed from the birefringence signal.

Two mechanisms for signal to noise enhancement are indicated by Eq. (6.3.9). The signal to noise can be enhanced through lock-in detection if the time constant and modulation frequency are properly chosen. By looking at the case of pure birefringence, a signal to noise enhancement mechanism is noted for the phase-sensitive detection

enhancement. In the case of pure birefringence in the classic Kerr apparatus, the intensity at the detector reduces to

$$I_{det} = \frac{I_0}{2}\sin^2((\varepsilon_z' - \varepsilon_x')/2).$$

(6.3.10)

Through use of the PEM, the signal for pure birefringence is proportional to the square root of the classic Kerr signal, where $\sin(\varepsilon_z' - \varepsilon_x') >> \sin^2((\varepsilon_z' - \varepsilon_x')/2)$. With the use of another polarization modulation technique, the same enhancement mechanism was used to detect a shot noise limited Kerr dispersion angle of 10^{-9} radians.[1,2]

If light source noise is a significant problem, Eq. (6.3.11) indicates that for pure birefringence an unmodulated, DC signal can be generated independent of the birefringence. The birefringence independent DC signal is possible when the $J_0(M_0)$ is zero. This Bessel function is zero when the modulation depth is set to 0.383 wavelengths, which means $M_0 = 2.406$ radians. The DC signal, independent of birefringence has been used in a ratio scheme to normalize the light source intensity fluctuations.

Just as the birefringence can be separated from the dichroism, the PEM can also be used to measure independently the linear dichroism of the sample. The Kerr apparatus is modified in two ways for the dichroism measurements. First, the analyzer polarizer is removed. Next, the sample is rotated so that the field axis is parallel with the first polarizer's polarization axis. Figure 6.5 shows the arrangement of the PEM, polarizer and

sample for the linear dichroism measurements. Without the dichroic sample the

polarization of the light is described by Eq. (6.3.11)

$$E_{det} = E_0 e^{i\omega t} \begin{pmatrix} e^{iM} & 0 \\ 0 & e^{-iM} \end{pmatrix} \begin{pmatrix} \cos\theta \\ \sin\theta \end{pmatrix}$$

(6.3.11)
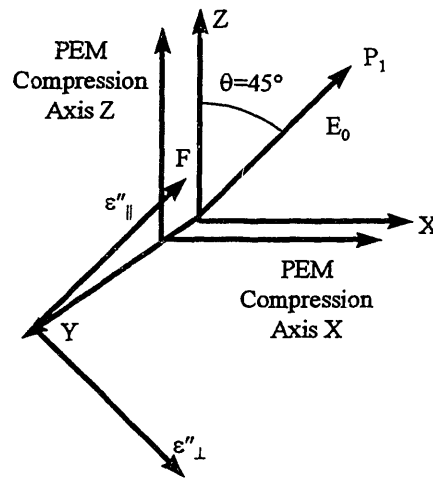
Figure 6.5 Linear Dichroism Arrangement For linear dichroism measurements, the sample and field are rotated 45° so that the dichroic axes are parallel and perpendicular with the first polarizer's axes. The analyzer polarizer is removed.

Although the sample is rotated in the dichroism measurements, Eq. (6.3.11) reflects no

change in the axis system in which the Jones Matrices are defined. The projections of the

polarization of the light along the dichroic axes parallel and perpendicular to the initial

polarization are taken based on Eq. (6.3.11). The electric field projections along the

dichroic axes are then multiplied by the exponentials for the respective absorbances. The light field parallel to the polarizer is

$$E_{det}^{\parallel} = e^{-\varepsilon_{\parallel}''}\left(\tfrac{1}{\sqrt{2}}\ \ \tfrac{1}{\sqrt{2}}\right)E_0 e^{i\alpha t}\begin{pmatrix} e^{iM} & 0 \\ 0 & e^{-iM} \end{pmatrix}\begin{pmatrix} \cos\theta \\ \sin\theta \end{pmatrix}, \qquad (6.3.12)$$

while the light field perpendicular to the first polarizer is

$$E_{det}^{\perp} = e^{-\varepsilon_{\perp}''}\left(\tfrac{1}{\sqrt{2}}\ \ -\tfrac{1}{\sqrt{2}}\right)E_0 e^{i\alpha t}\begin{pmatrix} e^{iM} & 0 \\ 0 & e^{-iM} \end{pmatrix}\begin{pmatrix} \cos\theta \\ \sin\theta \end{pmatrix}. \qquad (6.3.13)$$

The intensity, Eq. (6.3.14), of the light at the detector is the sum of the intensities parallel and perpendicular to the first polarizer.

$$I_{det} = \varepsilon_0 c\left[(E_{det}^{\parallel})^2 + (E_{det}^{\perp})^2\right]. \qquad (6.3.14)$$

After averaging over the time response of the detector and making substitution for $\cos(M_0 \cos ft)$ in the same way as for the birefringence case, Eq. (6.3.15) gives the intensity of light at the detector.

$$I_{det} = \frac{I_0}{2}\left[e^{-2\varepsilon_\parallel''} + e^{-2\varepsilon_\perp''} + (e^{-2\varepsilon_\parallel''} - e^{-2\varepsilon_\perp''})[J_0(M_0) + 2\sum_{n}^{\infty}(-1)^n J_{2n}(M_0)\cos(2n\!f\!t)] \right].$$

(6.3.15)

Equation (6.3.15) indicates that the intensity on the detector is the sum of a modulated (I_{AC}) and unmodulated (I_{DC}) signal. If the modulated signal is extracted with a lock-in amplifier while the unmodulated signal is separated with a low pass filter, the ratio of the I_{AC}/I_{DC} signals is determined by the difference in absorbance $\varepsilon_\parallel'' - \varepsilon_\perp''$. Equation (6.3.16) indicates that the ratio I_{AC}/I_{DC} is proportional to the hyperbolic tangent of the absorbance difference.

$$\frac{I_{AC}}{I_{DC}} = 2J_2(M_0)\tanh(\varepsilon_\parallel'' - \varepsilon_\perp'').$$

(6.3.16)

The utility of the PEM in characterization of the Kerr effects has been demonstrated through the derivation of the signals for linear dichroism and birefringence. The capacity to separate these two phenomena is of particular interest in modeling the effect. It was also shown that the PEM can be used to increase the signal to noise ratio over the classic Kerr measurement apparatus. A combination of the success of the FT-PEM optical activity measurements and the potential of the PEM were the reason for pursuing a PEM based Kerr measurement apparatus.

6.4 FT Polarization Modulation Spectroscopy: Introduction

As was shown in the previous section, there were a number of reasons for pursuing the PEM based Kerr measurement scheme. The Fourier Transform spectrometer was selected to take advantage of the multiplex and throughput advantages over dispersive spectrometers. In addition, the BioRad FTS60A is functional in the ultraviolet, visible, and infrared.

Two attempts at the FT-PEM Kerr measurement were made. In the first, the FTS-PEM apparatus was designed to repeat the measurements of the formaldehyde Kerr effect for the $\widetilde{A}^1 A_2 - \widetilde{X}^1 A_1 (\pi^* \leftarrow n)$ ultraviolet transition of formaldehyde previously reported.[12-14] The goal of the formaldehyde experiments was to demonstrate the technique on a molecule that had already been investigated. The final attempt was made with the FTS-PEM apparatus operated in the infrared near the NO_2 bands of the explosives. The components of the measurement apparatus common to all measurements will be described in the first part of this section. Then the specifics of the ultraviolet, near IR, and mid-IR FT-PEM measurement apparatus will be explored in subsequent sections.

The measurement of the Kerr effect began with the construction of the Kerr cell shown in Fig. 6.6. Great care was taken in the design to minimize electrical discharges from the Stark plates. For this reason, the cell was constructed of two inch inside diameter glass tubing, that was four feet in length. Two stopcocks were attached to the cell for sample introduction and connection to a mechanical pump. Two additional ports were added to supply the high voltage to the plates and for a Baratron pressure transducer

for pressure measurements. All attachments to the cell ports were made with 9 mm Viton O-ring glass fasteners. The windows were 2 inch diameter CaF_2 1 cm thick wedged flats (Janos) and were mounted to the cell with an aluminum flange shown in Fig. 6.7. On the window side of the flange the window was compressed against a Green Rubber 1-130 Viton O-ring placed in an O-ring groove. The window was held in place by an aluminum sleeve attached to the aluminum flange with #4-40 screws. On the other side of the flange, and Green Rubber 1-139 O-ring was used to seal to the cell.
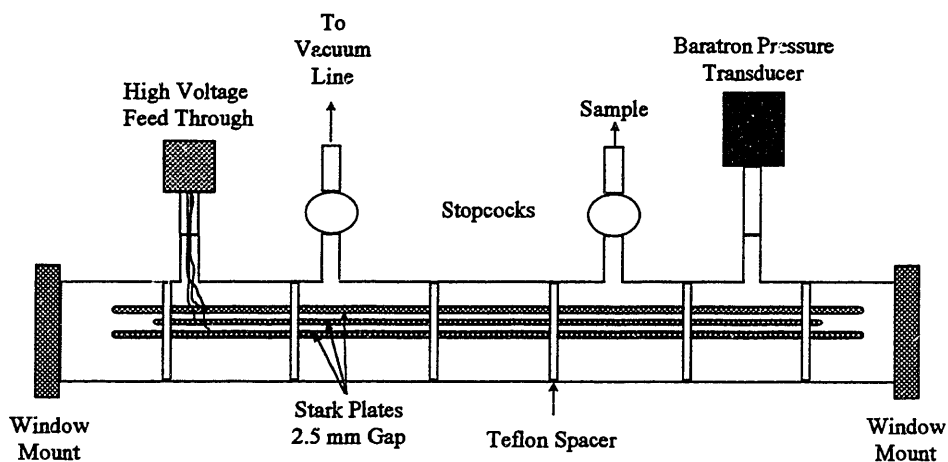
Figure 6.6 Kerr Cell The Kerr cell is constructed from a four foot long section of two inch diameter glass tubing. The Stark plates were separated 2.5 mm by six teflon spacers evenly spaced in the cell. The three plate design was selected for minimizing discharges at low pressure. The window mounts are shown in Fig. 6.7. Connections to the cell were made with 9 mm Viton O-ring connectors.

Aluminum
Window
Mount

CaF₂
Wedged
Window

1-130 Viton
O-ring

Aluminum Flange

1-139 Viton
O-ring

#4-40
Screws

2 in

O-ring
Groove

3/8 in
Bolt
Mounting
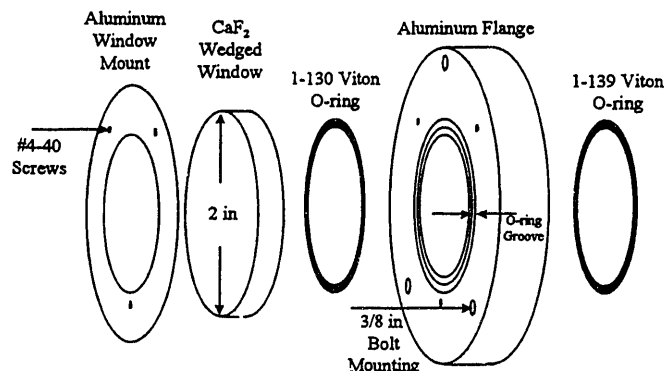
Figure 6.7 Window Mounts The windows were mounted to the cell with an aluminum flange. The seal between the window and the flange, and between the flange and the cell were made with Green Rubber Viton O-rings. The vacuum seal was difficult to maintain at higher temperatures as the flange and glass cell had different thermal expansion coefficients.

Inside the cell, a three plate design was used to produce the static electric field. The inside plate was smaller than the outside plates and was negatively biased, while the outside plates were grounded. The small plate placed between the larger outside plates minimized electrical discharges from the edges of the biased middle plate to the other plates, and exterior of the cell. The plates were constructed of 3/16 of an inch thick polished stainless steel with the edges rounded. The outside plates were 44 inches long with a width of 1 ½ inches, while the inside plate was 43 inches long with a width of 1 ¼ inch. The plates were held in the cell by six teflon spacers which separated the two outside plates and the inside plate with gaps of 2.5 mm. The gap was kept constant to within 0.1 mm along the length of the plates with teflon wedges placed between the plates. In experiments where optical throughput needed to be maximized the center plate was removed to yield a gap of 9.8 mm. Voltage was supplied to the plates with a Fluke 4088

power supply which was calibrated to within ± 10 V. The ground and voltage wiring were attached to the plates through 2-56 screws in the side of the plates. High vacuum Teflon wire was used to minimize out-gasing. The high voltage connection screws were encased in teflon holders to prevent discharges from the edges of the screws.

6.5 Formaldehyde Ultraviolet Kerr Effect: Procedures and Setup

Figure 6.8 illustrates the arrangements of the basic components of the FT-PEM Kerr measurement apparatus. In the formaldehyde experiments the light source was a 1000W Oriel Xenon arc lamp. The light output was collimated with the telescope mounted to the housing of the lamp. An Oriel infrared absorption cell was attached to the telescope to minimize damage to the optics in the interferometer from the IR output of the arc lamp. The light from the arc lamp was directed into the interferometer through the external source port of the BioRad FTS60A. The beamsplitter in the interferometer was the BioRad Quartz UV beamsplitter. At the external sample port, a two lens telescope constructed of 50 cm and 25 cm focal length lenses (Janos CaF_2) was used to improve collimation and reduce the beam size to fit within the one inch aperture size of the Kerr cell. An aperture at the focal length of the two lenses of the telescope was added to eliminate non-collimated light. The light from the telescope was then directed through the first polarizer (1 cm aperture) and the cell with two, two inch mirrors (Janos Al coated flats) mounted for horizontal and vertical control of the beam. The polarizers were calcite Glan-Thompson prism polarizers with crossed transmission of 10^{-6}. The light was directed

through only one of the gaps between middle and outside Stark plates. After the analyzer

polarizer, the detectors used were a Hamamatsu R166UH photomultiplier (Sensitivity = 4

x 10^5 A/W, Dark Current = 1 nA), Hamamatsu 1P28 photomultiplier (Sensitivity = 4.8

x10^5 A/W, Dark Current = 1 nA), and a UDT UV-enhanced photodiode (455UV/LN,

NEP = 2.5 x 10^{-14}). For the 1P28 and the photodiode, an Andover fused silica UV filter

(FS326) with maximum transmission at 326 nm (70%) with a FWHM of 23 nm was used

to shield the detector from room light. A one inch diameter f/1 CaF_2 lens (Janos) was

used to focus the light onto the photodiode or to fill the cathode of the PMT.

FT Spectrometer and Light Source — Polarizer — P E M — High Voltage Power Supply — Kerr Cell — Ground — Analyzer Polarizer — Detector — Lock-in Amplifier Locked to PEM — Fast Fourier Transfrom Processing
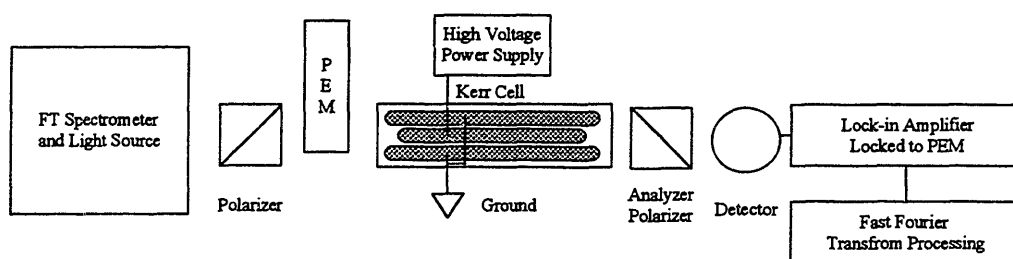
Figure 6.8 FT-PEM Setup For all attempts at the Kerr measurement, the light from the interferometer was directed through a polarizer followed by the PEM. The light was directed between one of the gaps between the middle and outside plates. After lock-in detection at the PEM frequency, the signal was processed with the BioRad fast Fourier Transform software.

The signal from the detectors was demodulated with Princeton Applied Research

(PAR) model 124A lock-in with a PAR 116 preamplifier input. The PAR 124A was

chosen over other lock-ins because the 124A could be used just as a mixer without an

output time constant. At the faster Fourier frequencies used in the formaldehyde

experiments, this insured that the lock-in did not distort the Fourier frequencies in the

interferogram signal. The sensitivity of the lock-in was selected so that the lock-in output signal filled the BioRad A/D converter (± 10 V). The BioRad signal processing was used after the lock-in to collect the interferogram and to convert the interferogram to a power spectrum.

The formaldehyde was cracked from para-formaldehyde (Aldrich). The synthesized formaldehyde was triply distilled from a dry ice-acetone cooled cold finger (196 K) to a liquid nitrogen chilled finger (77 K). Five grams were prepared at a time. The formaldehyde was stored in a dry ice and acetone bath. Without the cold storage, the polymerization of the formaldehyde, a highly exothermic reaction, would destroy the glass storage vessels used.

Attempts at Kerr spectra were collected at vapor pressures between one and eight Torr. Field strengths between 1 kV/cm and 10 kV/cm were applied to the formaldehyde samples for the Kerr measurements. Above an applied field of 2.5 kV/cm, the cell was filled with 200-400 Torr of SF_6 to prevent electrical discharges. For a field of 12 kV/cm and a formaldehyde pressure of 5 Torr, Bridge, Haner, and Dows were able to see 1.5% transmission through their 1 m pathlength Kerr cell in the classic Kerr apparatus for some of the rotational lines for this band of formaldehyde.[14]

6.6 Formaldehyde Ultraviolet Kerr Effect: Results

Although absorption spectra of formaldehyde could be recorded in the ultraviolet, the interferometer lacked the stability necessary for the measurement of the Kerr

spectrum. The stability problem of the interferometer while operating in the ultraviolet was experimentally verified during the frequency calibration of an Acousto-optic Tunable Filter (AOTF) around 300 nm. In that calibration, the BioRad FTS60A was used to measure the 30-40 cm^{-1} optical bandpass of the AOTF. It was noted during a series of single beam collections that the AOTF bandpass feature in the power spectrum would disappear while the interferogram was still detected on the PMT. The disappearance of the single beam power spectrum is most likely the result of the instability of the interferometer. As was noted in Chapter Two, the interferometer is automatically aligned so that the moving mirror and fixed mirror are always coplanar. One of the most difficult problems with the BioRad FTS60A interferometer is the instability of the automated dynamic alignment. For the long infrared wavelengths, the instability is not as significant as it is for the shorter ultraviolet wavelengths. To illustrate, if from one scan to the next the mirrors are shifted by one quarter of the HeNe alignment laser wavelength, the interferometer will be misaligned by nearly half of a wavelength for the ultraviolet wavelengths near the formaldehyde band. For the misaligned HeNe interferograms, the average of successive interferograms will exhibit only partial cancellation while the average for the ultraviolet interferograms may be completely canceled.

The error in the mirror positions is exacerbated by the way the zero path difference of the interferometer is determined. The zero path difference is the position of the moving mirror where the moving and stationary mirrors are equidistant from the beamsplitter,. The zero path difference is determined to be the largest negative peak in the interferogram by the FTS60A control electronics. Appropriate determination of the zero path difference

is important because the software of the BioRad performs the fast Fourier transform (FFT) from this point. If between scans the zero point is shifted slightly due to misalignment of the mirrors, the shift can lead to errors in the FFT and cancellation of the signal. In the AOTF calibration scans, the problem led to a software error that indicated there was no distinguishable zero path difference and to the already mentioned disappearance of the bandpass feature of the AOTF in the power spectrum. The problem is less pronounced for scans when there is a broad spectral source such as the Xenon arc lamp. However, even for the broad band Mercury arc lamp source, which has more structure than the Xenon arc, there were problems with the disappearance of Mercury spectral features. In the end, the BioRad FTS60A is more stable for single frequency narrow features on a broad power spectrum than for similar features against a zero background.

Two approaches were taken to remedy the problem of interferometer instability. The first was based on the correction proposed by Keiderling for his BioRad FTS60A interferometer where he experienced a similar problem of zero path difference determination in VCD.[15] In Keiderling's VCD experiments, the zero path difference problem was remedied by the use of a second detector placed immediately after the interferometer. This second detector sampled a portion of the amplitude modulated beam exiting the interferometer and would thus collect the interferogram of the light source. If the second detector signal was added to the signal from the optical activity detector, an interferogram with a large zero path difference signal resulted and the optical activity spectrum could be processed by the BioRad electronics and software. Keiderling also

suggested that the second detector should have a different spectral response than the VCD detector. This would enable the optical activity to still be seen against a zero background. Unfortunately, in the ultraviolet case the interferometer instability was just too large for the correction provided by longer wavelength interferograms mixed with the Kerr signals. Correction of the problem at shorter wavelength was not possible as the beamsplitter was opaque for these wavelengths. The second method for overcoming the interferometer instability was to use a 254.6 nm quarter-waveplate between the polarizers. The multi-order waveplate produced a sinusoidal birefringence power spectrum which led to a large zero path difference signal in the interferogram. Although the waveplate produced a large zero path difference signal, the background birefringence overwhelmed any possible formaldehyde Kerr signal as can be shown from the expressions for the PEM signal generated earlier in this chapter.

Because the primary goal was to measure the Kerr effect with a PEM and FT in the infrared, no further attempts were taken to improve the ultraviolet system developed for formaldehyde. It certainly is possible to replace the FT with a UV monochromator and repeat the experiment for formaldehyde, but that measurement would not be directed at addressing the explosives detection problem.

6.7 Fluoroform Near-IR Kerr Effect

After the ultraviolet formaldehyde experiments were abandoned, measurements were made in the near-IR on the overtone bands of fluoroform between 6000 and 9000

cm^{-1} using a classic Kerr measurement setup based on the BioRad FTS60A. The fluoroform measurements were pursued as a proof of the size of the Kerr effect for vibrational bands. Because the ultraviolet Kerr setup could be used to make the near-IR measurements with only minor modifications, the fluoroform measurements were conducted while the infrared Kerr measurement apparatus was assembled.

A classic Kerr setup based on the elements of the formaldehyde measurement apparatus was used for the fluoroform experiments. The Xenon arc lamp source in the formaldehyde experiments was replaced with the BioRad Tungsten halogen source in the FTS60A and the detector was changed to a North Coast high purity germanium detector ($D* = 5 \times 10^{15}$ cm Hz$^{1/2}$ W^{-1}). The polarizers were unchanged, but exhibited a larger crossed transmission of 10^{-3}. In the classic Kerr setup, the quartz PEM was removed from the setup because the quartz PEM was not designed for this spectral region.

The FT was operated with the same settings as in the formaldehyde experiments. However, the UDR was decreased to one matching the collection frequency with the zero crossings of the interferogram. As already mentioned, the interferometer was much more stable for these wavelengths, so collections of over 8192 scans were possible.

Fluoroform had previously been purchased by earlier Steinfeld group members from Matheson, and was used without purification. For the Kerr measurements, the cell was filled with 400 to 700 Torr of fluoroform. At these pressures of fluoroform, there was no need for a buffer gas, and fields of 10 to 12 kV/cm could easily be applied without arcing. The pressure measurements were made with a Matheson 700 Torr pressure gauge.

The most serious problem in the brief fluoroform experiments was the sensitivity of the detector to cosmic rays. Although the detector came with a circuit for minimizing the effects of the cosmic rays, the size of the Kerr signal and the remaining cosmic ray signals were comparable. The cosmic ray spikes in the interferogram produced a sinusoidal variation in the baseline. The sinusoidal variation was removed from baseline with a FFT of the power spectrum with digital extraction of the cosmic ray spikes in the inteferogram. With the removal of the spikes, power spectra with flat lines were recalculated with a second FFT.

Figure 6.9 shows the results of the fluoroform experiment. The Kerr spectrum was collected with 700 Torr of fluoroform and an applied field of 12 kV/cm. The Kerr spectrum was ratioed with the power spectrum of the same sample without the field. The background and Kerr spectra were generated from 4096 scans collected at a scan speed of 2.5 kHz. Two of the bands in the spectrum have been assigned to the CH stretch-bend interacting manifold.[16] The band at 7018 cm^{-1} has been assigned to the transition from the ground state to the N = 5/2 j = 2, where N $= V_{stretch} + \frac{1}{2} V_{bend}$, and j is just an energy ranking, The strong feature at 7322 cm^{-1} has been assigned to the ground state to the N = 5/2, j = 1 transition. The third band at 7100 cm^{-1} is unassigned. The magnitude of the transmission was difficult to determine after the FFT treatment, since the removal of the background noise also eliminated some of the signal. Based on the size of the feature in the noisy baseline, however, the estimated transmission for the strongest feature at 7322 cm^{-1} is 0.005 corresponding to a dispersion angle $(\varepsilon_z' - \varepsilon_x')$ of 0.14 radians.
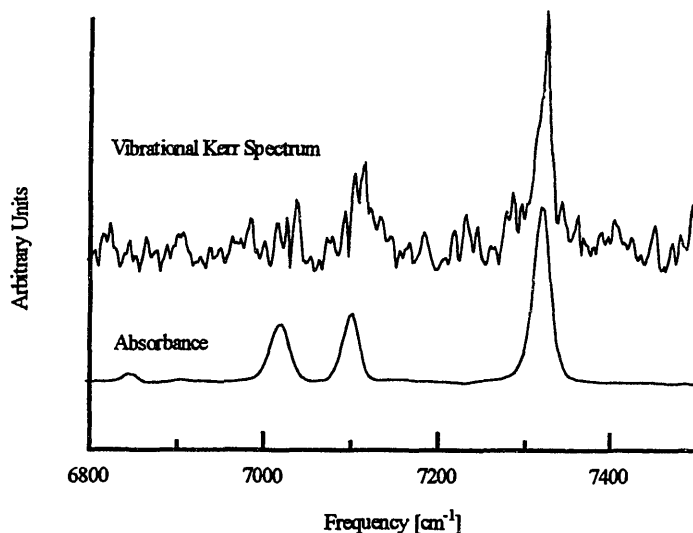
Figure 6.9 Fluoroform Kerr Overtone Spectrum The top trace is the vibrational Kerr spectrum for fluoroform, while the bottom trace is the absorption spectrum.

6.8 FT-PEM Infrared Kerr Measurement

Upon the arrival of the ZnSe PEM and the infrared polarizers, experiments to measure the vibrational Kerr spectrum for nitromethane began. The Hinds ZnSe PEM (Model II ZS37) replaced the Hinds Quartz PEM (Model FS50) in the FTS-PEM Kerr setup described for formaldehyde. The beamsplitter was changed to the BioRad KBr beamsplitter, while the polarizers were switched to the CaF_2 wire grid polarizers (Molectron IGP227). The detector was the Santa Barbara MCT used in the explosive

infrared absorption measurements described in Chapter Two. Unfortunately only preliminary measurements were possible with the infrared FTS-PEM setup as the piezoelectrics used to compress the crystal separated from the crystal on three separate occasions and the decision was made to remove the PEM from the detection system and to attempt classic Kerr apparatus measurements. The next chapter describes the diode laser based classic Kerr apparatus in detail.

References

[1] D.P. Shelton, R.E. Cameron, *Rev. Sci. Instrum.* 59 (1988) 430.

[2] D.P. Shelton, *Rev. Sci. Instrum.* 64 (1993) 917.

[3] E. Charney, R.S. Halford, *J. Chem. Phys.* 29 (1958) 221.

[4] L.A. Nafie, M. Diem *App. Spectrosc.* 33 (1979) 130.

[5] T.A. Keiderling, *Practical Fourier Transform Infrared Spectroscopy* Academic Press Inc. (1990) 203.

[6] P.L. Polavarapu, *Spectrosc.* 9 (1994) 48.

[7] E.D. Lipp, C.G. Zimba, L.A. Nafie, *Chem. Phys. Lett.* 90 (1982) 1.

[8] T.R. Devine, T.A. Keiderling,, *J. Chem. Phys.* 79 (1983) 5796.

[9] T.R. Devine, T.A. Keiderling, *Spectrochim. Acta* 43A (1987) 627.

[10] B. Wang, R.K. Yoo, P.V. Croatto, T.A. Keiderling, *Chem. Phys. Lett.* 180 (1991) 339.

[11] C.N. Tam, T.A. Keiderling, *J. Mol. Spectrosc.* 157 (1993) 157.

[12] D. E. Freeman, W. Klemperer, *J. Chem. Phys.* 40 (1964) 604.

[13] N. J. Bridge, D. A. Haner, D. A. Dows, *J. Chem. Phys.* 48 (1958) 4196.

[14] J. M Brown,. A. D. Buckingham, D. A. Ramsay, *Can. J. Phys.* 49 (1971) 914.

[15] R.K. Yoo, P.V. Croatto, B. Wang, T.A. Keiderling, *Appl. Spectrosc.* 45 (1991) 231.

[16] H.R. Dübal, M. Quack, *J. Chem. Phys.* 81 (1984) 3779.

Chapter Seven

Infrared Kerr Measurements

7.1 Introduction

In this chapter the successful measurement of the rovibrational Kerr spectrum of nitromethane is described. The measurement was made on the asymmetric stretch band of nitromethane at 1584 cm^{-1} shown in the infrared spectrum, Fig. 7.1. The first section of this chapter gives an overview of the classic Kerr detection scheme, followed by a detailed description of the procedures to extract the signal from the detectors in this non-ideal setup. The spectra are evaluated in terms of the qualitative features expected from the theory already outlined in this thesis. Out of the experiments come suggestions for improvement of the measurement of the Kerr effect in nitromethane and other molecules in the infrared.
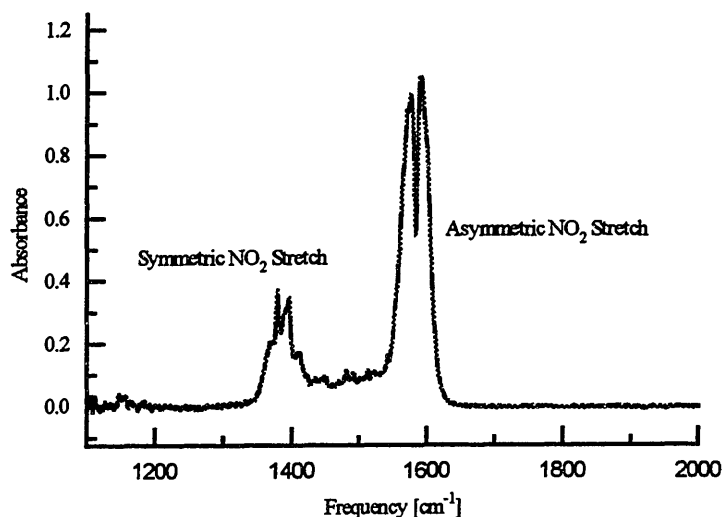
Figure 7.1 Nitromethane Infrared Absorption Spectrum The infrared vapor spectrum of nitromethane was collected with the BioRad FTS60A with 330 mTorr in the Kerr cell.

7.2 Classic Kerr Measurement Setup

In spite of all attempts at improvements, the setup that was most successful in the measurement of the Kerr effect for nitromethane was the classic Kerr setup. The classic Kerr setup used here is shown in Fig. 7.2. The Kerr cell used is described in Chapter Six. The light source for the Kerr setup was a Laser Photonics tunable infrared diode laser (L5621-1560). The multimode power output was 0.5 mW between 1497 cm^{-1} to 1600 cm^{-1}. The laser was cryogenically cooled with liquid nitrogen. The frequency of the laser was controlled with temperature and current. Temperature control was used to select the mode of the laser while current was used to scan within a mode. Within any given mode, the laser was scanned over no more than 3 cm^{-1} with many modes only covering 1 cm^{-1}. The scanning was typically done with current settings between 200 to 300 mA, at scan rates of >0.1 mA/s. At larger currents than the 200 to 300 mA, the laser would operate multimode, and at lower currents the output was too weak. The modes were separated between 2 - 3 cm^{-1}. As the laser aged the mode structure changed, so that some spectral regions were lost. The scanned frequencies were calibrated with NO_2 absorption lines using the HITRAN spectral database.[1] Fits of the frequency versus laser current were done with a third order polynomial with an accuracy of ±0.002 cm^{-1}. In addition, the laser output frequencies and multimode characteristics were independently measured with the BioRad FTS60A. Based on the FTS calibration and characterization, multimode output was not a problem for the small spectral regions measured.

The output of the laser was chopped at 1 kHz with a mechanical chopper. The light from the laser was collimated with a Janos 90° off-axis parabolic gold mirror. The one inch beam divergence was less than 1.5°. For some measurements with the narrow gap Stark plates, the beam was focused onto the detector to limit depolarizing reflections from the Stark plates. Two gold mirror flats were used to direct the light through the Stark plates in the cell. An aperture at the Kerr cell, front window was used to decrease the beam diameter to 1 mm. The diameter was diminished to limit depolarizing reflections from the plates. After the light had traversed the first polarizer and the Kerr cell, 35 % of the light was directed to one of the detectors with a Germanium beam splitter. The remainder of the light was polarization analyzed with a second CaF_2 wire grid polarizer in front of the second detector. The polarizers were Molectron CaF_2 wire grid polarizers (IGP277-25) originally selected for broadband infrared polarizing functionality. The detectors were matched liquid-nitrogen-cooled Electro-optical Systems MCT detectors ($D^* = 1 \times 10^{10}$ cm $Hz^{1/2}$/W at 6 μm) with preampliifiers. The preampilifier was set for gain of 1000. To fill the 1 mm^2 detection element of the detectors, an f/1 lens was used to focus the light onto both detectors. The signals from the two MCT detectors were demodulated with a Stanford Research Systems SR510, and an Ithaco 3990 Dynatrac lock-in amplifiers.
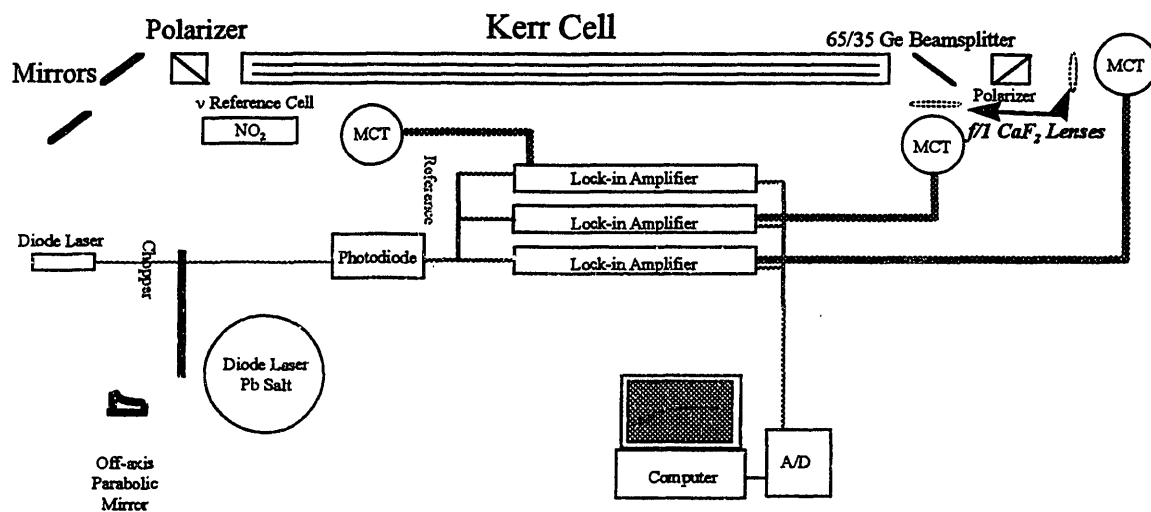
Figure 7.2 Classic Kerr Infrared Laser Diode Setup The light from the infrared diode laser was chopped at 1 kHz with a mechanical chopper. The light after the chopper was collimated with a 90° off-axis parabolic mirror. A portion of the collimated beam was directed into the reference cell for frequency calibration of the source. After traversing the first polarizer and the Kerr cell, 35% of the light was directed onto the first MCT detector with a Ge beam splitter. The remainder of the light was analyzed with a second polarizer. After demodulation with the lock-ins, the three detector outputs were stored and processed with a personal computer.

A portion of the beam was directed into a 9 cm pathlength gas cell containing 200-500 mTorr of NO_2 for frequency calibration of the laser. The laser radiation was detected after the wavelength calibration cell with a Santa Barbara Research Associates MCT detector. The signal from the detectors preamplifier was demodulated with a Princeton Applied Research (PAR) 124A lock-in amplifier with PAR 116 preamplifier. The outputs of all three of the lock-ins were digitized with a Data Translation 8 bit A/D card (DT5712-PGH). The signals were stored and processed with a personal computer.

129

7.3 Experimental Procedures

Nitromethane was purchased from Sigma. The nitromethane was vacuum distilled. Matheson NO_2, without purification, was used for frequency calibration and for Kerr measurement attempts. Both the frequency calibration cell and the Kerr cell were filled from room temperature vapor pressure samples of NO_2 and nitromethane. In the Kerr cell nitromethane was absorbed by the Viton O-rings and the teflon stopcocks over days. For this reason, the cell had to be pumped for at least twelve hours to return to a flat absorption baseline after extended exposures to nitromethane. Eventually the stopcocks and O-rings had to be replaced as they became a near permanent source of nitromethane.

Because the reflections from the Stark plates depolarized the light, optical alignment was crucial to these experiments. As mentioned, the light was directed through the cell with two mirrors for vertical and horizontal adjustment. The wedged CaF_2 windows of the cell deflected the beam and the deflection (0.5 °) had to be accounted for in the alignment of the system. With the first window in place and the Stark plates removed from the cell, two masks simulating the aperture of the Stark plates were placed in the cell. The laser was then aligned through the masks. Once the initial alignment had been made, the plates were returned to the cell. The transmission through the crossed polarizers after this careful alignment was between 1 to 3%, which indicates some birefringence or depolarization from the plates. The crossed transmission of the polarizers alone was less than 0.9%. Because the beam of the diode laser is polarized parallel to the

plane of the laser table top, the signal through the first polarizer was maximized by setting its polarization axis parallel to the table. The polarization axis of the first polarizer was set with a level using the markings indicating the polarization axis on the polarizer mount. The Stark plates were then rotated so that the normal of the Stark plate surface was at 45° with respect to the plane of the laser table. The angle of the plates was set with a 45° cutting angle and level. The minimum of the light signal on the detector was used to cross the polarizers.

The depolarization of the light via the combination of reflections from the plates and birefringence of the windows produced a background signal in the Kerr spectra. The background spectra was a convolution of the infrared transmission spectra and the desired Kerr spectra. To remove the transmission spectra from the Kerr spectra, the second MCT detector was added to the system. A ratio of the two signals on the detectors was taken to remove the background transmission spectra. The two detector signal ratio is preferred over a single sequential scan with and without the field as the spectra are altered by the electric field.

For some of the Kerr spectra, the middle plate of the Kerr cell was removed to increase the aperture size of the plates and to minimize reflections. In these experiments the background transmission was minimized and approached the normal transmission of the crossed polarizers (<0.9%). The wide gap Stark cell was, however, more susceptible to arcing.

For all of Kerr spectra scans, a scan of the diode laser mode is first performed by ramping the current delivered to the diode. With nothing in the Kerr cell and the analyzer

polarizer removed, the ratio of the signals on the two detectors was used to scale the response of the two detectors, and will be referred to as the scaling factor. After the background scan, the analyzer polarizer was returned to the setup, and a second scan was taken. The ratio of the Kerr detector signal to the signal of the second MCT was multiplied by the scaling factor. The scaled second scan was the background transmission of the cell and crossed polarizers. With the background spectrum collected, the cell was filled with the desired pressure of nitromethane or other analyte. A third scan with no field was then taken. This third scan was used to calculate the absorption spectrum. The final scan was taken with the electric field applied. The ratio of the two detector signals was once again taken and multiplied by the scaling factor. The background transmission spectrum was then subtracted from the Kerr spectrum.

7.4 Results

Nitromethane Kerr spectra of the asymmetric stretch band of nitromethane have been recorded in three spectral regions determined by the mode structure of the infrared diode laser. The three regions are shown in Figs. 7.3, 7.4, and 7.5. These figures illustrate the differences between the conventional absorption or transmission spectra and the Kerr spectra. Within these regions several Kerr active features have emerged. First, as expected, the Kerr spectra for nitromethane had fewer strong transitions than the corresponding absorption spectra. Furthermore, the Kerr signal did not necessarily correspond to the absorption strength of the transitions in the absorption spectrum in the

vicinity of the strong Kerr feature. It is postulated that the spectral simplification noted in Figs. 7.3, 7.4, and 7.5 is due to low J sensitivity of the Stark splittings of the $\Delta M's$. Beyond increased total transmission with field, no simple field dependence was found. Figure 7.6 illustrates how the signal can change with electric field. The figure indicates there can be cancellation or enhancement as the field is changed for overlapping lines. The largest transmission at fields of 1 kV/cm and 150 mTorr was 0.5 % for at least one or two lines in the spectral regions probed. At fields larger than 1 kV/cm and at pressures greater than 150 mTorr arcing was a problem. The pressure dependence of the signals was, as shown in Chapter Three for a system with intrinsic birefringence and weak analyte birefringence and dichroism, linearly dependent on pressure. Returning to the results of Chapter Three,

$$I_{det} = \frac{I_0 e^{-(\varepsilon''_z + \varepsilon''_x)}}{2}(T_r + \tfrac{1}{4}(B^2{}_{back} + B_{back}(\varepsilon'_z - \varepsilon'_x) + (\varepsilon'_z - \varepsilon'_x)^2), \qquad (7.3.1)$$

where

$$\varepsilon'_{z,x} = \text{Re}(\Pi_{zz,xx})\frac{lN\omega}{c\varepsilon_0} \qquad (7.3.2)$$

In Eq. (7.3.2), l is the pathlength, N is the concentration of the molecules, ω is the frequency of light, c is the speed of light, and ε_0 is the permittivity of vacuum. Figure 7.7 illustrates the linear dependence of the Kerr signal for a strong line at 1581.35 cm^{-1}.

In order to correlate the observed Kerr spectra to the rotational states of a molecule, several attempts were made at measuring the Kerr spectrum of NO_2 near its asymmetric stretch band in the same spectral regions as nitromethane. In the first couple of scans of the Kerr spectra of NO_2, there were a number of what appeared to be weak Kerr active transitions. However, it was discovered that the Kerr lines were from nitromethane out-gasing from the stopcocks and O-rings. The demonstration of the Kerr detection technique's sensitivity to polar molecules over non-polar or weakly polar molecules was one of the goals of this research. Detection of nitromethane in a cell with over a thousand times greater concentration of the weakly polar NO_2 was an important demonstration of the selectivity of the Kerr effect to polar molecules.
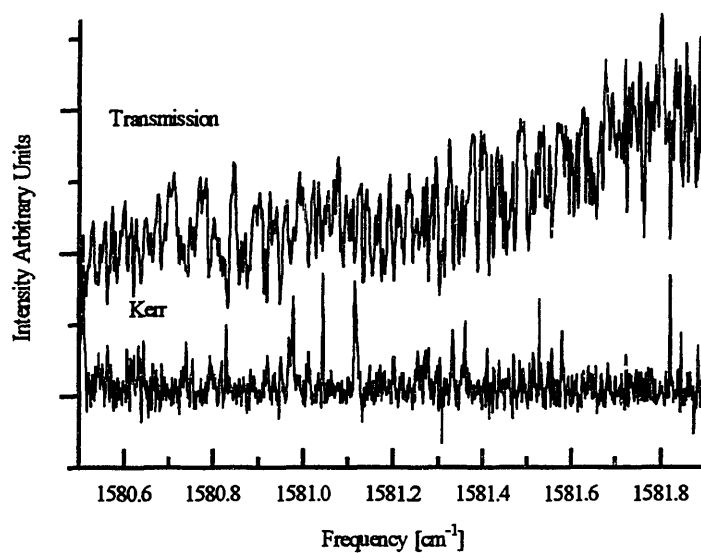
Figure 7.3 Nitromethane Kerr Spectrum 1580.5-1581.9 cm⁻¹. Kerr spectrum of nitromethane recorded with 324 mTorr and a field of 300 V/cm. The strongest Kerr feature has a transmission of 0.5 %.
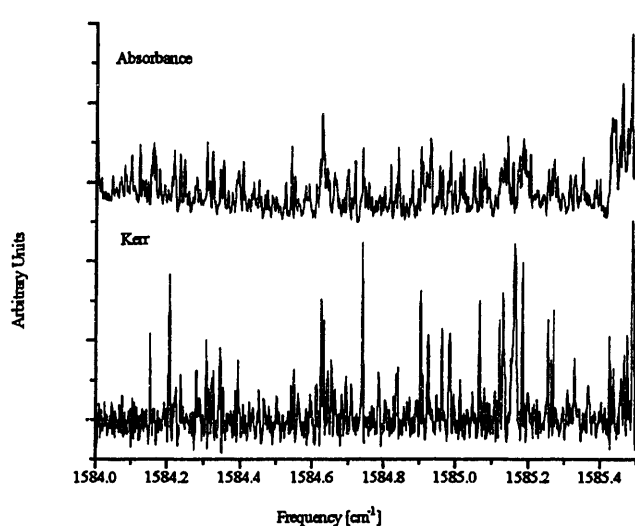
Figure 7.4 Nitromethane Kerr Spectrum 1584.0-1585.5 cm⁻¹. The Kerr spectrum in
this figure was recorded for 143.1 mTorr nitromethane at a field of 400 V/cm. The
maximum transmission in the Kerr spectrum is 0.4 %. A portion of this spectrum is
expanded in Fig. 7.6 to illustrate the field effects.
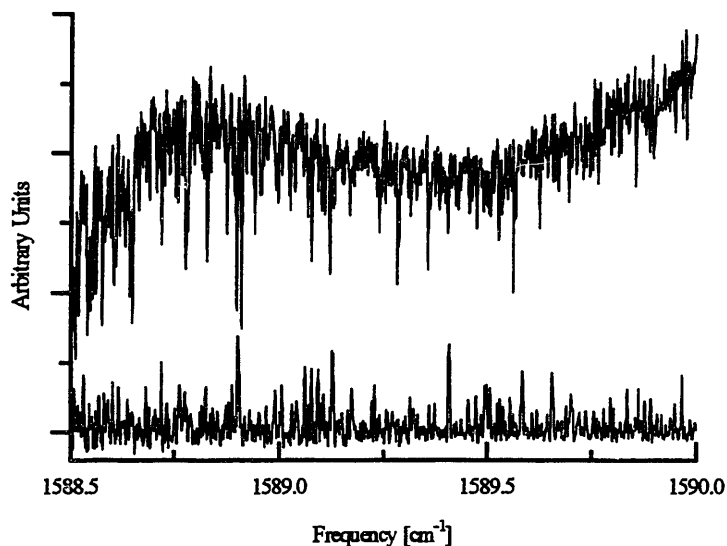
Figure 7.5 Nitromethane Kerr Spectrum 1588.5-1590.0 cm⁻¹. The Kerr spectrum in
this figure was recorded with 143 mTorr of nitromethane in a field 0f 400 V/cm. The
greatest transmission was 0.3 %.
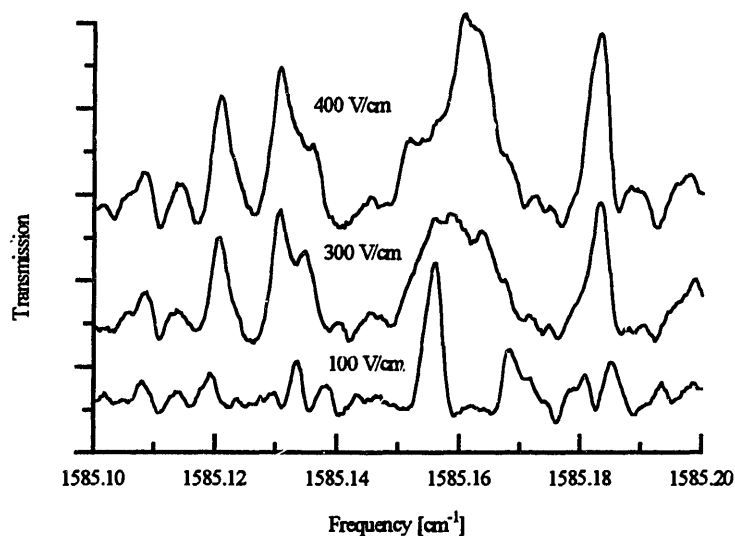
Figure 7.6 Electric Field Dependence As the figure indicates there was no simple relationship between the Kerr signal and the applied field. In fact, the Kerr signal at a given frequency may increase or decrease with increasing field. This behavior of the Kerr spectrum with applied field is indicative of the cancellation and enhancement mechanisms outlined in Chapter Five.
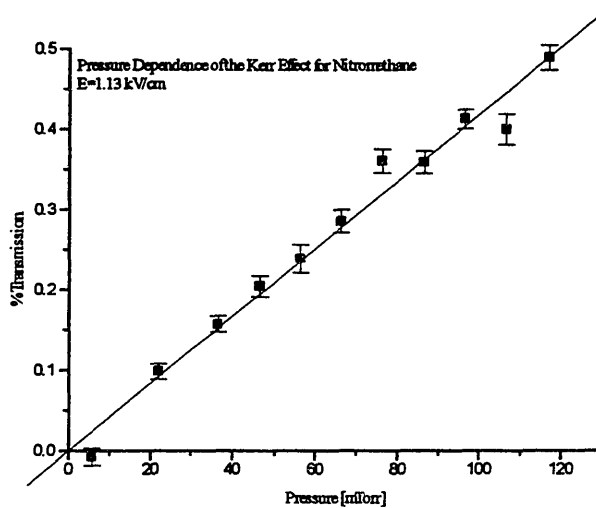
Figure 7.7 Pressure Dependence of the Kerr Effect In the case where the background birefringence is small (transmission < 2%) and where the analyte birefringence and linear dichroism is small, it can be shown that the signal is linear with respect to pressure for low pressures.

136

7.5 Conclusions

Although infrared Kerr spectra in the gas phase were measured for the first time, the experiments need to be improved in several ways before any more meaningful information can be extracted from the Kerr spectrum of nitromethane. Most importantly, the incorporation of a functioning photoelastic modulator would improve the Kerr measurement system tremendously. The capacity of the PEM to improve signal to noise, separate linear dichroism, and birefringence, and utilize only one detector without need for subtraction of undesired transmission would have permitted a more complete evaluation of the source of the features in the Kerr spectrum of nitromethane. The likely improvement in signal to noise with polarization modulation would also permit the study of the effect at lower applied electric fields, where the Stark shifts are less likely to cause transitions to overlap in frequency.

To aid in correlating the rotational states of the molecule to the strong Kerr features, a source must be found with greater coverage of the entire nitromethane asymmetric NO_2 stretch band. In particular, access to the low J transitions in the P, Q, and R branches may have shown strong features related to the low J sensitivity of this technique. The desired, broader spectral coverage would also permit the application of an extraction technique such as extended cross correlation to the assignment of the band. A likely candidate for improved spectral coverage would be a high resolution Fourier Transform spectrometer coupled with the polarization modulation. The correlation

between the observed Kerr spectrum and a calculated Kerr spectrum would also be improved by inclusion of the internal rotor states. For the internal rotor states to be included, the internal rotation parameters of the excited state would need to be determined or measured, perhaps from the Kerr spectrum covering the entire band.

References

[1] L.S. Rothman, A. McCann, L. Abreu, M. Voltaire, S. Harvey, J. Schroeder, HITRAN96, Ontar Corp. (1996).

Chapter Eight

Conclusions

The focus of the Kerr measurements and of the research conducted in conjunction with the Kerr effect has been the sensitive and selective detection of explosives. The research on the Kerr effect has established that the laser diode based classic Kerr measurement setup is not applicable to the task of explosives detection and suggests that the Kerr effect will likely not be a useful means of explosives detection. However, the research has demonstrated a new probe of the rotational structure of infrared vibrational bands of molecules in the gas phase. The qualitative features of the spectra collected here indicate the possibility of making assignments in rovibrational spectra based on the Kerr effect. With the capacity to probe the entire band and the addition of a polarization modulation scheme, the rotational structure of the asymmetric NO_2 stretch band of nitromethane could be assigned for more than just the rotational states without internal rotation. Continuation of the nitromethane research, however, with the current Kerr measurement apparatus is unlikely to lead to any further correlation of the effect to the rotational states of nitromethane or to the measurement of the Kerr spectra of the explosives.

The scope of the explosives detection research has gone far beyond the Kerr effect, however, and included UV-Resonance Raman, surface enhanced resonance Raman, UV-photolysis with NO_2 fragment detection, conventional Raman, and more recently infrared cavity ring-down detection. The UV-resonance and conventional Raman

techniques have been demonstrated as useful tools in probing solutions and solid samples larger than required for most security screening. Conventional Raman has already been used with microscopy to characterize the residues of explosive device construction, and, has, therefore improved understanding of appropriate residue detection.[1]

The results of the surface enhanced Raman (SERS) work suggests that with appropriate engineering of the surface substrates, SERS will be a sensitive detection technique. With detection levels of 1 pg already demonstrated for TNT, the technique must be made more reproducible through the synthesis of colloids with consistent optical properties.[2] In addition to improvement in the optical properties of the substrates, the chemistry of the binding of the explosives to the SERS active substrate must be better understood before substrates with appropriate binding characteristics can be made. If all of these improvements can be made, a SERS based detection system could be deployed for aviation security screening of baggage and cargo. The baggage and cargo could be wiped with a swab. The swab could then be analyzed with a compact diode laser based Raman spectrometer based on an acousto-optic filter or liquid crystal tunable filter. Both filters were considered for explosives detection during my tenure at MIT. The SERS active substrates might be in the swab or attached to the Raman spectrometer. In the second case, the swab would have to be wiped over the SERS active substrate. The collected Raman spectra could then be analyzed for explosive features. The application of extended cross correlation extraction of spectral features related to explosives, explosives binders, and other related compounds could improve the analysis of the spectra likely to contain features from many other compounds.[3]

More recently, work has begun on infrared cavity ring down (CRD) absorption spectroscopy. CRD is likely to become a very useful tool in weak infrared absorption measurements. The possible 3 km pathlength associated with this technique could make the room temperature vapor pressure detection of TNT a reality.[4,5] In addition, unlike other long path techniques CRD can be made with a small sample volume which is crucial in explosives detection where analyte quantities are small. The small volume construction of the CRD systems makes it the ideal infrared absorption system to couple with the Varian membrane separator with cold trap preconcentrator.

In the end, important contributions have been made to the field of explosives detection. Although the focus of this thesis, Kerr spectroscopy, proved to be inadequate to the task of explosives detection, the results indicate the challenges that must be overcome before Kerr spectroscopy can be considered again for vapor phase detection in the infrared.

References

[1] C. Cheng, T.E. Kirkbride, D.N. Batchelder, R.J. Lacey, *J. Forensic Sci.* 40 (1995) 31.

[2] K. Kniepp, Y. Wang, R.R. Dasari, M.S. Feld, B.D. Gilbert, J.A. Janni, J.I. Steinfeld, *Spectrochim. Acta* A51 (1995) 2171.

[3] M.P. Jacobson, S.L. Coy, R.W. Field, *J. Chem. Phys.* 107 (1997) 8349.

[4] J.J. Scherer, D. Voelkel, D.J. Rakestraw, J.B. Paul, C.P. Collier, R.J. Saykally, A. O'Keefe, *Chem. Phys. Lett.* 245 (1995) 273.

[5] Conversations with A.A. Kachanov

Appendix A

BioRad Fourier Transform Spectrometer Terms

Gain Range Ratio-The number of data points from the centerburst of the interferogram for which no gain is applied. Outside this array, a gain is applied to the analog data so that A/D coverter is filled by these weak signals. Since much of the resolution information is in this weak signal the quality of the spectrum collected is enhanced. For Mid-IR spectra the recommended value is 40.

JCAMP-A file format used by the BioRad software when translating data from the BioRad platform to a PC format file. A transmission or absorption spectrum can be translated to the PC format by typing tojcamp [filename] at the % prompt. The output file is stored on the hard drive as a JCAMP format file under the name set in the Newspec parameter with extension .dx. The [filename].dx is an ascii file of rows and columns of data. The header gives all of the collection parameters. The data is formatted so that the first column is an array of approximately every seventh or eighth frequency point divided by the factor Xfactor given in the heading. After each element in this column are each of the absorption or transmission data points between the frequency point in column one and the next frequency point given in column one. These elements are divided by the factor Yfactor also given in the header. This file format is used so that the data can be stored with minimum disk space.

JCAMP File Format

```
#
#Several lines of header giving collection parameters.
#Xfactor=A
#Yfactor=B
#Frequency Start=f;
#Frequency End=f2;
```

Column 1	Column 2	Column 3	Column 4	Column 5	Column 6	Column 7
v1	a1	a2	a3	a4	a5	
v6	a6	a7	a8	a9	a10	a11
v12	a12	a13	a14	a15	a16	a17

In the description of the JCAMP file format the terms v# = frequency data point #/Xfactor, while the terms a# = absorption or transmission point #/Yfactor. The number of columns in each row was not always consistent as illustrated above.

Scanning Frequency (Fourier frequency)-The rate of HeNe zero crossings in the interferometer.

Undersampling Ratio (UDR)-The ratio of the HeNe zero crossing rate to the digital sampling rate of the interferomgram.

Zero Filling Factor (ZFF)-The factor that tells the BioRad software how many zeroes to add to the data set in order to make the interferogram a data set of 2^n elements. The fast Fourier Transform performed by the FT's computer only works for interferograms with 2^n elements.

Appendix B

MATLAB Programs

This program generates the rotational Hamiltonian matrix for the ground and excited vibrational state for the asymmetric NO$_2$ stretch of nitromethane.

function f=nitro2e(J)

For the ground state the following rotational constants were used:

```
C=0.1959942;
B=0.3517224;
A=0.4450372;
DJ=0.2048000*1e-6;
DJK=0.5921000*1e-6;
DK=-0.251500*1e-6;
dj=0.082300*1e-6;
dk=0.5254000*1e-6;
```

%Asymmetric Top Hamiltonian for Nitromethane

The following rotational constants apply to the excited vibrational state.

```
C=0.1960255;
B=0.3516826;
A=0.4449620;
DJ=0.2431000*1e-6;
DJK=0.6822000*1e-6;
DK=-1.570100*1e-6;
dj=0.071700*1e-6;
dk=0.4573000*1e-6;
%[cm-1]
Ke=0:2:J;
Ko=1:2:J;
%Projection of rotational energy on symmetry axis
v1=length(Ke);
v2=length(Ko);

%Diagonal of positive Wang transformation even
for v3=1:v1;
        fep(v3,v3)=1/2*(B+C)*J*(J+1)+[A-1/2*(B+C)]*(Ke(v3))^2-DJ*J^2*(J+1)^2-
DJK*J*(J+1)*(Ke(v3))^2-DK*(Ke(v3))^4;
end;
```

%Off diagonal asymmetric terms positive Wang transformation even
for v4=2:v1-1;
       fep(v4,v4+1)=(1/4*(B-C)-dj*J*(J+1)-dk*Ke(v4+1)^2)*([J*(J+1)-
Ke(v4+1)*(Ke(v4+1)-1)]*[J*(J+1)-(Ke(v4+1)-1)*(Ke(v4+1)-2)])^(1/2);
       fep(v4+1,v4)=fep(v4,v4+1);
end
       fep(1,2)=(2)^(1/2)*(1/4*(B-C)-dj*J*(J+1)-dk*4)*(J*(J+1)*(J*(J+1)-2))^(1/2);
       fep(2,1)=fep(1,2);

%Diagonal asymmetric terms positive Wang transformation odd
       fop(1,1)=1/2*(B+C)*J*(J+1)+[A-1/2*(B+C)]+(1/4*(B-C)-dj*J*(J+1)-
dk)*J*(J+1)-DJ*J^2*(J+1)^2-DJK*J*(J+1)-DK;
for v5=2:v2;
       fop(v5,v5)=1/2*(B+C)*J*(J+1)+[A-1/2*(B+C)]*Ko(v5)^2-DJ*J^2*(J+1)^2-
DJK*J*(J+1)*Ko(v5)^2-DK*Ko(v5)^4;
end;

%Off diagonal asymmetric terms positive Wang transformation odd
for v6=1:v2-1;
       fop(v6,v6+1)=(1/4*(B-C)-dj*J*(J+1)-dk*Ko(v6+1)^2)*([J*(J+1)-
Ko(v6+1)*(Ko(v6+1)-1)]*[J*(J+1)-(Ko(v6+1)-1)*(Ko(v6+1)-2)])^(1/2);
       fop(v6+1,v6)=fop(v6,v6+1);
end

%Diagonal asymmetric terms negative Wang transformation even

for v7=1:v1-1;
       fem(v7,v7)=1/2*(B+C)*J*(J+1)+[A-1/2*(B+C)]*Ke(v7+1)^2-DJ*J^2*(J+1)^2-
DJK*J*(J+1)*Ke(v7+1)^2-DK*Ke(v7+1)^4;
end

%Off Diagonal asymmetric terms negative Wang transformation even
for v8=1:v1-2;
       fem(v8+1,v8)=(1/4*(B-C)-dj*J*(J+1)-dk*Ke(v8+2)^2)*([J*(J+1)-
Ke(v8+2)*(Ke(v8+2)-1)]*[J*(J+1)-(Ke(v8+2)-1)*(Ke(v8+2)-2)])^(1/2);
       fem(v8,v8+1)=fem(v8+1,v8);
end

%Diagonal asymmetric terms negative Wang transformation odd
       fom(1,1)=1/2*(B+C)*J*(J+1)+[A-1/2*(B+C)]-(1/4*(B-C)-dj*J*(J+1)-
dk)*J*(J+1)-DJ*J^2*(J+1)^2-DJK*J*(J+1)-DK;
for v9=2:v2;

```
        fom(v9,v9)=1/2*(B+C)*J*(J+1)+[A-1/2*(B+C)]*Ko(v9)^2-DJ*J^2*(J+1)^2-
DJK*J*(J+1)*Ko(v9)^2-DK*Ko(v9)^4;
end
%Off Diagonal asymmetric terms negative Wang transformation odd

for v10=1:v2-1;
        fom(v10+1,v10)=(1/4*(B-C)-dj*J*(J+1)-dk*Ko(v10+1)^2)*([J*(J+1)-
Ko(v10+1)*(Ko(v10+1)-1)]*[J*(J+1)-(Ko(v10+1)-1)*(Ko(v10+1)-2)])^(1/2);
        fom(v10,v10+1)=fom(v10+1,v10);
end
[esep,evep]=eig(fep);
[esop,evop]=eig(fop);
[esem,evem]=eig(fem);
[esom,evom]=eig(fom);
esep2=esep';
esem2=esem';
esop2=esop';
esom2=esom';

for v11=1:v1;
        f(v11,1)=evep(v11,v11);
        f(v11,2)=J;
        f(v11,6:5+v1)=esep2(v11,1:v1);
        f(v11,6+v1:5+2*v1)=Ke;
end;J

for v13=1:v1-1;
        f(v13+v1,1)=evem(v13,v13);
        f(v13+v1,2)=J;
        f(v13+v1,6:4+v1)=esem2(v13,1:v1-1);
        f(v13+v1,6+v1:4+2*v1)=Ke(2:v1);
end

for v12=1:v2;
        f(v12+2*v1-1,1)=evop(v12,v12);
        f(v12+2*v1-1,2)=J;
        f(v12+2*v1-1,6:5+v2)=esop2(v12,1:v2);
        f(v12+2*v1-1,6+v1:5+v1+v2)=Ko;
        f(v12+2*v1+v2-1,1)=evom(v12,v12);
        f(v12+2*v1+v2-1,2)=J;
        f(v12+2*v1+v2-1,6:5+v2)=esom2(v12,1:v2);
        f(v12+2*v1+v2-1,6+v1:5+v1+v2)=Ko;

end;
```

```
eval(['save esd' int2str(J) ' f -ascii']);
```

The previous program's output files were the rotational eigenstates and eigenvalues. These output files were then analyzed with the next programs which sorted the energies and assigned them the prolate and oblate top limit quantum numbers K_a and K_c.

```
function p=consol(J);

for i=2:J;

        eval(['load esd' int2str(i) ]);
        eval(['temp=esd' int2str(i) ';']);
        [Y,V]=sort(temp(:,1));
        o=length(temp(:,1));
        for l=1:o;
                x(l,:)=temp(V(l),:);
        end;
        eval(['save esds' int2str(i) ' x -ascii']);
i
clear
end;


function f=add(j);

for i=2:j;

        eval(['load esds' int2str(i) ]);
        eval(['e=length(esds' int2str(i) '(:,1));']);
        for i2=1:(e-1)/2;
                eval(['esds' int2str(i) '(2*i2+1,3)=i2;']);
                eval(['esds' int2str(i) '(2*i2,3)=i2;']);
                eval(['esds' int2str(i) '(e+1-2*i2,4)=i2;']);
                eval(['esds' int2str(i) '(e-2*i2,4)=i2;']);
        end;
        eval(['save esds' int2str(i) ' esds' int2str(i) ' -ascii ' ]);
end
```

The next three programs account for Boltzman factor and nuclear spin statistic population factors.

```
function f=add3(j)

for i=1:j;

        eval([' load gsds' int2str(i)]);
        eval([' gsds=gsds' int2str(i) ';']);
        k=0:2:i;
        e=length(k);
        for r=1:length(gsds(:,1));
        if gsds(r,6+e)==1;
        gsds(r,5)=0;
        else
        eval(['gsds' int2str(i) '(:,5)=(2*i+1)*exp(-gsds' int2str(i) '(:,1)/207.223266);'])
        end;
        end;
        eval(['save gsds' int2str(i) ' gsds' int2str(i) ' -ascii'])
end;


function add5(j);
load average

for i=2:j;
        eval(['load gsds' int2str(i)]);
        eval(['gsds' int2str(i) '(:,5)=gsds' int2str(i) '(:,5)/average;']);
        eval(['save gsds' int2str(i) ' gsds' int2str(i) ' -ascii']);
end
```

With the ground state populations calculated, the spectra were generated with the next three programs.

P Branch

```
function f=genp(J);

for i=3:J;
        eval(['load gsds' int2str(i) ]);
        eval(['load esds' int2str(i-1) ]);
        eval(['g=gsds' int2str(i) ';']);
        eval(['e=esds' int2str(i-1) ';']);
        Ke1=0:2:i;
        e1=length(Ke1);
        Ke2=0:2:i-1;
        e2=length(Ke2);
```

```
for i2=1:i-1;
        p(i2,1)=e(2*i2,1)-g(2*i2-1,1)+1583.81163;
        p(i2,2:4)=e(2*i2,2:4);
        p(i2,5:7)=g(2*i2-1,2:4);
        for i3=1:e1;
                K1=g(2*i2-1,5+e1+i3);
                for i4=1:e2;
                K2=e(2*i2,5+e2+i4);
                if K1-K2==-1;
                        int1a(i3,i4)=((i-K1)*(i-K1-1))^(1/2)*g(2*i2-
1,5+i3)*e(2*i2,5+i4);
                elseif K1-K2==1;
                        int1a(i3,i4)=(-1)*((i+K1)*(i+K1-1))^(1/2)*g(2*i2-
1,5+i3)*e(2*i2,5+i4);
                else int1a(i3,i4)=0;
                end;
                end;
        end
        for i5=1:length(int1a(:,1));
        int2a(i5)=sum(int1a(i5,:));
        end
        int3a=sum(int2a);

        p(i2,8)=g(2*i2-1,5)*int3a^2/(16*(i)^2*(2*i+1)*(2*i-1));

        p(i2+i-1,1)=e(2*i2,1)-g(2*i2+3,1)+1583.81163;
        p(i2+i-1,2:4)=e(2*i2,2:4);
        p(i2+i-1,5:7)=g(2*i2+3,2:4);
        for i6=1:e1;
                K3=g(2*i2+3,5+e1+i6);
                for i7=1:e2;
                K4=e(2*i2,5+e2+i7);
                if K3-K4==-1
                        int1b(i6,i7)=((i-K3)*(i-K3-
1))^(1/2)*g(2*i2+3,5+i6)*e(2*i2,5+i7);
                elseif K3-K4==1
                        int1b(i6,i7)=(-1)*((i+K3)*(i+K3-
1))^(1/2)*g(2*i2+3,5+i6)*e(2*i2,5+i7);
                else
                int1b(i6,i7)=0;
                end;
                end;
        end;
        for i8=1:length(int1b(:,1));
```

```
                    int2b(i8)=sum(int1b(i8,:));
                    end;
                    int3b=sum(int2b);


        p(i2+i-1,8)=g(2*i2+3,5)*int3b^2/(16*(i)^2*(2*i+1)*(2*i-1));
        end;
        for i3=1:i;
                p(i3+2*(i-1),1)=e(2*i3-1,1)-g(2*i3,1)+1583.81163;
                p(i3+2*(i-1),2:4)=e(2*i3-1,2:4);
                p(i3+2*(i-1),5:7)=g(2*i3,2:4);
                for i9=1:e1;
                        K5=g(2*i3,5+e1+i9);
                        for i10=1:e2;
                        K6=e(2*i3-1,5+e2+i10);
                        if K5-K6==-1;
                                int1c(i9,i10)=((i-K5)*(i-K5-1))^(1/2)*g(2*i3,5+i9)*e(2*i3-
1,5+i10);
                        elseif K5-K6==1;
                                int1c(i9,i10)=(-1)*((i+K5)*(i+K5-
1))^(1/2)*g(2*i3,5+i9)*e(2*i3-1,5+i10);
                        else int1c(i9,i10)=0;
                        end;
                        end;
                end;
                for i11=1:length(int1c(:,1));
                int2c(i11)=sum(int1c(i11,:));
                end;
                int3c=sum(int2c);

                p(i3+2*(i-1),8)=g(2*i3,5)*int3c^2/(16*(i)^2*(2*i-1)*(2*i+1));
        end;
        eval(['save pd' int2str(i) ' p -ascii']);i
end;

Q Branch

function f=genq(J);

for i=25:J;

        eval(['load gsds' int2str(i) ]);
        eval(['load esds' int2str(i) ]);
        eval(['g=gsds' int2str(i) ';']);
```

```
eval(['e=esds' int2str(i) ';']);
for i2=1:2*i-1;
        q(i2,1)=e(i2+2,1)-g(i2,1)+1583.81163;
        q(i2,2:4)=e(i2+2,2:4);
        q(i2,5:7)=g(i2,2:4);
        Ke=0:2:i;
        e2=length(Ke);
        for i3=1:e2;
                K=g(i2,5+e2+i3);
                        for i4=1:e2;
                        K2=e(i2+2,5+e2+i4);
                        if K-K2==1
                                int1(i3,i4)=((i+K)*(i-
K+1))^(1/2)*g(i2,5+i3)*e(i2+2,5+i4);
                                elseif K-K2==-1
                                int1(i3,i4)=((i-
K)*(i+K+1))^(1/2)*g(i2,5+i3)*e(i2+2,5+i4);
                                else int1(i3,i4)=0;
                                end
                                end
        end
        for ia=1:length(int1(1,:));
        int2(ia)=sum(int1(:,ia));
        end
        int3=sum(int2);
        q(i2,8)=int3^2*g(i2,5)/(16*i^2*(i+1)^2);
        q(i2+2*i-1,1)=e(i2,1)-g(i2+2,1)+1583.81163;
        q(i2+2*i-1,2:4)=e(i2,2:4);
        q(i2+2*i-1,5:7)=g(i2+2,2:4);
        for i5=1:e2;
                K3=g(i2+2,5+e2+i5);
                        for i6=1:e2;
                        K4=e(i2,5+e2+i6);
                        if K3-K4==1
                                int1a(i5,i6)=((i+K3)*(i-
K3+1))^(1/2)*g(i2+2,5+i5)*e(i2,5+i6);
                                elseif K3-K4==-1
                                int1a(i5,i6)=((i-
K3)*(i+K3+1))^(1/2)*g(i2+2,5+i5)*e(i2,5+i6);
                                else int1a(i5,i6)=0;
                                end
                                end
        end
        for i7=1:length(int1a(1,:));
```

151

```
                    int2a(i7)=sum(int1a(:,i7));
                    end
                    int3a=sum(int2a);
                    q(i2+2*i-1,8)=g(i2+2,5)*int3a^2/(16*i^2*(i+1)^2);
          end;
          eval(['save qd' int2str(i) ' q -ascii']);i
end;


R branch

function f=genr(J);

for i=2:J;

          eval(['load gsds' int2str(i) ]);
          eval(['load esds' int2str(i+1) ]);
          eval(['g=gsds' int2str(i) ';']);
          eval(['e=esds' int2str(i+1) ';']);
          Ke=0:2:i;
          Ke2=0:2:i+1;
          e1=length(Ke);
          e2=length(Ke2);
          for i2=1:i;
                    r(i2,1)=e(2*i2+3,1)-g(2*i2,1)+1583.81163;
                    r(i2,2:4)=e(2*i2+3,2:4);
                    r(i2,5:7)=g(2*i2,2:4);
                    for i3=1:e1;
                              K1=g(2*i2,5+e1+i3);
                              for i4=1:e2;
                              K2=e(2*i2+3,5+e2+i4);
                              if K1-K2==-1
                                        int1(i3,i4)=(-
1)*((i+K1+1)*(i+K1+2))^(1/2)*g(2*i2,5+i3)*e(2*i2+3,5+i4);
                                        elseif K1-K2==1
                                        int1(i3,i4)=((i-K1+1)*(i-
K1+2))^(1/2)*g(2*i2,5+i3)*e(2*i2+3,5+i4);
                                        else int1(i3,i4)=0;
                                        end;
                                        end;
                              end;

                    for i5=1:length(int1(:,1));
                    int2(i5)=sum(int1(i5,:));
                    end;
```

```
int3=sum(int2);

r(i2,8)=g(2*i2,5)*int3^2/(16*(i+1)^2*(2*i+1)*(2*i+3));

r(i2+i,1)=e(2*i2-1,1)-g(2*i2,1)+1583.81163;
r(i2+i,2:4)=e(2*i2-1,2:4);
r(i2+i,5:7)=g(2*i2,2:4);
for i6=1:e1;
        K3=g(2*i2,5+e1+i6);
        for i7=1:e2;
        K4=e(2*i2-1,5+e2+i7);
        if K3-K4==-1
                int1a(i6,i7)=(-
1)*((i+K3+1)*(i+K3+2))^(1/2)*g(2*i2,5+i6)*e(2*i2-1,5+i7);
        elseif K3-K4==1
                int1a(i6,i7)=((i-K3+1)*(i-
K3+2))^(1/2)*g(2*i2,5+i6)*e(2*i2-1,5+i7);
        else int1a(i6,i7)=0;
        end;
        end;
end;
for i8=1:length(int1a(:,1));
int2a(i8)=sum(int1a(i8,:));
end;
int3a=sum(int2a);
r(i2+i,8)=g(2*i2,5)*int3a^2/(16*(i+1)^2*(2*i+1)*(2*i+3));

end;
for i3=1:i+1;
        r(i3+2*i,1)=e(2*i3,1)-g(2*i3-1,1)+1583.81163;
        r(i3+2*i,2:4)=e(2*i3,2:4);
        r(i3+2*i,5:7)=g(2*i3-1,2:4);
        for i9=1:e1;
                K5=g(2*i3-1,5+e1+i9);
                for i10=1:e2;
                K6=e(2*i3,5+e2+i10);
                if K5-K6==-1;
                        int1b(i9,i10)=(-
1)*((i+K5+1)*(i+K5+2))^(1/2)*e(2*i3,5+i10)*g(2*i3-1,5+i9);
                elseif K5-K6==1;
                        int1b(i9,i10)=((i-K5+1)*(i-
K5+2))^(1/2)*e(2*i3,5+i10)*g(2*i3-1,5+i9);
                else int1b(i9,i10)=0;
                end
```

```
                    end;
            end;
            for i11=1:length(int1b(:,1));
            int2b(i11)=sum(int1b(i11,:));
            end;
            int3b=sum(int2b);           .
            r(i3+2*i,8)=g(2*i3-1,5)*int3b^2/(16*(i+1)^2*(2*i+1)*(2*i+3));
        end;
        eval(['save rd' int2str(i) ' r -ascii']);i
end;
```

The intensities for each branch were then multiplied by the sum over M of the M dependent direction cosine matrix elements.

THESIS PROCESSING SLIP

FIXED FIELD: ill. _____ name _____

index _____ biblio _____

▶ **COPIES:** (Archives) Aero Dewey Eng Hum

Lindgren Music Rotch (Science)

TITLE VARIES: ▶ ☐ _____

_____

_____

NAME VARIES: ▶ ☑ _Alan_ _____

_____

IMPRINT: (COPYRIGHT) _____

_____

▶ **COLLATION:** _154 p_ _____

_____

▶ **ADD: DEGREE:** _____ ▶ **DEPT.:** _____

SUPERVISORS: _____

___ ___ _____
___ ___ _____
___ ___ _____
___ ___ _____
___ ___ _____
___ ___ _____
___ ___ _____

NOTES:

	cat'r:	date:
		page: ▶ 553

▶ **DEPT:** _Chem_

▶ **YEAR:** _1998_ ▶ **DEGREE:** _Ph.D._

▶ **NAME:** _JANNI, James A._